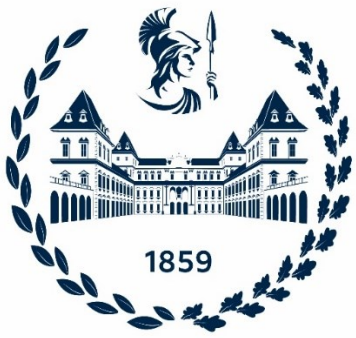

Politecnico di Torino

Master's degree in Civil Engineering

Master's Thesis

Effect of mechanical cracking on the corrosion of steel reinforcement in concrete

Supervisors:

Prof. Ing. Alessandro Pasquale Fantilli
Prof. Ing. Arch. Els Verstynge
Prof. Ing. Ozlem Cizer

Presented by:

Gianluca Chiarella

Academic year 2022-2023

Preface

This thesis is the outcome of a collaboration between two esteemed universities in Europe: the Polytechnic of Turin and the Katholieke Universiteit Leuven (KUL). I am honored to have participated in this collaboration, focusing on a topic as significant as the corrosion of reinforced concrete.

Foremost, my sincere gratitude goes to the supervisors and proponents, Prof. Els Verstrynge and Prof. Özlem Cizer. Their guidance not only enabled me to participate in this experimental work but also demonstrated kindness and genuine interest in the work throughout the entire year. Additionally, I extend my appreciation to Prof. Fantilli, who, despite the distance, consistently showed interest and provided precious advice for this thesis.

Acknowledgments are due to the University and the Department of Civil Engineering at the KUL, where the experimental work in the laboratory was carried out. The laboratory technicians Jan Vander Auwera, Zander Quatacker, Bernd Salaets, provided very important assistance during the experimental phase with their constant availability and efficiency. Gratitude extends to Gerda Hechtermans for her contribution to the crucial chemical experiments required for this thesis.

Special mention goes to Valeria Belloni and Marcello Mutti for their enjoyable and enriching conversations in the laboratory, adding a cheerful note to the experimental program.

The heartiest appreciation for this thesis goes to my daily supervisor, Constantijn Martens. His brilliance and continuous support were of paramount importance throughout the entire thesis project, allowing me to face the challenges that emerged unexpectedly. Thank you immensely, Constantijn!

Finally, I extend profound gratitude to my committed friends who remained close to me despite the physical distance: Giovanni, Francesco, Nicolas and Nazaret. Alejandro's precious company during my time in Belgium. My gratitude extends to my girlfriend, Erica, for consistently keeping me motivated and relaxed even during the most stressful periods. It was no small feat! I am thankful to my elder brother, Mario, who serves as a reliable reference point in all aspects of my life. Lastly, profound thanks to my parents, Alessandro e Maria Assunta, whose daily demonstration of love and sacrifices continually drive me toward my goals and dreams.

Gianluca Chiarella

Table of Contents

Abstract

Due to concrete's limited resistance to tensile forces, reinforced concrete (RC) elements, like beams, can experience mechanical cracking, where tensile stresses are concentrated. When cracks appear in the concrete, they create a direct pathway for aggressive agents, with chlorides being among the most aggressive. Chlorides are commonly found in various environments, especially in marine environments, where they come into contact with RC structures through saltwater exposure. This research aims to analyse how the presence of cracks influences corrosion of steel reinforcement due to chloride-induced corrosion, with a focus on corrosion rate. The outcomes emphasize that the occurrence of transversal cracks significantly influences the corrosion process, as observed through increased corrosion rates correlated with an increase in the width of transversal mechanical cracks.

The natural transport mechanism of chlorides into concrete is a highly debated topic as it is challenging to analyze and predict. This study evaluates the chloride diffusivity using the chloride diffusion coefficient (CDC) and chloride content through experimental work. It investigates how mechanical cracks impact chloride diffusion and establishes correlations between this influence and the corrosion process. These correlations can shed light on significant parameters, such as chloride content and corrosion rate for understanding the corrosion process. Indeed, the findings indicate that the zone with higher chloride content exhibited more pronounced corrosion activity of the steel reinforcement.

Empirical models are typically employed to predict corrosion parameters like chloride content and corrosion rate, necessary for assessing the service life of reinforced concrete structures. This thesis presents a comparison between theoretical predictions and measured results to provide valuable information about the accuracy of these models. The results highlight that incorporating this experimental data into the existing literature-based models for predicting corrosion rate and chloride content is not a straightforward task. This issue requires further investigation and exploration.

To address these research questions, a structured experimental program is adopted. It involves the initial casting of concrete samples, ensuring uniform composition and geometrical properties. Mechanical cracks are induced in most of the samples through three-point bending test, while a few remain uncracked for comparison purposes. Subsequently, the samples are subjected to chloride-induced corrosion using a state-of-the-art setup. Monitoring and assessment of the results employ electrochemical techniques to measure corrosion rates, DEMEC points and other devices to monitor mechanical cracks and potential corrosion crack formations. Additionally, the extraction of rebars from selected specimens and cores is conducted to evaluate the consequences of the corrosion process on the steel reinforcement and the chloride content within the concrete.

List of figures and tables

List of figures

List of tables

List of abbreviations and symbols

Abbreviations

3PBT	3 Point Bending Test
CCI	Chloride Conductivity Index
CDC	Chloride Diffusion Coefficient
CMC	Chloride Migration Coefficient
DC	Direct Current
ECP	Electrochemical Potential
EFM	Electrochemical Frequency Modulation
FA	Ferrochrome Ash
EIS	Electrochemical Impedance Spectroscopy
GGBS	Ground Granulated Blast-furnace Slag
GPT	Galvanostatic Pulse Technique
GR	Guard Ring
HCP	Half-Cell Potential
IC	Impressed Current
LPR	Linear Polarization Resistance
LVDT	Linear Variable Differential Transducer
MDT	Minor-Destructive-Technique
PC	Portland Cement
RC	Reinforced Concrete
RCM	Rapid Chloride Migration test
RE	Reference Electrode
RH	Relative Humidity
SSCE	Silver/silver chloride electrode

Symbols

i_a	Anode electrical density
i_d	Cathode electrical density
V_{corr}	Corrosion penetration
W_{FE}	Atomic weight for iron
i_{corr}	Instantaneous (uniform) corrosion current density
z_{FE}	Valence of iron molecule
F	Faraday constant
G_{FE}	Density of iron
w/c	Water-to-cement ratio
x	Concrete penetration depth
K	Regression constant
ρ_{con}	Electrical concrete resistivity
T_i	Initiation phase

T_p	Propagation phase
$C(x,t)$	Chloride content over time and depth
t	Time
A_{ca}	Cathode area
A_{an}	Anode area
D	Chloride diffusion coefficient
Ψ_p	Mathematical function
erf	Gaussian error function
C_0	Initial chloride content [wt.%/c].
C_s	Chloride concentration at the surface
t_0	Reference time
$D_{RCM}(t_0)$	Apparent migration diffusion coefficient at first exposure time
$D_{app}(t)$	Apparent chloride diffusion coefficient over time
c_{cr}	Critical chloride content
p	Constant
S	Exposure environment and binder type constant
c	Concrete cover
Φ_t,	Residual diameter
Φ_0	Initial diameter
R_p	Polarization resistance
E_{corr}	Corrosion potential
ΔE	Applied voltage
ΔI	Applied current
α	Pitting factor
D_{90}	Chloride diffusion coefficient by (CCI)
L_{crit}	Polarizes critical length
P_x	Averaged penetration
P_{pit}	Maximum pit depth
R_e	Electrical resistance
$W_{Ci,j,0}$	Initial weight of cut-piece *j* for sample *i*
$W_{Ci,j,f}$	Final weight of cut-piece *j* for sample *i*
$L_{Ci,j}$	Length of cut-piece *j* for sample *i*
q_{ref}	Reference cut-piece distributed weight
$\Delta W_{Ci,j}$	Weight variation of cut-piece *j* for sample *i*

Chapter 1: Introduction

This introductory chapter presents the problem statement and the motivation for this research. This work contributes to the PhD research of ir. Constantijn Martens and the lifeMACS project (Life-cycle Methodology for the Assessment of existing Concrete Structures), which is a collaboration between KU Leuven, Ghent University, and “Buildwise” (Scientific and Technical Construction Centre).

1.1 Problem statement

Since the last century, *reinforced concrete* (RC) has been one of the most extensively used building materials. It is a composite material comprising concrete with embedded steel reinforcement, achieved by mixing cement, sand and aggregates with water. The invention of Portland cement greatly contributed to the popularity of concrete, but its inherent limitation in tensile strength led to the introduction of steel bars within the concrete volume to enhance its tensile properties.

The widespread use of RC is attribute to several factors:

- Cost-effectiveness: the ingredients required for making concrete are affordable and readily available.
- Versatility: RC is employed in various types of structures, such as buildings, bridges, dams etc., due to the use of different moulds during the casting process.

Concrete is well-known for its durability; however, in recent years, instances of rapid deterioration have been observed in various RC structures [1]. As a result, the study of concrete structure durability has become a significant research topic today. Interestingly, ancient structures constructed by past civilizations have withstood the test of time, remaining in good conditions even after thousands of years, while modern constructions show significant signs of deterioration within a few decades [2]. For instance, the Colosseum in Rome (Italy), as shown in Figure 1, is an ancient structure dating back to 72 AD, built by the Romans using a different type of concrete made of lime, water, Pozzolana and other building materials like Travertine, brick, Marble, iron/bronze clamps etc..

Several reasons explain the difference between the durability of ancient and modern structures:

- RC is a relatively recent material in comparison to ancient construction methods.

- The environment has become more aggressive due to increased industrial activity.
- Modern design techniques, such as utilizing thinner elements due to advanced Design Techniques (ULS), may contribute to higher susceptibility to deterioration [2].

As a result, the attention to the durability of concrete structures is significantly higher today than in the past.

Figure 1: Colosseum, Rome (Italy)

In addition to these factors, it is worth noting that RC buildings are typically designed with a target of around 50 years. As we progress into the current decade, it aligns with the total designed life of many reinforced concrete buildings that were constructed during the booming construction period of the 1970s, as depicted in Figure 2. Consequently, there is a pressing need for the renovation and rehabilitation of these aging concrete structures.

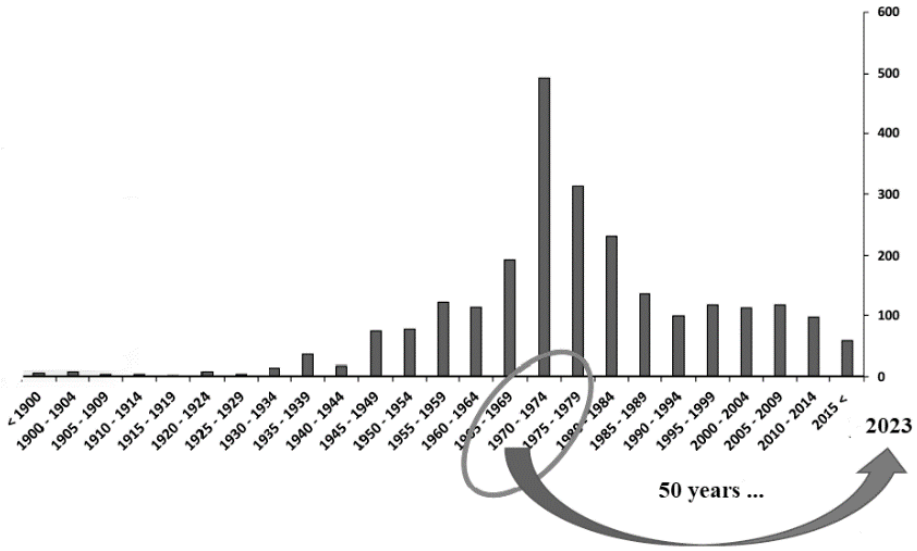

Figure 2: Construction of RC structures over the years; adapted from [3]

As a composite material, the degradation of RC structures can be attributed to both the concrete matrix and the steel reinforcement.

The durability of concrete is primarily influenced by its permeability to water, which is closely related to its porosity. When the porosity is low, aggressive agents dissolved in water find it difficult to penetrate the material. Porosity is closely linked to the water-cement ratio (w/c). A lower w/c ratio results in reduced porosity and higher compressive strength; however, an excessively low w/c ratio can make the concrete less workable, leading to inadequate compaction during construction.

Table 1 provides a list of the causes of concrete deterioration, including chemical, physical and mechanical actions [2].

Table 1: Cause of concrete degradation; adapted from [4]

Chemical	Physical	Mechanical
Sulphates	Frost	Shock
CO_2	Shrinkage	Erosion
Chlorides	Fire	Earthquake
Alkali	Hydration heat	Vibrations

Regarding steel reinforcement, corrosion encompasses all interactions between the environment and the metallic surface. The driving force behind metallic corrosion is the thermodynamically stability of the oxidized form of metallic atoms, making corrosion a natural and spontaneous process, leading the metal's surface to change into more stable state. When steel undergoes corrosion, rust forms and continues until the material bearing section is entirely consumed. *Carbonation-induced corrosion* and *chloride-induced corrosion* are the main causes of reinforcement corrosion [2].

Despite the susceptibility of both materials to degradation, one of the most significant advantages of RC is that concrete provides an alkaline environment within its volume, offering good chemical protection to steel against corrosion and allowing the formation of a passive layer around the rebar. This passive layer helps minimize the steel's exposure to environmental aggressors. However, once the passive layer becomes unstable, corrosion can occur, either due to carbonation, chlorides, or both.

Cracking in concrete creates a direct connection between the embedded steel reinforcement and the atmosphere, facilitating the infiltration of aggressive agents to reach the reinforcement [5]. Mechanical cracks, mostly caused by bending actions, significantly affects beam elements, making them more susceptible to corrosion, with chlorides being one of the most aggressive agents. When chlorides come into contact with the rebar, its passivation is compromised.

Following de-passivation, the rebar starts to corrode, leading to the formation of rust. This corrosion product causes an increase in volume, generating stress within the concrete, which in turn leads to cracking. Furthermore, the mass loss of steel rebars reduces the bearing capacity, ultimately diminishing design capacity of the RC beam, thereby leading to unexpected and premature element collapses [6].

1.2 Research objectives

The primary objective of this thesis is to examine the influence of mechanical cracking on the corrosion of the steel reinforcement in concrete.

To achieve this, reinforced concrete samples with identical geometrical and compositional properties will be cast. Subsequently, three-point bending tests will be conducted to induce cracking in some of the samples, while others will remain intact. The cracked and uncracked samples will then be subjected to chloride-induced corrosion. Electrochemical techniques will be utilized to monitor and analyze the corrosion process in all specimens.

While all cracked specimens will undergo the same casting and corrosion procedures, the cracking process may result in formation of different cracks in terms of width, frequency and orientation. Hence, it will be intriguing to observe how these factors influence the corrosion of the steel reinforcement. Additionally, the uncracked samples will serve as means of comparison to understand the detrimental effects of cracks on steel reinforcement corrosion.

Furthermore, an investigation into chloride into the concrete matrix will be conducted, as it plays a crucial role in developing mathematical models to predict the durability of RC elements subjected to chloride-induced corrosion.

In conclusion, this study aims to compare theoretical corrosion models, used to evaluate corrosion initiation and propagation in advance, and predict chloride penetration and content within the concrete matrix, with the experimental results obtained from the investigation.

1.3 Research methodology

The work plan for this thesis is organized into three main parts: literature review, experimental program, and analysis of results.

Literature review:

The first part of the thesis focuses on conducting a comprehensive literature review. It encompasses general and fundamental aspects of corrosion for steel reinforcement in concrete. Topics covered include corrosion rate measurement, natural and accelerated corrosion processes, and chloride-induced corrosion. The review also searches into the electrochemical corrosion process and the techniques employed to evaluate corrosion rate, such as the Galvanostatic Pulse (GP) method. Additionally, the literature review includes a study on chloride diffusion and corrosion modeling to facilitate comparisons with both theoretical and experimental results. This part is crucial in gaining insights into the results obtained from the experimental program.

Experimental test program:

The second phase of the thesis involves the implementation of the experimental test program. Initially, concrete specimens are prepared, involving molding, demolding, concrete mixture preparation, and casting. Subsequently, the specimens will undergo a three-point bending test, except for some selected specimens. Finally, a natural corrosion setup will be applied to the specimens, monitoring the corrosion rate in the cracked area using the Galvanostatic Pulse (GP) technique. This phase of the study will enable the collection of experimental data necessary for further analysis.

Analysis of the results:

The last part of the thesis consists of analyzing the results obtained from the experimental program. Observations and conclusions will be drawn based on the monitoring phase. Moreover, the influence of mechanical cracks on steel reinforcement corrosion will be assessed by measuring the mass loss of the steel reinforcement. Theoretical results from the literature will be compared with the experimental findings to gain a comprehensive understanding of the corrosion behavior under different conditions.

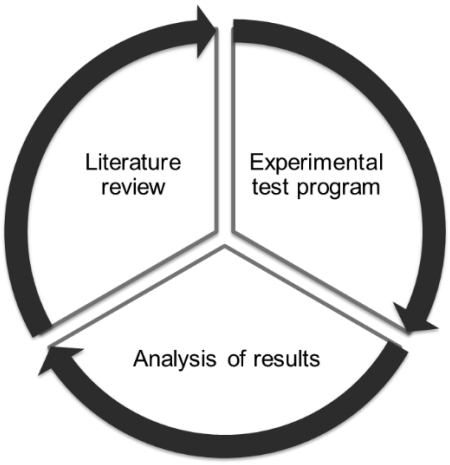

Figure 3: Research methodology overview

In conclusion, this structured work plan will allow for a systematic investigation of the impact of mechanical cracking on the corrosion of steel reinforcement in concrete.

1.4 Thesis outline

This thesis is structure into three distinct parts:

Part 1: Discussion of the state of the art

In this section, theoretical models related to corrosion in RC structures are explored, along with various techniques used for monitoring and assessing corrosion. This part serves as a foundation for understanding the existing research scenery in the field of corrosion in RC.

Part 2: Description of specimens and experimental corrosion setup

This part includes the molding process, material properties, and casting techniques. Additionally, the experimental setup for inducing and monitoring corrosion in the specimens is outlined. This section serves to provide clarity on the experimental procedures and conditions.

Part 3: Analysis and discussion of the results

The core of the thesis lies in this section. It presents a thorough analysis and discussion of the results obtained from the ongoing monitoring and assessment program during the corrosion process until the conclusion of the experimental program. Data on corrosion rates, mechanical crack characteristics, and the impact of corrosion on steel reinforcement are extensively discussed and analyzed.

Finally, a conclusion Chapter:

Following the analysis and discussion of the results, a conclusion chapter will be presented. This chapter summarizes the key observations and outcomes of the research.

The organization of the thesis is as follows:

- *Chapter 1:* Overview and motivation
- *Chapter 2:* Literature study on corrosion in RC and experimental test program
- *Chapter 3:* Specimens casting, cracking and corrosion setup
- *Chapter 4:* Analysis of Theoretical Corrosion Parameters
- *Chapter 5:* Ongoing monitoring results during the corrosion process
- *Chapter 6:* Conclusion, final observations and suggestions for future works
- *Appendices:* Calculations of corrosion parameters and additional graphs.

Chapter 2: Literature study

In this chapter the State of the Art on corrosion in RC is presented. First, the fundamental phenomenon of RC is described, including corrosion potential, corrosion rate, the types of corrosive attacks, the influence of cracks on the corrosion process and the approaches used to evaluate corrosion in laboratory conditions. Then, a study on the chloride diffusion measurement and modelling is presented. Subsequently, the corrosion rate measurement and modelling are described. Later, the effect of corrosion processes on the rebar mass loss is reported. Finally, critical observations are made on the literature study.

2.1 Corrosion in reinforced concrete (RC)

2.1.1 Fundamental principles

When steel is exposed to the environment, it will corrode due to the reaction of iron, the main component of the rebars, with oxygen and water [2]. The driving force that leads metals to corrosion is that the oxidized form of metallic atoms is the thermodynamically more stable one, therefore corrosion is a spontaneous and natural process. The metallic state is temporary. The characters involved in the corrosion process are the metallic surface, the environment, and the metal/environment interface. Corrosion processes can be described as electrochemical processes generated by an oxidation of metallic species, also called anodic reaction, and reduction of either non-metallic or metallic with higher corrosion potential species present in the environment, also called cathodic reaction, see Figure 4.

Anodic reaction: $$2Fe \rightarrow 2Fe^{2+} + 4e^{-} \quad (2.1)$$

Cathodic reaction: $$O_2 + 2H_2O + 4e^{-} \rightarrow 4OH^{-} \quad (2.2)$$

In the anodic reaction, Equation (2.1), the metal is oxidized to *n*+, where *n* stands for the change in valence, the number of electrons formed and ready to serve the cathodic reaction. In the cathodic reaction the four electrons react due to the presence of water and oxygen [4]. The electrons pass through the steel up to the cathodic zone meeting water and oxygen, resulting in formation of hydroxyl ions (OH^-). First, OH^- react with the iron ions forming *ferrous hydroxide* ($Fe(OH)_2$), then reacting with both oxygen and water it becomes *ferric hydroxide* ($4Fe(OH)_3$). Finally, reacting with water, *hydrated ferric oxide* ($Fe_2O_3 \cdot H_2O + 2H_2O$) or *rust* is formed [6]:

$$Fe^{2-} + 2OH^{-} \rightarrow Fe(OH)_2 \quad (2.3)$$

$$4Fe(OH)_2 + 2H_2O + O_2 \rightarrow 4Fe(OH)_3 \quad (2.4)$$

$$2Fe(OH)_3 \rightarrow Fe_2O_3 \cdot H_2O + 2H_2O \quad (2.5)$$

These reactions imply an increase in volume on the reinforcement surface.

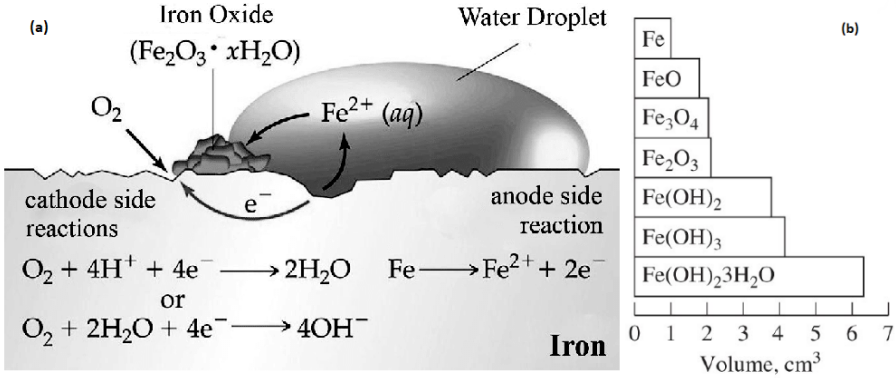

Figure 4: (a) Corrosion of iron in the presence of water and oxygen (adapted from [7]),

(b) Corrosion products volume scale (adopted from [2])

Rust can form uniformly along the exposed metal surface (*uniform corrosion*) causing a large effect on the bond between concrete and reinforcement and a uniform reduction of the steel reinforcement bearing section. Besides, rust can form locally (*pitting corrosion*) generating pits on the metal surface. Pitting corrosion is more affective on the reinforcement bearing capacity than uniform corrosion since it implies a larger local section reduction of the rebar, and it is more complex to detect.

Since concrete is a porous material, it allows the ingress of water and oxygen. It may seem inappropriate to embed within the concrete paste steel rebars, however, the pore solution has a high pH value provided by the *portlandite* (calcium hydroxide) resulting from the cement hydration. From a thermodynamic point of view at high pH values, steel forms a passive film on its surface, making it more resistant to corrosion than in neutral or acid conditions. The Pourbaix diagram illustrates the relationship between the electrochemical potential and pH [8], see Figure 5.

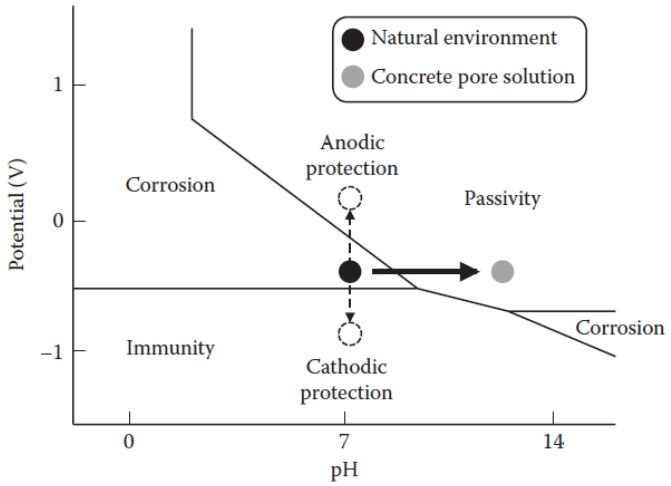

Figure 5: Pourbaix equilibrium diagram; adapted from [2]

Hence, reinforcing steel is passive and not actively corroding due to the high pH in concrete, between 12.5 and 13.5 [9].

Nevertheless, this protective layer cannot always stand. Some mechanisms can cause *depassivation*, leading to active corrosion of the steel reinforcement. The two main mechanisms are: carbonation-induced corrosion and chloride-induced corrosion. Both are discussed below.

2.1.2 Carbonation-induced corrosion

Carbonation of concrete occurs when carbon dioxide (CO_2) from air enters concrete. Carbon dioxide reacts with alkaline elements in order to form carbonates, mainly calcium hydroxide ($Ca(OH)_2$).

$$Ca(OH)_2 + CO_2 \rightarrow CaCO_3 + H_2O \quad (2.6)$$

Due to this reaction, the pH decreases from approximately 13 to less than 8.5 involving in the loss of the passive layer [10].

The carbonation-induced corrosion process has two main steps: reaction between calcium hydroxide (from the cement) and carbon dioxide (from the atmosphere) and the calcium carbonate precipitation. The diffusion of carbonation inside the cement paste over time depends on several factors:

- Temperature, wetting and drying cycles.
- CO_2 concentration
- Permeability or concrete quality can reduce the corrosion rate increasing the concrete resistivity.
- Concrete cover, with a double effect: elongating the electrical current path and delaying the oxygen diffusion.
- Relative humidity. In the range between 50-70% carbonation is more rapid while in dry conditions CO_2 cannot react with Ca $(OH)_2$ due to the absence of moisture and in completely wet conditions CO_2 cannot diffuse through water-filled pores. Thus, the diffusion of carbonation depends on the possibility of CO_2 to penetrate.

Once the CO_2 reaches the steel rebars, the initiation phase ends involving a depassivation of the rebars due to the reaction of oxygen and water with steel. The increment of volume on the metal surface is uniform, it is due to rust formation and an increase in volume from iron-to-iron oxides 2-6 times higher. Since carbonation implies a uniform corrosion process, leading to bond loss between concrete and steel reinforcement followed by full detachment of the concrete cover, with the steel rebars openly in contact with the atmosphere [6].

2.1.3 Chloride-induced corrosion

It can be observed from Equations (2.1) and (2.2) that chlorides do not participate to the corrosion process, but they can influence it if present in sufficiently high concentration.

Pitting corrosion is a common consequence of chloride-induced corrosion due to the specific characteristics of chloride ions and their impact on the protective oxide layer formed on metal surfaces. Pitting corrosion refers to a localized form of corrosion characterized by the development of small pits or cavities on the metal surface. It

arises when the protective oxide layer, typically present on metals like steel is compromised. This compromise can be influenced by several factors, one of which is the presence of chloride ions. Chloride ions play a significant role in the corrosion process of metals. When chloride ions come into contact with a metal surface, they can infiltrate the oxide layer and reach the underlying metal. These ions possess high corrosive properties and act as depolarizers, accelerating the electrochemical reactions responsible for corrosion. In the presence of chloride ions, the integrity of the protective oxide layer can be disrupted at specific points on the metal surface. The corrosive nature of chloride ions causes them to accumulate at these locations, creating an environment conducive to pitting corrosion. Once the protective oxide layer is compromised at these localized points, an electrochemical cell forms between the exposed metal surface and the surrounding metal covered by the intact oxide layer. Pitting corrosion is characterized by its aggressive nature and can progress rapidly, resulting in the formation of deep and narrow pits, as shown in Figure 6.

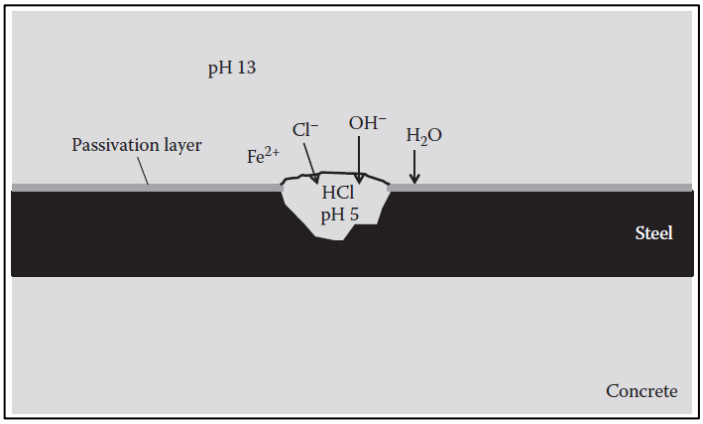

Figure 6: Chloride-induced pitting corrosion in RC; adapted from [2]

Chloride-induced corrosion is more aggressive than carbonation-induced corrosion because of the higher aggressive environment developed into the pit involving in a more acid environment with low ph up to 5. The presence of chlorides into concrete can cause several complications: reduction of (Ca $(OH)_2$) solubility, destruction of the passive film, increase of the moisture content (hygroscopicity of salts (*NaCl*)), and an increase of the concrete electrical conductivity.

The sources of chlorides in RC elements can be:

- De-icing salts, used on roadways in presence of snow and ice. It represents the primary cause of premature failure for structures like bridges.
- Sea water, which has a salt content of *3.5% wt.* Salts dissociate in free chlorides ions and migrate with the water into the pores of the concrete.
- Use of calcium chloride $CaCl_2$ to accelerate the concrete casting.

Chlorides can be present in the concrete solution as *free chlorides* and *bound chlorides.* The firsts are mobile in concrete while the seconds form by reaction with cement hydrates, mainly alluminates. Bounded chlorides may be realised if the pH reduces increasing the free chlorides content. The latters are the responsible for the corrosion initiation phase [11]. However, according to EN 206 26 [12], there is a threshold chloride content that must not exceed *0.4* [% by mass of the cement]. It

depends on several factors such as the concrete cover, moisture content, concrete quality, porosity and temperature.

The chloride threshold content implying the depassivation of the steel reinforcement is still not straightforward. The common idea is that free chlorides accelerate the corrosion process by settling on the metal surface and a breakdown of the protective passive layer occurs locally, implying a pitting corrosion process [13].

The chlorides transport mechanism in the concrete matrix can have two different processes:

- capillary suction for liquids
- diffusion for gases and ions, consisting in electrical or thermal migration and pressure-induced flow.

Close to the surface the capillary suction induces the chloride ions inside the concrete paste, therefore, at the first stages on chloride penetration it represents the dominant transport mechanism, while, in the later stages, chlorides deeply penetrate by diffusion [14]. Furthermore, for the presence of water and chloride in the concrete border, capillary suction is the main mechanism, while deeper in the concrete the diffusion is the main process. In RC elements subjected to corrosion by chloride-containing water, chloride ions move towards the evaporation zone of water, and therefore the highest chloride content is over the water level. The diffusion of chlorides is evaluated with the *diffusion coefficient*. In marine environments, there are three different zones for chloride penetrations: the atmospheric zone, the splash/tidal zone and the submergent zone, see Figure 7. In the splash/tidal zone, the chloride penetration is mainly characterized by capillary suction in dry conditions, and diffusion in wet condition. This zone implies the highest chloride accumulation since cyclic wetting and dry involves water evaporation. Moreover, in the submerged zone the chloride penetration occurs only by diffusion transport since the pores are saturated of water. However, the environmental exposure is not the only important parameter for chloride diffusion, it is also influenced by the type of cement, as for carbonation [15].

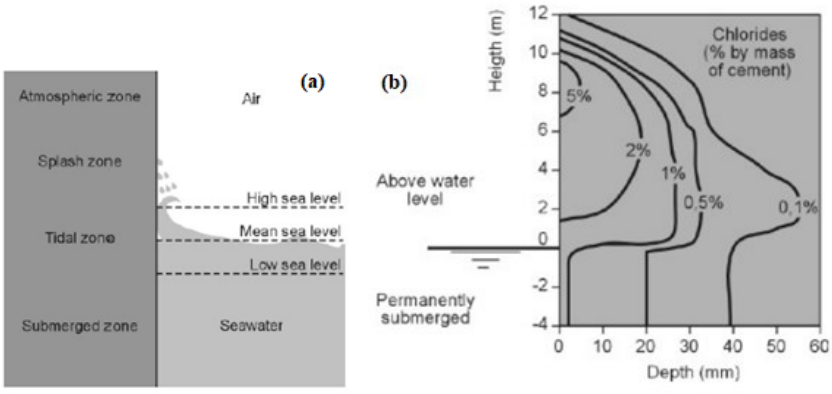

Figure 7: (a) Marine zones of a structure; (b) Chloride penetration in marine zone; adapted from [15]

2.1.4 Corrosion potential

As mentioned in the Section 2.1.1, corrosion of metals is an electrochemical process governed by thermodynamic conditions. The electrochemical device is called *electrochemical cell* and is based on three parts:

- Anode, oxidation part.
- Cathode, reduction part.
- Electrolyte, in contact with both anode and cathode transporting the electrons through the electrical field towards the direction of the anode.

To create the electrochemical cell, a potential difference between anode and cathode must be present. Each electrodes have a certain electrochemical potential (ECP). The anodic zone is characterized by a negative potential while the cathodic one by a positive or less negative potential.

The ECP is a measurement of how much the corrosion process is favoured from a thermodynamic point of view and it is expressed in *Volt* [V]. The ECP can vary in dependence of pH and temperature: the larger is the ECP difference between anode and cathode, the more thermodynamically favoured is the corrosion process, for example, a more negative ECP at the anode and/or a more positive ECP at the cathode implies an increase in corrosion potential. The oxidizing power of a solution can lead to two different kinetic behaviours: active behaviour, with a direct proportionality between corrosion potential and corrosion rate, and passive behaviour, where some metals in high oxidizing environments create a protective layer on the surface which acts as a barrier like in RC [6].

In an electrochemical cell, the two electrodes can be constituted by either different materials or by the same material observing a local different electrochemical potential. In the later situation the corrosion can be of two types: *microcell corrosion* and *macrocell corrosion*.

When corrosion occurs uniformly, as in case of carbonation-induced corrosion or uniformly high chloride content close to the rebar, formation of microcells occurs. The name “microcells” is related to the formation in microscopic size of immediately adjacent anode and cathode and in this case the corroded area is wider. This is due to the fact that the anode and the cathode are adjacent each other, implying a uniform removal of steel [16].

When the corrosion is localized, as in case of chloride-induce corrosion, formation of microcell occurs where the anode is surrounded by a larger cathode, implying a more intensive transfer of electrons from the anode to the cathode. In RC, the anode can form parallel to the cathode when the element is exposed on one side to chlorides and the other to air. Therefore, once the chlorides penetrate and break down the passive layer, the exposed part will act as anode while the other will act as cathode. In this case, the difference in voltage is very high because of the very low (negative) potential of the anode due to the high chloride content, and the very high (positive) potential of the cathode due to the high oxygen content (passivity of the reinforcement).

The last component of the electrochemical cells generated in RC is the concrete which acts as an electrolyte. The migration of ions takes places into the concrete

macrostructure. Therefore, it is important to analyse the ability of concrete to withstand transfer of charge, also called the *resistivity* of the concrete, as discussed below.

2.1.5 Concrete resistivity

Concrete resistivity influences the corrosion process because of the current flow between anode and cathode. Generally, the ability of a material to withstand the transfer of charge is called electrical resistivity ρ [Ωm], it represents the reciprocal of the conductivity σ [S/m]. Concrete resistivity mainly depends on concrete microstructure properties such as the porosity, moisture content and temperature [9], [17].

The conductivity of concrete is in direct relationship with the relative humidity (RH). The higher the RH, the higher the conductivity. It approaches zero at a RH between 40% and 80%, for different types of cements. Moreover, for Portland cement (PC) the less the water cement ratio *w/c* the lower the conductivity, see Figure 8.

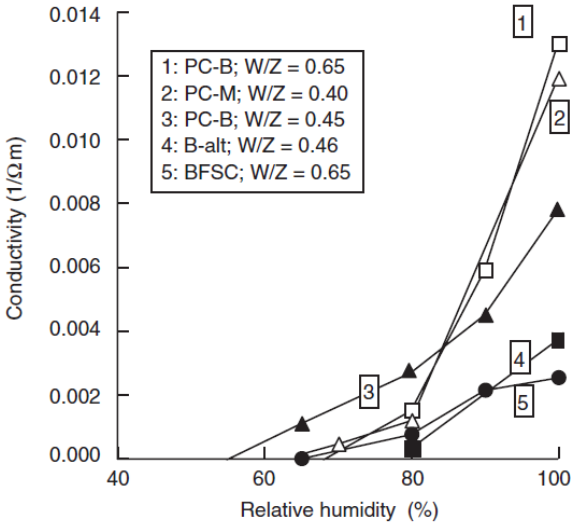

Figure 8: Conductivity vs. RH for different types of concrete; adapted from [6]

Regarding the porosity, a general correlation with concrete resistivity does not exist because of the mobility of the water inside the pores. Nevertheless, the degree of saturation of the pores is the most affecting factor on concrete resistivity.

Generally, concrete resistivity can be easily measured both in laboratory and field conditions. It is a reasonable parameter to predict the corrosion rate through a correlation between concrete resistivity and corrosion rate, which represents a risk for corrosion to occur.

2.1.6 Effect of cracks on the corrosion process

Cracks are a pathway by which chlorides, water and oxygen can easily enter concrete material. Their presence can intensify the corrosion of steel reinforcement and they can form for various reasons. In Figure 9, several causes of cracks are listed, divided into two main types: cracks during concrete setting and hardening and cracks after concrete hardening.

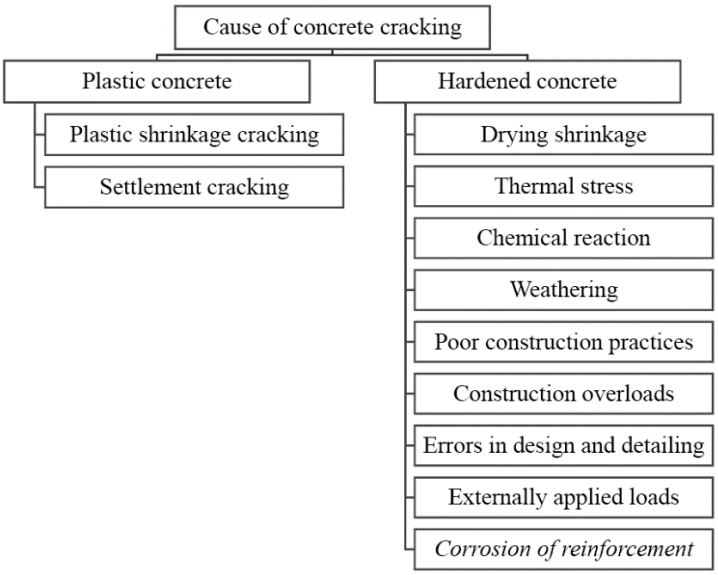

Figure 9: Concrete cracks causes; adopted from [18]

However, understanding the influence of cracking on corrosion of steel reinforcement in concrete is complex as it depends on various factors such as the exposure conditions, mix design, crack orientation, crack frequency, concrete cover and crack width [18].

Regarding the *orientation of the crack*, longitudinal and transversal cracks can form. Longitudinal cracks are mainly due to shrinkage and corrosion of the steel reinforcement itself and represent a highly dangerous corrosion situation as they form a large portion of exposure for the steel reinforcement. This can lead, in the case of chloride-induced corrosion, to a uniform corrosion process. The transversal cracks instead form parallel to the stirrups (when present), as in the case of flexural cracks (subject of this thesis). A comparison between these two types of cracks was made by Poursaee and Hansson [19], where it was observed that with the same crack width of *0.1 mm* for both longitudinal and transversal cracks, the highest corrosion current density was due to longitudinal cracks.

Furthermore, the *frequency of cracks* is also important for corrosion of steel reinforcement, it represents the number of cracks that form along the RC member. Arya and Ofori- Darko [20] observed that the embedded steel reinforcement increased weight loss by an increase in frequency of cracks, an exception was one RC element with the highest crack frequency (20), but narrower crack widths which resulted in an insignificant change in the corrosion process. The cause was related to a possible material self-healing. Nevertheless, Schiessl and Raupach [21] stated that the crack frequency has more importance than crack width on the corrosion rate. In particular, the higher is the crack frequency, the more anode points are formed and the smaller is the cathodic area between the cracks.

Other important research can be related to the *concrete cover*. In an experimental program by Blagojević [22], three different concrete covers of *20*, *30* and *40 mm* were compared, implying three different crack frequencies of 9, 8 and 6 cracks respectively with same maximum crack width of *0.15 mm* for each RC element. Consequently, it was observed that the corrosion of the steel reinforcement decreased by a decreasing in crack frequency or by an increasing in concrete cover. In conclusion,

the crack frequency is a function of the concrete cover and can therefore be considered a secondary parameter.

Finally, one of the most studied parameters for the influence of cracks on steel reinforcement corrosion is the *crack width*. Again, it was observed by Schiessl and Raupach [21] that having two different crack widths of *0.5* and *0.7 mm*, the influence of the crack on the chloride-induced corrosion of the reinforcement was important in the short-term, while the influence was negligible in the long-term. Finally, Abo Alarab et al. [23] investigated the influence of crack width for transverse cracks on chloride-induced corrosion of reinforcement, with crack width sizes of *0.1*, *0.3* and *0.7 mm* and an uncracked RC element. Consequently, the presence of cracks generally showed the most consistent corrosion activity at the location of the cracks. However, the narrowest crack of *0.1 mm* resulted in the slowest corrosion process among the cracked elements. The reason could be related to the accumulation of corrosion products in the cracks, filling the opening and leading to lack of oxygen. This also explains the difference on the short and long-term corrosion process also observed in [21]. In the end, it has been observed that due to the presence of transverse cracks: the corrosion pits tend to form at the crack zone [24] and the ECP can be very different between the crack zone and the ones away from the crack, for example, for a distance of 70 mm the ECP can differ of about 400 mV. Regardless different crack widths, the macrocell pattern does not change significantly, while increasing the crack width, the steel active area increase implying a larger microcell area. Nevertheless, in the localized corrosion processes it has been observed that macrocell corrosion is much more significant than microcell corrosion [25].

In conclusion, there is no certainty about the influence of cracks on reinforcement corrosion as there are several factors. However, this influence becomes much more important with crack widths above *0.20 mm*, while with narrower crack widths, crack filling with corrosion products can slow the corrosion process [18].

2.1.7 Accelerated and natural corrosion

For the experimental evaluations of the corrosion process in RC samples, two different types of corrosion setup can be carried out: *accelerated* and *natural* corrosion. Physiologically, the natural corrosion process is slow; therefore, it is common to accelerate the corrosion process of steel reinforcement to predict the corrosion-induced damage that involves cover cracking, spalling, loss of steel mass and loss of designed steel bearing capacity. The accelerated corrosion is used to replicate real-life corroded reinforcement in a faster way than the natural one. For example, natural corrosion effects which would take 30 years can be obtained in few months by means of accelerated corrosion [24].

Accelerated corrosion can be carried out in laboratory in different ways:

By impressing Current:

It entails the use of either a galvanostat or a potentiostat, as a direct current (DC) power supply, to apply a direct anodic impressed current (IC) to the embedded steel reinforcement. A cathode, such as stainless steel, can be used either externally or internally (embedded in concrete), it acts as a reference electrode (RE). By means of the Faraday's law, the amount of steel reduction can be estimated, however, this can lead to either an overestimation or underestimation depending on the IC applied [26].

Furthermore, IC implies a larger importance of the macrocell corrosion than the microcell because, reaching the threshold chloride content, localised breakdowns of the passive layer are formed in different points on the steel surface involving a larger cathode-to-anode area ratio of the galvanic cell and therefore a higher corrosion rate. Moreover, the IC influences the chemistry of the pore solution in the concrete close to the reinforcement. Lastly, using a galvanostat to accelerate the corrosion process denies the possibility to repassivation, which instead can occur in natural corrosion process.

Cyclic wetting and drying:

It consists of accelerating the corrosion process by spreading chloride-contained water solution in wet and dry cycles, simulating either the tidal/splash marine zone or the cyclic spreading cycles of de-icing salts in non-marine environments. The corrosion setup for this research is based on this technique, spreading salt-water uniformly along the RC specimens, in a controlled temperature room. High temperature can affect the transport mechanics in concrete, damaging the microstructure. This technique increases the chloride penetration rate since it implies more capillary suction, hence shortening the initiation phase. In addition, oxygen depletion is avoided allowing the continuous presence of oxygen at the cathodes, it has been demonstrated the more is the drying phase, the higher is the corrosion rate, for instance, increasing from 2 to 4 day of drying, and keeping 2 days of wetting, the corrosion rate can raise up to 55% [27]. Finally, the oxygen availability allows more stable corrosion products and less voluminous, avoiding the occupation of more space for corrosion agents attacking the steel surface. Nevertheless, the more accelerated is the process, the more it is different from the natural conditions.

For both accelerated corrosion methods, to further accelerate the corrosion process, an *initial chloride content* between 1-5% can be used in the concrete mix. This implies formation of microcells (uniformly distributed corrosion) and if the initial chloride content is too high, the passive protective layer on the steel surface may not form at all [28].

Natural corrosion experiments allow to emulate more accurately the corrosion process for any RC element. Nevertheless, they need more detailed information to be carried out such as specimens and design test set-up, scattering due to the specimen's heterogeneity and most important, long time to obtain valuable results.

2.2 Corrosion rate

The corrosion rate is the speed of deterioration for metallic materials, and it represents the main parameter to describe the corrosion state of metallic materials. The corrosion process can be divided in two main phases*: corrosion initiation* and *corrosion propagation*, see Figure 10.

The corrosion initiation time represents the time needed for the depassivation of steel reinforcement. It starts with entering the concrete matrix of aggressive agents, then these penetrate inside by diffusion causing a gradual depassivation of the steel reinforcement until the reaching of the metal surface implying full depassivation. During the initiation phase the corrosion process does not imply damage [24]. This

phase is characterized by the transport processes, carbonation, chloride diffusion (concrete quality), concrete cover, exposure conditions and sulphate content.

Once the steel reinforcement is depassivated, corrosion begins to propagate. In the propagation phase the rebar starts to corrode and forms rust along its surface. This formation of corrosion product leads to an increase in volume inducing cracking of concrete. Furthermore, the bond between the steel reinforcement and the concrete is lost causing spalling and/or delamination (in case of several parallel reinforcements). Finally, due to excessive mass loss of the steel bearing section, the element collapses.

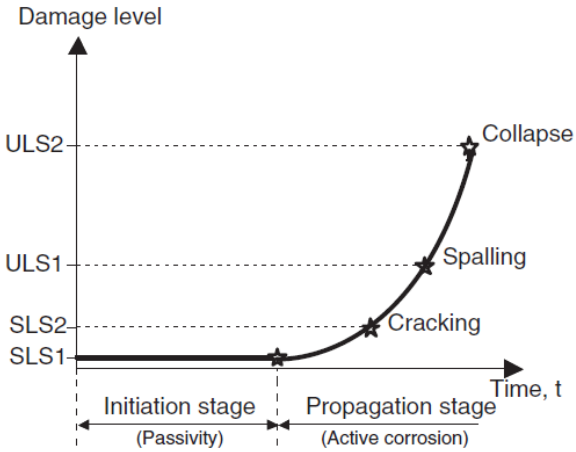

Figure 10: Simplified corrosion model; adopted from [6]

The propagation phase is characterised by the corrosion kinetics, depending mainly on the concrete quality, moisture content, electrical resistivity, temperature, pH of the pore and oxygen availability [29].

In saturated conditions, the oxygen diffusion coefficient is very low since the pores are filled with water (submerged zones). This circumstance is called oxygen depletion. Moreover, the oxygen diffusion resistance of concrete is high enough to consider the corrosion rate negligible, observing a lower corrosion potential due to a lower ECP at the cathode [30]. In the presence of a crack for a submerged RC element, even though oxygen can directly enter through the opening, the opening is filled with water impeding oxygen to enter, therefore slowing down the corrosion process.

To simplify the evaluation of the corrosion rate, some factors can be already referred to others such as the concrete resistivity which depends on temperature, moisture content and concrete quality [31]. It is interesting to notice that the chloride content itself has a lower effect on the corrosion propagation [6].

In case of localised corrosion due to chlorides ingress through a crack, a *galvanic cell* is formed between anode and cathode, where the anode corresponds to the area of the local ingress and the cathode to the non-corroding area.

Equation (2.7) represents an estimation of the corrosion current density (i_{corr}) in a galvanic cell, measured in microamperes per square centimetres [$\mu A/cm^2$]. The equation is given by [6]:

$$i_{corr} = i^{0}{}_{corr}\left(1 + \frac{A_{ca}}{A_{an}}\right) \quad (2.7)$$

Where A_{ca} and A_{an} represent the cathodic and anodic area respectively, in square meters [m^2], as shown in Figure 11 and $i^{0}{}_{corr}$ is the corrosion current density without the galvanic effect, measured in microamperes per square centimetres [$\mu A/cm^2$]. It is interesting to observe that the higher the cathodic area with respect to the anodic one, the more the corrosion current density increases. This demonstrates why the localized corrosion is more aggressive and deleterious than the uniform corrosion.

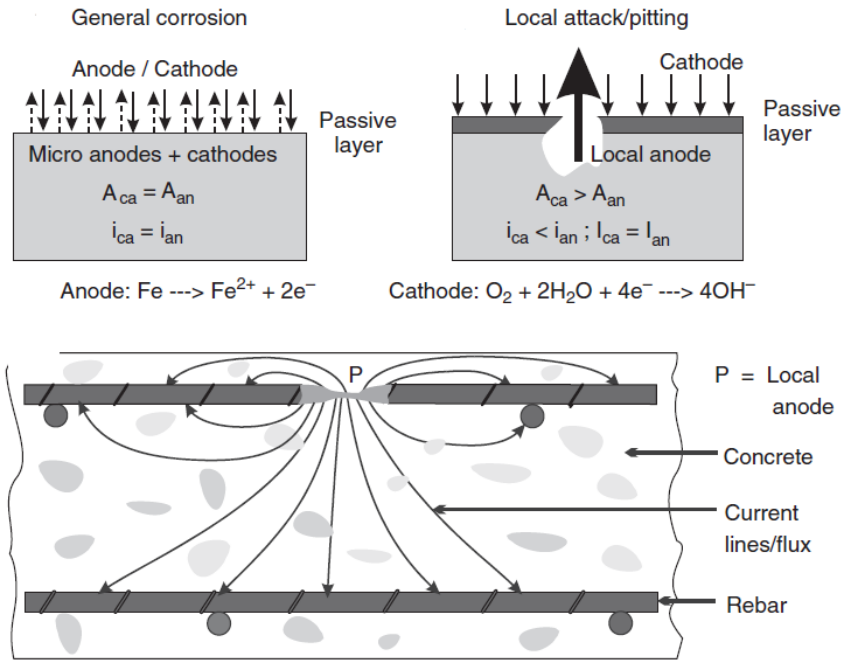

Figure 11: Differences between uniform and pitting corrosion and galvanic cell in concrete; adapted from [29]

Nevertheless, when the cathode-anode area ratio become very high the corrosion current density is lower than it is supposed to be due to the electrochemical resistances of the anodic and cathodic reaction that limit the current flux. However, the evaluation of both anodic and cathodic area is complex. Therefore, to evaluate the corrosion rate, other parameters have been introduced in Section 2.5.

In Equation (2.8), Faraday's law is used to relate i_{corr} to the corrosion penetration (V_{corr}). The equation provides a way to convert the electrochemical measurement of corrosion current density into a more practical measure of corrosion rate expressed in millimetres per year [mm/year]:

$$V = \frac{W_{Fe} \cdot i_{corr}}{z_{Fe} \cdot F \cdot G_{Fe}} \cdot 31.56 \cdot 10^{6} \quad (2.8)$$

where W_{FE} is the atomic weight for iron, measured in grams per mole, 56 [g/mol], z_{FE} is the valence of iron molecule, a dimensionless value [-], F is the Faraday constant, measured in coulombs per mole, 96500 [C/mol], G_{FE} is the density of iron, measured in kilograms per cubic meter, 7874 [kg/m^3].

Corrosion rate measurement using electrochemical techniques, as describes in Section 2.4 of the thesis, is a common practice and at the end of a corrosion process

to monitor and assess concrete structures. The measured corrosion rate values serve as a means to validate the modelled corrosion rates calculated in advance. The modelling of corrosion for a specific reinforce concrete (RC) sample setup is a significant area of research, as it plays a crucial role in predicting the service life of concrete structures.

In recent years, several researchers have been actively developing models to better understand the dependency between the service life of an RC structure and the corrosion process. These models aim to accurately predict the time taken for various corrosion-related damage steps, such as cover cracking and reduction in steel cross-section area. One of the essential input parameters in these corrosion-induced damage models is the corrosion rate. The more precise the prediction of the corrosion rate, the better the estimation of the service life of the structure affected by corrosion [32, 33].

The modelling of corrosion rate typically involves two main phases: the initiation phase (T_i [years]) and propagation phase (T_p [years]).

2.3.1 Initiation phase

The initiation stage for chloride-induced corrosion in uncracked RC specimens can be described by the Fick's second law of diffusion, applying the inverse formula:

$$T_i = \frac{1}{4D} \frac{c^2}{\left(erf^{-1}\left(1-\frac{C_{cr}}{C_{s,0}}\right)\right)^2} \tag{2.9}$$

Again, the diffusion coefficient must take in account the time-dependency of chlorides diffusion and therefore, Equation (2.9) is applied.

2.3.2 Propagation phase

To evaluate the propagation phase of a corrosion, process several empirical models have been developed [34]. They are based on a general relationship between the corrosion rate and measurable parameters such as concrete resistivity, RH, temperature and they can provide simple and practical corrosion rate values based on empirical relationships [6].

For cracked RC elements, the relationship between corrosion rate and transversal (mechanical) crack width has been a matter of debate for a long time. However, a suitable corrosion rate prediction for cracked samples subjected to chloride-induced corrosion was elaborated by Otieno [35].

The experimental program made by Otieno [36] to evaluate the prediction model was based on exposing 105 beam specimens (120 x 130 x 375 mm) to accelerated corrosion (by cyclic wetting and dry, with 3 days of wetting with water containing 5% salt and 4 days of drying) and other 105 specimens to natural corrosion in a tidal zone of marine environment with about 2% of salt. A rebar of diameter *10 mm* was embedded in the specimens. The concrete mix and properties of the specimens are reported on Table 2.

Table 2: Concrete mix proportions and selected properties, adopted from [36]

Material (kg/m³)	Binder composition	100 % PC	50/50 PC/GGBS		70/30 PC/FA	
	w/b ratio	0.40	0.40	0.55	0.40	0.55
	Mix label	PC-40	SL-40	SL-55	FA-40	FA-55
Portland cement, PC (CEM I 42.5 N)		500	231	168	324	236
Ground granulated blastfurnace slag (GGBS)		-	231	168	-	-
Fly ash (FA)		-	-	-	139	101
Fine aggregate: Klipheuwel sand (2 mm max.)		529	749	855	749	855
Coarse aggregate: Granite (13 mm max.)		960	1040	1040	1040	1040
Water		200	185	185	185	185
Superplasticizer[a] (SP)		2.1[b] (0.4)[c]	1.8 (0.4)	0.3 (0.1)	0.4 (0.1)	-
Slump (mm)		120	105	150	85	200
28-day compressive strength (MPa)		58.2 (3.0)[d]	48.1 (2.0)	35.3 (0.9)	50.7 (0.9)	28.6 (1.9)

[a] Chemical base: Naphthalene Formaldehyde Sulphonate.
[b] Percentage of SP by mass of total binder.
[c] Amount of SP in litres/m³.
[d] Standard deviation.

It is crucial to consider both the cement type and the exposure condition since the chloride diffusion coefficient obtained in the described experiment may vary from that of the experimental work presented in this thesis.

Equation (2.10) presents a relationship between the corrosion rate (i_{corr}) and several experimental variables such as concrete cover, crack width and concrete quality. The equation is expressed as:

$$i_{corr} = k_2 \left(\frac{c}{w_{cr}}\right)^{-A_2} \tag{2.10}$$

where w_{cr} is the crack width, measured in millimetres [mm], c is the concrete cover, measured in millimetres [mm], A_2 [-] and k_2 [μA/cm^2] are constants dependent on the cement type, w/c and exposure environment. The parameters K_2 and A_2 are distinguished for field specimens and laboratory specimens, where the field specimens are subjected to natural corrosion and the laboratory specimens are subjected to accelerated corrosion. The expressions in relation with the chloride diffusion coefficient $D_{app}(t)$ are the following:

$$k_2 = \begin{cases} 5.18\, e^{0.01\left(D_{app}(t)\cdot 10^{10}\right)},\ R^2 = 0.9, & lab\ (l) \\ 0.64\, e^{0.06\left(D_{app}(t)\cdot 10^{10}\right)},\ R^2 = 0.9, & field\ (f) \end{cases} \tag{2.11}$$

$$A_2 = \begin{cases} 0.96\left(D_{app}(t)\cdot 10^{10}\right)^{-0.35},\ R^2 = 0.7, & lab\ (l) \\ 0.21\, e^{0.02\left(D_{app}(t)\cdot 10^{10}\right)},\ R^2 = 0.8, & field\ (f) \end{cases} \tag{2.12}$$

By substituting Equations (2.11) and (2.12) into (2.10), the following corrosion current density expressions are obtained [35]:

$$\begin{aligned} i_{corr,l} &= \left[5.18\, e^{0.01\left(D_{app}(t)\cdot 10^{10}\right)}\right]\left(\frac{c}{w_{cr}}\right)^{-0.96\left(D_{app}(t)\cdot 10^{10}\right)^{-0.35}} \\ i_{corr,f} &= \left[0.64\, e^{0.06\left(D_{app}(t)\cdot 10^{10}\right)}\right]\left(\frac{c}{w_{cr}}\right)^{-0.21\, e^{0.02\left(D_{app}(t)\cdot 10^{10}\right)}} \end{aligned} \tag{2.13}$$

For the calculation of the predicting model, Otieno considered the diffusion coefficient D_{90} obtained by the 90-day chloride conductivity index test (CCI). However, on the conclusion it was stated that diffusion coefficient obtained by rapid chloride migration (RCM) test can be used too.

In the end, a comparison was made by using a regression model (relationship between dependent and independent variable with R_2 the coefficient of determination) noticing that the results were in good agreement, see Figure 12:

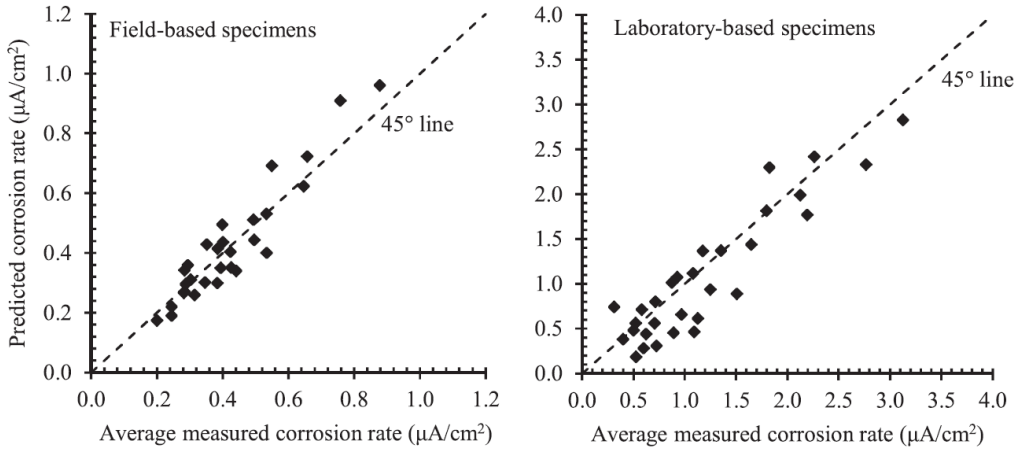

Figure 12: Predicted vs. measured corrosion rate; adopted from [35]

The corrosion initiation phase modelling was not included in this experiment, since for cracked specimens the initiation phase is drastically shortened or eliminated.

2.3 Chloride diffusion and chloride content

The diffusion and content of chloride within concrete samples play a crucial role in the corrosion process of steel reinforcement. This *natural* process is accelerated in the case of accelerated corrosion, where electrical current speeds up the chloride ingress, resulting in a non-natural dynamic of chloride transport.

In the short term, the main transport mechanism for chloride ingress is capillary suction which operates at the surface of the concrete samples. However, beyond a certain depth, diffusion becomes the dominant transport mechanics. The transport of chlorides through diffusion is described by the *chloride diffusion coefficient*, often referred to as the *apparent chloride diffusion coefficient* to account for its time-dependent behaviour.

The diffusivity of chlorides into concrete is critical factor in determining the chloride content within the sample. The chloride content is an important parameter for assessing the risk of the chloride-induced corrosion; higher chloride content increases the risk of corrosion.

The models used to simulate chloride penetration in concrete structures are divided into two main categories: empirical models and quasi-scientific models. Empirical models are derived from modified versions of Fick's 2nd law of diffusion, while quasi-scientific models take a more scientific approach to model specific aspects of the chloride penetration process. After careful consideration, the study prioritizes the evaluation of empirical models over quasi-scientific ones, citing their better fulfilment of the required criteria for assessing the chloride penetration process [37].

Equation (2.14) represents a general analytical model for the chloride concentration (C) at a specific depth (x) and age (t) in a cementitious material. The chloride concentration is denoted as a percentage by mass of the cement. The equation is given by:

$$C(x,t) = C_0 + \mathrm{S}\left\{(t - t_0)\, D_{app}\right\}^p \Psi_p\left(\frac{x}{2\sqrt{D_{app}\,(t-t_0)}}\right) \tag{2.14}$$

Where $C(x,t)$ [% by mass of the cement] is the chloride concentration at depth (x) and age (t), C_0 [% by mass of the cement] is the initial chloride level, S [-] is a constant that depends on the exposure environment and binder type, D_{app} for the apparent diffusion coefficient, measured in square meters per time unit [m^2/s] and p [-] is a constant greater than 0. The mathematical function $\Psi_p(z)$ is analogous to the conventional error function complement and are used in the equations when p assumes the value of zero [37], obtaining the following expression, referred to as the ERFC-Solution with Time-Dependent D_{app}, is obtained [38]:

$$C(x,t) = C_0 + (C_\mathrm{S} - C_0)\left[1 - \mathrm{erf}\left(\frac{x}{2\sqrt{D_{app}\,(t-t_0)}}\right)\right] \tag{2.15}$$

Equation (2.15) is preferred to Equation (2.14) as in practical scenarios, the surface chloride level tends to increase with time, but it often stabilizes and reaches a relatively constant value within a relatively short period compared to the intended service life of the structure. Due to this behavior, it is common practice to adopt an approach where C_s (the time-dependent build-up of the surface chloride level) is assumed to be time-independent, denoted by setting the constant p to zero (i.e., $p = 0$) [37].

Equation (2.16) represents an analytical expression introduced by Colleopardi [39] for predicting the chloride concentration (C) in a cementitious material based on Fick's second law of diffusion. The equation describes the diffusion of chloride ions through the material over time. The equation is given by:

$$\frac{\partial \mathrm{C}}{\partial \mathrm{t}} = D\,\frac{\partial^2 C}{\partial \mathrm{x}^2} \tag{2.16}$$

In this equation, D is the chloride diffusion coefficient, typically expressed in square meters per second [m/s^2]. The chloride diffusion coefficient used in Equation (2.16) is not time dependent. Several researchers discovered that the constant value is unrealistic for short service lives of structures. It was observed that the chloride diffusion coefficient is more dependent on the long-term exposure corrosion than short-term.

Equation (2.17) introduces the concept of the apparent chloride diffusion coefficient (D_{app}) as a time-dependent relationship to replace the constant value of the diffusion coefficient. The equation is given by [40]:

$$D_{app}(t) = \mathrm{k}_e \cdot D_{RCM}(t_0)\left(\frac{t_0}{t}\right)^a \tag{2.17}$$

Where $D_{app}(t)$ [m/s^2] represents the apparent chloride diffusion coefficient at time t, $D_{RCM}(t_0)$ [m/s^2] is the chloride migration coefficient at the first exposure time t_0 [years], a [-] is the aging exponent which indicates the drop over time of the apparent

diffusion coefficient and k_e [-] refers to the effect of temperature on the ingress of chloride in concrete. This drop over time is still not clearly understood among researchers, but some causes could be the cement hydration, that implies a denser concrete microstructure, and the environment because of concrete drying through ion-exchange with moisture and water [41].

Another important parameter which characterises the diffusion coefficient is the moisture content of concrete: the higher the moisture content, the larger the chloride diffusion coefficient. This is because in conditions of high RH (pores full of water) the ions can move easily, while the molecules of oxygen and carbon dioxide cannot penetrate inside the material [29], see Figure 13:

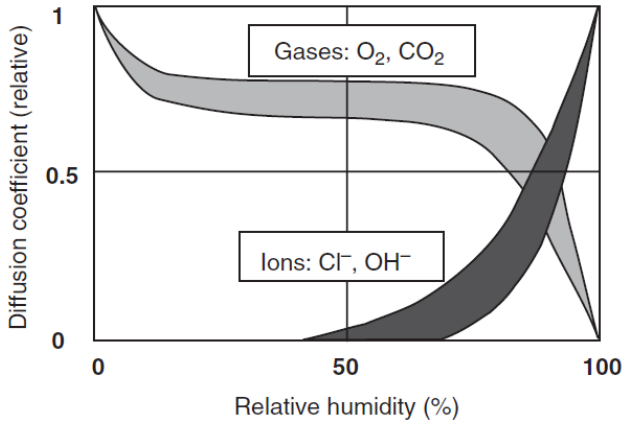

Figure 13: Influence of RH on gas and ions diffusion coefficient; adopted from [6]

The modelled chloride migration coefficient is commonly validated by comparing it with measured values. Two types of tests can be conducted to evaluate the apparent diffusion coefficient: laboratory diffusion test and rapid chloride migration (RCM) test. In this experimental work, the RCM test, specifically the Nordtest method, is performed to evaluate the chloride diffusion coefficient. The Nordtest method involves calculating the chloride migration coefficient by measuring the depth of chloride penetration. By establishing an analytical relationship between the chloride migration coefficient and the chloride diffusion coefficient, the RCM test provides a means to estimate the diffusion coefficient based on measured chloride penetration depths. This test is used to measure the chloride migration coefficient (CMC), which differs from the chloride diffusion coefficient (CDC). For CMC, the migration is related to the movement of ions subjected to an electrical excitation, while for CDC diffusion is related to the movement of ions and molecules due to a different concentration zone, from the lowest to the highest. However, the coefficients are related analytically and hence from measuring the CMC it is possible to evaluate the CDC. The Nordtest method is based on the application of an external electric potential acting along a direction of the specimen. After a certain test duration, it is possible to measure the *chloride penetration depth* as the presence of chloride on the surface of the sample becomes visible by spaying a $AgNO_3$ solution. From the penetration depth, the CMC can be calculated [42].

Additionally, Equation (2.15) introduces the function $C_s(t)$ [% by mass of cement], which defines the time-dependent build-up of the surface chloride level and is described by Equation (2.18):

$$C_s = C_0 + \mathrm{S}\left\{(t - t_0)\, D_{app}\right\}^p \tag{2.18}$$

The time-dependent characteristic of surface chloride concentration in concrete is characterized by a rapid increase during the initial years of exposure, followed by a gradual slowdown after a certain period, eventually stabilizing. Notably, the available literature data on surface chloride concentration behavior over time are still limited or scarce, despite various mathematical models being proposed to represent its trend, such as power or exponential growth functions [43].

The proximity to the coast significantly impacts the transportation of marine aerosols, which play a crucial role in the surface chloride concentration of concrete. As ascending air currents carry marine aerosols, they can reach high altitudes and be transported several kilometres inland by prevailing winds. The concentration of marine aerosols decreases with the distance from the coast, thus influencing both chloride salt deposition and the surface chloride concentration of concrete in coastal areas [44].

The ambient water, including rainfall and humidity, also affects the chloride salt deposition on the concrete surface. Rainfall can wash away chloride ions from the concrete, reducing the surface chloride concentration. Conversely, high humidity levels promote chloride absorption into the concrete, potentially increasing the surface chloride concentration [43].

Within concrete, two types of chloride ions exist: binding chloride ions, adsorbed by the solid matrix of concrete, and free chloride ions in the concrete pore solution. The total chloride concentration is a combination of both types, and the distribution is described using Fick's second law of diffusion. The empirical approach used in the study is built upon a robust dataset, consisting of a significant number of observations from chloride penetration profiles obtained by inspecting a diverse range of existing structures with varying ages, spanning around 60 years. Because the empirical model is derived from actual data, it is not subject to formal validation [37].

Lastly, the surface chloride concentration of concrete is affected by environmental conditions such as exposure time, distance from the coast, and wind speed, as well as material factors like the water-to-binder ratio. In the past, researchers have proposed various mathematical expressions to evaluate C_s, taking into account several parameters that influence it. One such expression, describing the parameter in marine environments for tidal zones which takes into account w/c ratio and time of exposure is provided by Liu [45]:

$$C_s = \left(0.257\frac{\mathrm{w}}{\mathrm{c}} + 0.254\right)\mathrm{t}^{0.383} \tag{2.19}$$

Where C_s is expressed as mass percentage of chloride to concrete and t indicates the exposure time [years].

After evaluating the chloride diffusion coefficient and estimating the chloride content using models, the next step is to subject the samples to a certain period of corrosion. Following this corrosion period, the chloride content within the samples can be measured. The measurement of chloride content is performed by extracting cores from the samples that have undergone the corrosion process for a specific duration.

These cores are then subjected to chemical treatment, known as *titration*, to determine the chloride content.

It is crucial to carefully select the location for analysing the chloride content within the samples. In Section 5.4 of the thesis, as part of the monitoring and assessing process, the specific zones where the cores are extracted for chloride content analysis are identified. These zones correspond to areas where the corrosion state is more advanced. By combining this chloride content data with the electrochemical parameter data, a comprehensive understanding of the corrosion state induced by chlorides can be obtained.

2.4 Electrochemical techniques

Commonly used techniques for monitoring the corrosion process involve measuring the instantaneous corrosion current density i_{corr} [μA/cm^2] using the concept of *Polarization Resistance* (R_p) [Ωcm^2]. These measurements provide valuable information for evaluating parameters such as the corrosion potential E_{corr} and the concrete resistance R_e, which are crucial for assessing the corrosion current density.

The corrosion potential (E_{corr}) represents the electrochemical potential at which the corrosion process occurs. It is typically measured in millivolts (mV) and provides insights into the thermodynamic driving force behind corrosion.

Equation (2.20) represents a relationship between the concrete electrical resistance (R_e), measured in ohms [Ω] and the concrete resistivity (ρ), measured in ohmmeters [Ωm]. The equation is given by:

$$R_e = \frac{\rho l}{A} \tag{2.20}$$

In this equation, l is the length of the concrete sample, measured in meters [m] and A is the cross-sectional area, measured in square meters [m^2].

By measuring the corrosion potential and concrete resistance, along with other factors like temperature and electrolyte properties, it is possible to calculate the corrosion current density. This value represents the rate at which corrosion is occurring and is usually reported in units of microamps per square centimetres (μA/cm^2).

These corrosion monitoring techniques based on i_{corr}, R_p, E_{corr}, and R_e are widely utilized due to their simplicity, reliability, and ability to provide real-time information about the corrosion process. They play a crucial role in assessing the corrosion state of concrete structures, optimizing maintenance strategies, and ensuring the long-term structural integrity and durability of infrastructure.

Electrochemical techniques are minor-destructive techniques (MDT) since the steel reinforcement which acts as working electrode (WE) must be connected by a cable to the receiver. Hence, a small part of concrete has to be removed.

R_p is evaluated through transient or coulostatic methods, as in the case of the Galvanostatic Pulse (GP) technique. However, an appropriate equivalent electrical model is assumed in these methods.

The measurements are carried out by means of a well-defined potential electrode, also called refence electrode (RE) and a working electrode (WE) which is the reinforcing steel. By connecting both electrodes with a voltmeter, the potential difference can be measured. This type of configuration is also known as two-electrode setup. However, to gain information on the corrosion kinetics of the system, the WE needs to be polarized from its open circuit potential. To polarize the WE, an electrical current can be applied using a 3rd electrode, also called counter electrode (CE), forming a three-electrode setup. The CE must be a non-corroding metal, such as stainless steel and acts as a source of electrons for the WE during the reaction [46].

As explained in Section 2.1.4, from a kinetic point of view, cathodic and anodic reactions occur at the same time, resulting in a decrease of anodic potential and increase of cathodic potential. When both reactions occur at the same rate, the corresponding corrosion potential is defined E_{corr}, and since both half-cell reactions cannot be directly measured, the sum of them is considered with the net current equal to 0 [A] at the corrosion potential, see Figure 14.

Equation (2.21) defines the R_p as a measure of the resistance against the potential shift of a corroding system away from its E_{corr}. The polarization resistance represents the ratio between the applied potential difference (ΔE) and the applied current (ΔI) during polarization of the metal from its corrosion potential, typically within a range of about 20-50 millivolts (mV). The equation is given by:

$$R_p = \frac{\Delta E}{\Delta I} \tag{2.21}$$

Where ΔE represents the change in potential, measured in volts [V] and ΔI represents the change in current, measured in amperes [A].

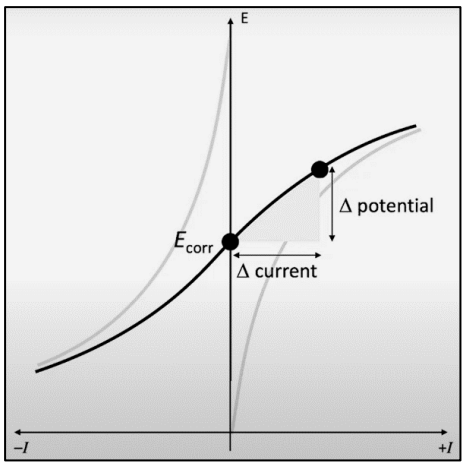

Figure 14: Polarization resistance in a half-cell reaction; adapted from [46]

The instantaneous current density is defined by the Stern-Geary relationship [46]:

$$i_{corr} = \frac{B}{R_p} \tag{2.22}$$

Where B [-] represents a combination of the anodic and cathodic Tafel slopes, and its value is tabulated. To distinguish the localized corrosion from the uniform corrosion, I_{corr} is written with the capital I while the small i refers to uniform corrosion. Finally, the corrosion rate is expressed as V_{corr} [mm/year] and it represents the volumetric loss of

reinforcement steel by unit of area and time. It is obtained from the corrosion current density by means of the Faraday's law introduced by Equation (2.8) and expressed in the following simplified way [47]:

$$V_{corr} = 0.0116\, I_{corr} \tag{2.23}$$

However, the resulting values of the corrosion current density can be erroneous due to the polarised area or current confinement. This happens when the CE is much smaller than the WE, implying the applied current to be non-uniformly distributed along the steel reinforcement with the vanishment of the electric signal due to large enough distances. Therefore, to fix this problem there is a critical length L_{crit} which must be confined in a delimited area [47], see Figure 15.

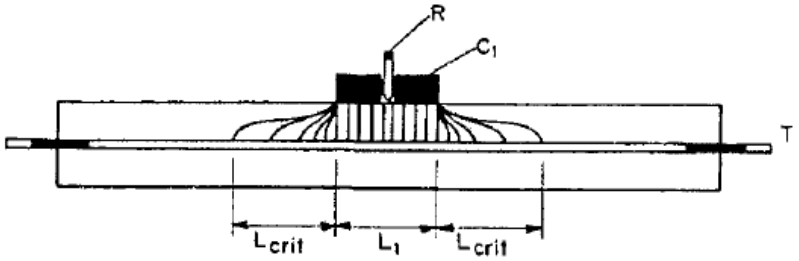

Figure 15: Critical length of polarized rebar by externally applied current, adopted from [47]

One way to confine the polarized area is the application of a guard ring (GR). This is an external circular counter electrode which enable to confine the current applied by the central CE within the GR.

2.4.1 Half-cell potential (HCP)

The half-cell is generated from two electrodes, the steel reinforcement WE and the RE, and the potential difference represent the half-cell potential or corrosion potential E_{corr}. To measure the HCP, different components are used: RE on the concrete surface, WE, voltmeter, and connection of RE and WE for the electrolytic continuity, see Figure 16.

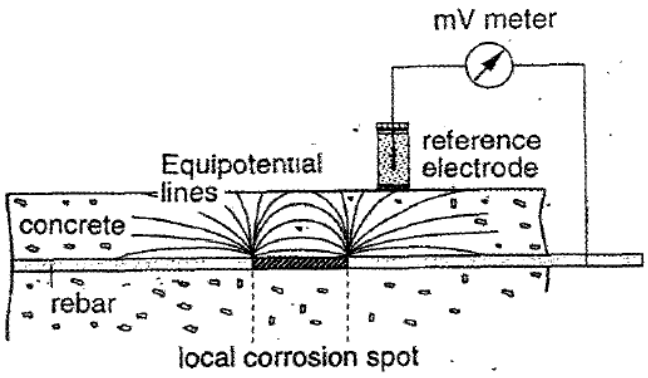

Figure 16: Components of Half-cell measurement, adopted from [48]

A silver chloride reference electrode (Ag/AgCl) is usually adopted. The RE is connected to the negative terminal, while the WE to the positive one of the voltmeter. This results in negative values of the measured HCP and it can only be positive only in case of passive state of the steel reinforcement and dry conditions of concrete [48].

On the contact surface between the RE and the concrete surface there is ions transport. In order to have a good electrical conduction, a wet sponge is placed in between the two parts which reduces the resistance between the RE and the concrete.

The measurements strictly depend on:

- Concrete cover depth: the larger the cover depth, the smaller becomes the potential difference between anode and cathode.
- Concrete resistivity: the higher the concrete resistivity, the harder the recognition of small corroding locations.
- Moisture content: the more wet the concrete surface, the more negative the HCP values. However, the measurements must be carried out with a wet concrete surface (not saturated).

HCP measurements do not provide quantitative information about the corrosion rate since it is not possible to evaluate the corrosion current density I_{corr}. However, this technique allows to visualize the risk for corrosion (in time and space).

Due to the numerous factors that can affect the measurements, the HCP measurement is usually supplemented by other techniques which results can be compared [48].

2.4.2 Galvanostatic Pulse (GP)

The Galvanostatic Pulse Technique is a non-destructive technique. The main purpose of the GP technique is the evaluation of the corrosion rate by measuring the polarization resistance R_p. It is configured as a three-electrode technique with both CE and RE applied on the concrete surface and the reinforcement acting as WE. It also contains other components such as guard ring and the sponge (as discussed earlier), see Figure 17.

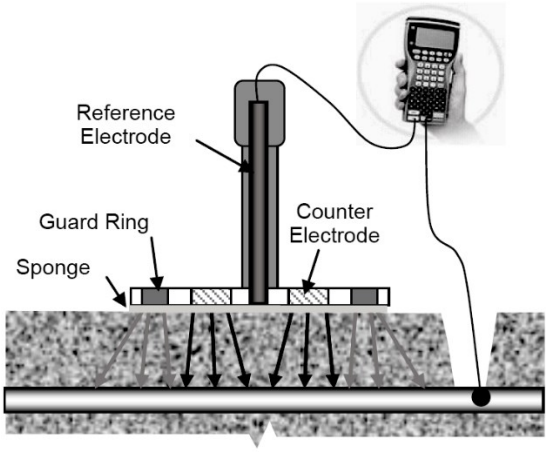

Figure 17: Components of GalvaPulse, adapted from [49]

The GP technique is based on the impression of a short-time anodic current (current pulse), between *5* to 400 *μA* by the CE and pulse duration between *5* to 10 *s*. The applied current changes the potential of the steel reinforcement implying polarization

in the anodic direction. The corrosion state of the reinforcement affects the extension of the polarization and the potential difference, since the difference between the polarized potential and the free corrosion potential is more negative for a rebar undergoing corrosion [50]. The GP is used to measure the HCP, the electrical resistance (R_e) and the corrosion rate (V_{corr}) of the reinforcement, by measuring the corrosion current density (I_{corr}). By means of the Randle's circuit, the GP technique measures the polarization resistance, after which the corrosion current density is calculated by the Stern-Geary equation, finally by applying the Faraday's law, the corrosion rate is evaluated according to [49]:

$$V_{corr} = 0.0116 \frac{I_{corr}}{A} \tag{2.24}$$

Where A is the confined area of the rebar below the CE, measured in square centimetres [cm^2].

The validation of electrochemical technique is usually made by comparison with *gravimetric weight loss measurement* which is a destructive technique.

2.5 Gravimetric weight loss of rebars

The corrosion of steel reinforcement in concrete results in the loss of metal. To assess this weight loss, the gravimetric wight loss measurement technique is employed. This destructive technique involves extracting the rebars from concrete samples, chemically cleaning them to remove remaining concrete fragments attached and corrosion products, and finally weighing the corroded rebars. The test guidelines for this technique are specified in ASTM G1-03 [51].

The primary purpose of this technique is to validate the weight mass loss predicted by electrochemical techniques through real mass loss measurements. By comparing the weight of the rebar before and after the corrosion process, the actual mass loss can be determined. This measured mass loss should align with the prediction made by electrochemical techniques based on Faraday's law. During laboratory research on the corrosion process of reinforced concrete samples, corrosion parameters such as E_{corr}, I_{corr} and V_{corr} are measured at different times. To predict the mass loss, a representative value (I_{corr}^{REP}, V_{corr}^{REP}) is calculated as an average of each measurement conducted during the corrosion process using the following formula:

$$I_{corr}^{REP} = \frac{\sum_{i=0}^{n} I_{corr,i}}{n} \tag{2.25}$$

Once the representative value is obtained, the penetration attack P_x [mm] can be calculated. P_x represents the reduction in radius of the reinforcement after a certain duration of the corrosion process. It is also used to evaluate the structural performance and damage level of corroded reinforced concrete elements [47]. P_x is determined using Faraday's law considering the propagation time (t_p) [years]:

$$P_x = 0.0116 \cdot I_{corr}^{REP} \cdot t_p = V_{corr}^{REP} \cdot t_p \tag{2.26}$$

However, P_x represents the corrosion propagation depth in the case of purely uniform corrosion, measured in millimetres [mm]. To account for localized corrosion, the *pitting factor* α [-] is considered. It distinguishes the type of corrosion attack and is expressed as:

$$\alpha = \frac{\Phi_0 - \Phi}{P_x} \tag{2.27}$$

For conservative predictions in concrete structures, α is considered equal to 10 for localized corrosion, while for uniform corrosion it is considered equal to 2, recognizing that corrosion processes are never perfectly uniform [47].

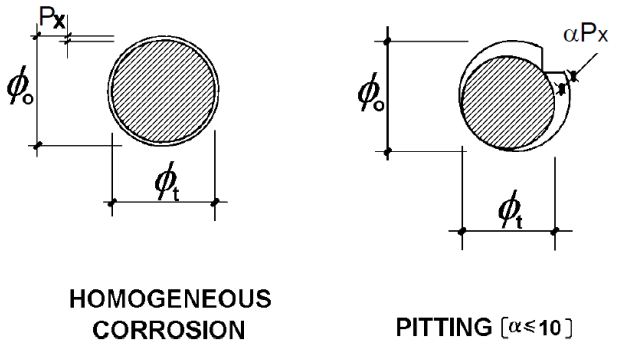

Figure 18: Pitting factor, adopted from [52]

Multiplying the pitting factor by the corrosion penetration, the maximum pit depth P_{pit} [mm] can be predicted:

$$P_{pit} = P_x \cdot \alpha \tag{2.28}$$

However, comparing the decrease in rebar diameter can be inaccurate. Therefore, a more precise approach is to compare the weights.

Equation (2.29) provides a method to calculate the final weight of the rebar (W_f) after corrosion has occurred, based on the corrosion propagation depth (P_x or P_{pit}) [47]. The equation is given by:

$$W_f = \pi L \rho \left(r_i^2 - P_x^2 - 2 r_i P_x\right) \tag{2.29}$$

Where L [mm] is the length of the cut piece of rebar, ρ is the density of the rebar, measure in grams per cubic millimetres [g/mm^3], and depending on the type of corrosion attack, either P_x or P_{pit} should be used.

Furthermore, the corrosion rate can be estimated by the inverse of the measured mass loss using the following equation [53]:

$$V_{corr} = \frac{k \cdot \Delta w}{A \cdot t \cdot \rho} \tag{2.30}$$

In this equation, Δw is the weight loss, measured in grams [g], k [-] is a constant, A is the exposed surface area, measured in square millimetres [mm^2] and t is the exposure time, typically measured in years [year].

2.6 Conclusion

The literature review serves as a valuable resource for understanding the key concepts and factors that influence the corrosion of steel reinforcement in concrete. It provides a foundation for designing and conducting the experimental program effectively.

The initial part of the literature review focused on the fundamental principles of the corrosion process. It emphasizes the importance of parameters such as chloride content, RH, temperature and concrete mix in describing and analysing chloride-induced corrosion. While chlorides are the primary cause of corrosion initiation, other factors can also affect the corrosion rate. The literature highlights the significance of environmental exposure, particularly in marine environments where the splash and tidal zones pose the highest risk to concrete structures. This insight informs the corrosion setup for the experimental program.

The second part of the literature review searches into the technical aspects of modelling and assessing the corrosion of steel reinforcement in concrete. It underscores the difficulty and importance of accurately predicting the corrosion rate, which is a critical parameter for describing the corrosion state. For corrosion assessment, both HCP and GP techniques are adopted. The use of these techniques in conjunction allows for comparisons and evaluations of the corrosion potential during the monitoring process, contributing to conclusions about their accuracy and reliability.

A central concept of this thesis is the significant influence of cracks on the corrosion process. The presence of cracks enables direct contact between chlorides and the rebars, accelerating the corrosion process. However, the impact of cracks is dependent on factors such as crack width, frequency and orientation.

Chapter 3: Samples and test setup

This chapter outlines the different phases in the experimental program, starting from Section 3.1 with the specimen design, to Section 3.3 with the natural corrosion setup. Finally, an overview on the experimental tests is given in Section 3.4.

3.1 Description of the test samples

For the experimental investigation, a total of nine reinforced concrete samples were made, all possessing identical geometric and material characteristics.

The samples were divided into three different groups based on their preparation methods:

- Four specimens were subjected to simple cracking using the Three-Point Bending Test (3PBT). This method induced cracks of a certain width in these four samples.
- Another three were notched, intending to create a crack in the middle of the sample during the 3PBT.
- Finally, the remaining two specimens were intentionally left uncracked to serve as a reference group.

The primary objective of the experiment was to create cracks that closely resembled real-world conditions in order to simulate the phenomenon of corrosion in RC elements within structures that possess mechanical cracks. By replicating realistic crack patterns and characteristics, the study aimed to investigate how corrosion behaves in RC elements that are subjected to similar cracking scenarios as those encountered in practical applications.

The labels adopted to identify the samples are the following:

Table 3: Sample labels

Number	Specimens	Label
2	Uncracked	UC1
		UC2
4	Cracked	C1
		C2
		C3
		C4
3	Cracked and notched	CN1
		CN2
		CN3

As indicated, the numbering from 1 to 4 is assigned to the cracked specimens and the numbering from 1 to 3 is assigned to the cracked and notched specimens. These numbers represent the ascending order of the main crack width measured immediately after the 3PBT using a Linear Variable Differential Transducer (LVDT), as stated in Section 3.3.

3.1.1 Samples design

In the design of the samples, the following specifications were considered:

- *Reinforcement*: Each specimen was reinforced with a steel rebar positioned centrally along the width and eccentrically along the height. The rebar had a diameter of 14 mm and was made of BE500 grade steel with a nominal yield strength of 550 MPa.
- *Concrete cover*: A concrete cover of 25 mm was provided around the steel rebar, as shown in Figure 19.
- *Galvanostatic Pulse technique*: To monitor the corrosion rate on the sample's surface (as described in Chapter 5), the rebar needed to be connected to the open circuit using a clamp. For this purpose, the rebar extended from the concrete surface.
- *Heat shrink epoxy layer*: Prior to the casting phase, an heat shrink epoxy layer was applied to the surface of the rebar. This step aimed to prevent crevice corrosion in the cavities between the rebar and the concrete surface during the corrosion process.
- *Anti-corrosive paint*: An anti-corrosive paint was used beneath the epoxy layer and on the embedded end of the rebar. This was done to avoid the formation of weak zones and to focus attention on the corrosion occurring in the central zone, especially for the cracked specimens. The anti-Corrosion paint was applied on the embedded end within the concrete matrix, considering the exposure of the rebar on two concrete sides.

The geometrical properties of the specimens are as follows, as shown in Figure 19:

- volume: *800x110x80 mm^3*
- rebar diameter: *14 mm*
- concrete cover: *25 mm*
- anti-corrosive paint length: *10 mm* on the left-hand side, *70 mm* on the right end side
- heat shrink epoxy layer length: *60 mm.*

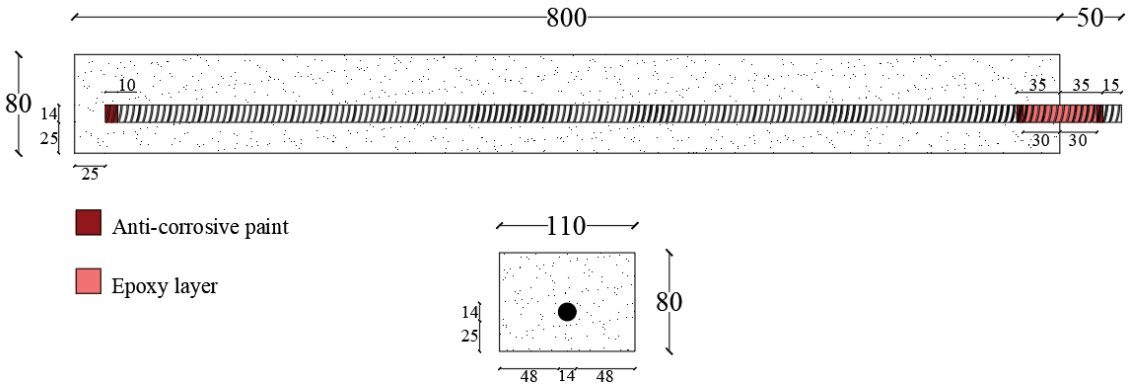

Figure 19: Layout of Reinforced concrete specimens [mm]

3.1.2 Concrete mixture

In the concrete mixture used for all samples, chlorides were added by incorporating salt (NaCl) in an amount of 0.4% [by weight of cement]. This percentage represents the maximum chloride content allowed by the standards EN 206 26 [12].

Table 4: Specimen concrete mixture

Materials	Quantities	unit
Aggregates	1270	kg/m^3
Sand	620	kg/m^3
CEM I 52.5 N	350	kg/m^3
Water	164	kg/m^3
Total (concrete)	2404	kg/m^3

Based on the values in Table 4, the water-to-cement ratio (w/c) is calculated to be 0.47 and the cement-to-concrete ratio is equal to 0.15.

3.1.3 Concrete casting

In the concrete casting process, all the specimens were produced over the course of four different days. The initial step involved preparing of wooden moulds, as depicted in Figure 20 (a). Subsequently, the rebars were coated with the anti-corrosive paint and inserted into the moulds, as shown in Figure 20 (b). During concrete pouring, the embedded part of the rebars was supported by a rebar spacer of 30 mm. To prevent lateral movement of the rebars during the pouring, a thin steel plate was placed on the mould and removed in the end of the pouring process, as illustrated in Figure 20 (d).

The concrete mixture process was performed according to EN 12390-1 [54] and followed these steps:

1. Salt was added to the water.
2. Aggregates and sand were mixed for 60 seconds.
3. Half of salt-water mixture was added to the mixture, which was then mixed for 120 seconds.
4. The mixer was stopped for 120 seconds for safety reasons.

5. Mixing resumed for an additional 30 seconds.
6. Cement was added to mixture and mixed for 30 seconds.
7. The remaining salt-water mixture was added, and a final mixing of 150 seconds was performed.

Once the concrete matrix was prepared, it was poured into the moulds and compacted using vibration. After achieving a smooth surface through trowel finishing, the specimens were placed in a curing room for 28 days. The curing conditions maintained a temperature of 20° and a Relative Humidity (RH) of 95% to facilitate proper concrete strength development over the curing period.

Figure 20: Casting process photographs: (a) Mould; (b) Rebar; (c) Concrete mixture preparation; (d) Rebar placed on the mould; (e) Concrete mixing; (f) RC specimens

3.1.4 Concrete strengths

In order to assess the mechanical characteristics of the reinforced concrete samples, three cubic specimens, each with dimensions of 150 mm each side, and three prism-shaped samples, with dimensions of 150 mm x 150 mm x 600 m, were cast.

From the cubic specimens, the compressive strength was determined, resulting in a mean value of 1557.7 kN and a standard deviation of 65.1 kN, as shown in Figure 21.

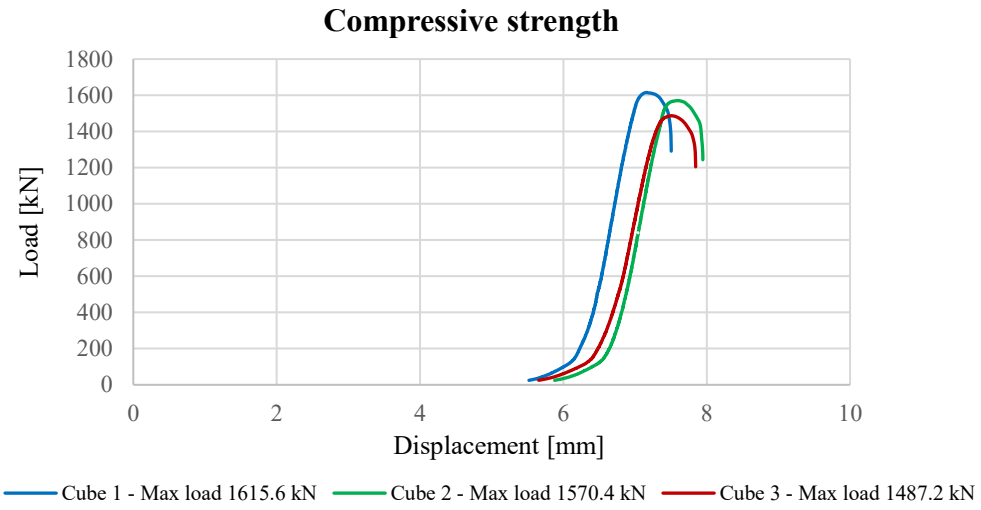

Figure 21: Cubic compressive strength

Considering the cross-sectional area of the specimens (A = 22500 mm^2), the cubic compressive strength ($F_{c,cub}$) was calculated as 69.2 MPa. By using the relationship between cubic and prism compressive strength ($F_{c,prism}$), the prims compressive strength was found to be 54.7 MPa.

The tensile strength was evaluated using the prism-shaped samples, yelding a mean value of 30.8 kN and a standard deviation of 0.1 kN, as shown in Figure 22.

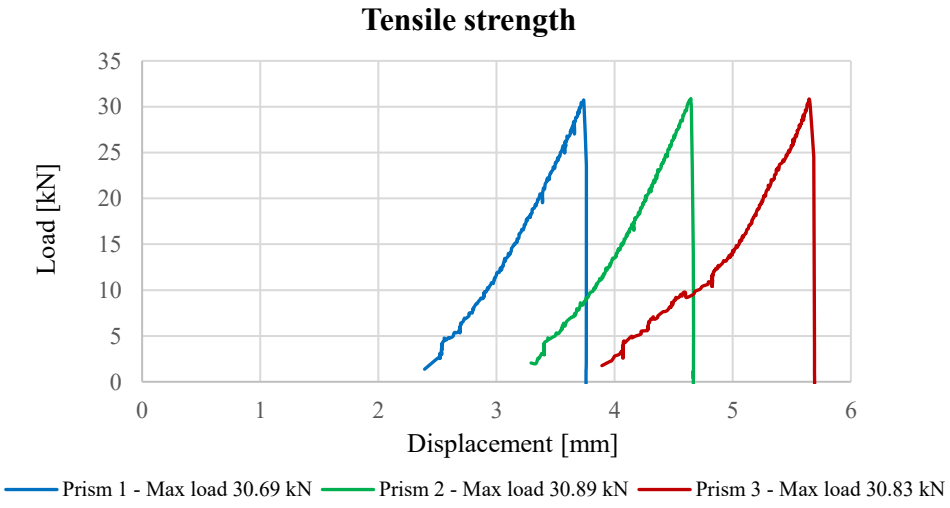

Figure 22: Prism tensile strength

With the cross-sectional area of the specimens, the prism tensile strength ($F_{t,prism}$) was determined as 1.4 MPa.

Next, the characteristic shear strength (V_{rk}) for elements that do not require shear reinforcement and bending strengths were calculated using the formulas provided by Eurocode 2 [55].

For the shear strength, the formula adopted is as follows:

$$V_{Rk} = \left[C_{Rk,c}\, k\, (100\, \rho\, f_{ck})^{\frac{1}{3}} + k_1\, \sigma_{cp}\right] b_w\, d \tag{3.1}$$

The parameters used are listed and described in Table 5.

Table 5: Shear strength parameters

Symbol	Values	Units	Description
$V_{Rk,c}$	10.31	kN	Characteristic shear strength
k	3.08	-	Constant
d	48.00	mm	Effective depth of a cross section
ρ	0.03	-	Reinforcement ratio for longitudinal reinforcement
b_w	110.00	mm	Smallest width of the cross-section in the tensile area
$C_{rd,c}$	0.12	-	Constant
fck,cyl	54.69	MPa	Characteristic compressive cylinder strength of concrete at 28 days
σ_{cp}	-	MPa	Compressive stress in the concrete from axial load
k_1	0.15	-	Constant

From the calculations, V_{rk} was found to be 10.31 kN, indicating a maximum point load of P = 2 V_{rk} = 20.61 kN for the 3-point bending test.

For the bending strength, the formula adopted is as follows:

$$M_{Rk} = \mu_{Rd}\, \mathrm{b}\, \mathrm{d}^2 \sigma_{cd} \tag{3.2}$$

The parameters used in this calculation are listed and described in Table 6:

Table 6 Bending strength parameters

Symbol	Values	Units	Description
M_{Rk}	3.54	kNm	Characteristic bending strength
μ_{rd}	0.26	-	Non-dimensional bending strength
d	48.00	mm	Effective depth of a cross-section
b	110.00	mm	Overall width of a cross-section
σ_{cd}	-	MPa	Design compressive stress

M_{rk} was determined to be 3.54 kNm, resulting in a maximum theoretical load of P = 4 M_{rk}/L = 18.89 kN to be applied during the 3PBT.

Therefore, the minimum of both strengths was taken to avoid collapse, leading to a maximum theoretical load of P = min {19.84 kN, 18.77 kN} for the 3PBT.

3.2 Cracking of the samples

After the 28-day curing period, the samples underwent refence measurements by applying DEMEC points. These points were placed on the face of the samples that were subjected to cracking (tension) during the 3PBT. Two rows of ten points

distributed longitudinally along the samples, as shown in Figure 23. The DEMEC points were positioned along the contour this face, allowing for the monitoring of longitudinally formed corrosion cracks. A digital dial gauge with a fixed and a movable conical point was used to measure the distance between the points. The reference span was set at 100 mm, measured on an Invar bar. This monitoring system enabled the continuous tracking of the mechanical cracks throughout the experimental work, which was crucial as these cracks could widen due to corrosion.

Figure 23: DEMEC-points application

To create cracks on the samples, 3-point bending test was performed. This test involves applying a concentrated load to the center of a simply supported specimen, resulting in the maximum bending moment at that point, as depicted in Figure 24. The initial tests were conducted at the laboratory of Civil Engineering department at KU Leuven.

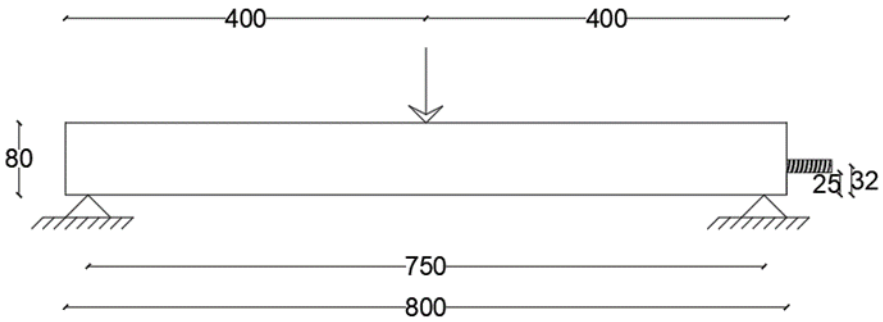

Figure 24: 3-Point bending test setup [mm]

During the testing, a Linear Variable Displacement Transducer (LVDT) was utilized to monitor the main crack width in the central region of the samples, as shown in Figure 25. This LVDT device was connected to a computer, enabling real-time monitoring of the crack width in the central area throughout the test.

Figure 25: LVDT application in the middle of the specimen

As first step, the four cracked specimens were tested, loaded in three loading steps, and the following results were obtained:

Table 7: Test results for C1, C2, C3, C4

Specimen	Maximum load [kN]	Crack width under loading [mm]	Crack width after relaxation [mm]
C1	17.50	0.72	0.16
C2	17.26	1.00	0.18
C3	16.63	0.72	0.18
C4	17.00	1.16	0.22

Figure 26 shows a comparison between the tests conducted for samples C3 and C4.

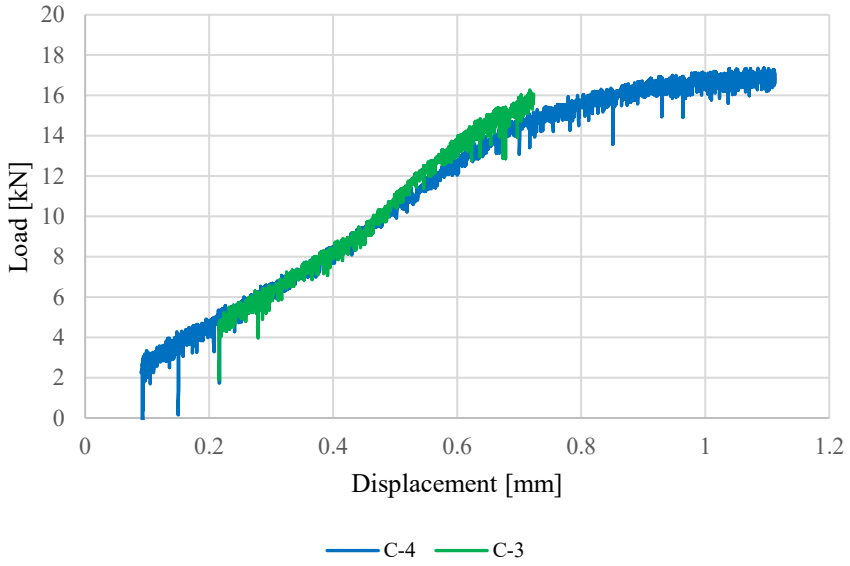

Figure 26: 3-Point Bending test results for samples C3 and C4

The load-displacement graph reveals that specimen C4 underwent a larger plastic stage compared to C3, resulting in a more substantial crack width after the test. However, to ensure safety and prevent unexpected collapse, the test for specimen C3 was stopped with a slight smaller load than the maximum load used for C4.

Following the test for the cracked specimens, the notched specimens were tested. Two different notch sizes were used:

- One specimen had a notch size of approximately 0.6 mm wide and 0.6 mm deep.
- The other two specimens had a notch size of approximately 1.5 mm deep and approximately 1.8 mm wide. These notches were designed to accommodate an object on either side of the notch, which could block the closure of the crack after loading and facilitate chloride ingress. The deeper notches were used because the first specimen with a smaller notch exhibited the main crack not in correspondence to the notch. Lengthening the notches ensured that the crack would form in the middle as intended.

The results of the 3-point bending test for the notched specimens are presented in Table 8:

Table 8: Test results for CN1, CN2, CN3

Specimen	Maximum load [kN]	Crack width under loading [mm]	Crack width after relaxation [mm]
CN1	16.30	0.97	0.32
CN2	16.30	0.70	0.32
CN3	17.00	1.31	0.75

The first notched specimen tested was CN3, and it underwent a total of five load steps. In the last step, the specimen reached the full plastic phase, resulting in an incredibly larger crack width than the others, as seen Figure 27. Specifically, two large crack widths formed in the central area of the specimen, as shown in Figure 34, but none in the notched section.

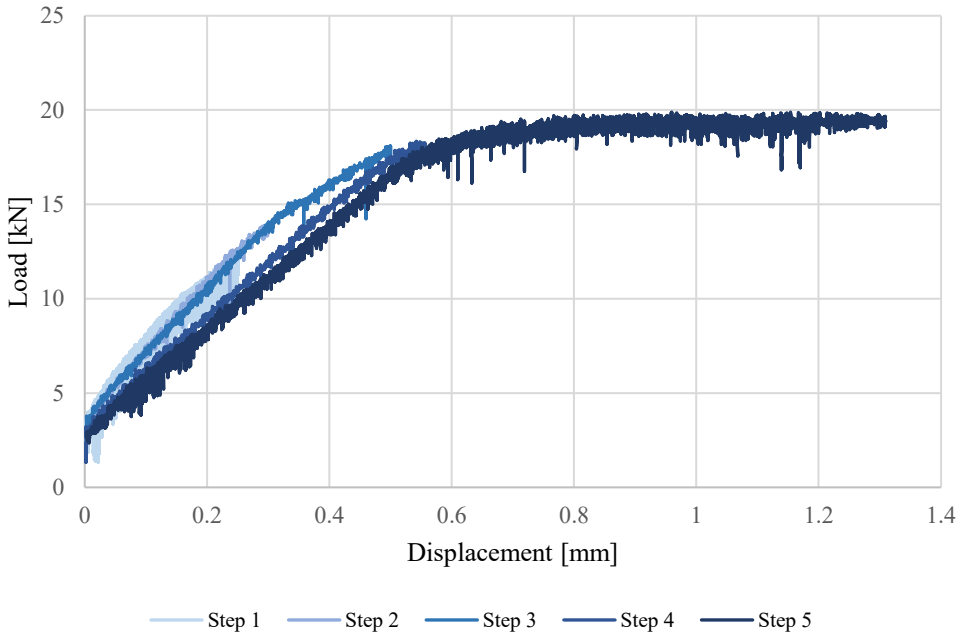

Figure 27: 3-Point bending test results for CN3

As a result, the other two specimens (CN1 and CN2) were notched differently. For these two samples, a pair of rigid plastic pieces, each 3.2 mm thick, were placed at the sides of the notch to a depth of 10 mm within the notch during testing. This was done to obstruct the closure of the crack after relaxation, as illustrated in Figure 32

and Figure 33. In the case of specimen CN1, local crushing was observed due to the application of these plastic objects.

After a few days of relaxation, the main *mechanical* crack widths were measured at four different transversal locations, yielding the following results:

Table 9: Summary of samples and main mechanical crack width values

Specimen	Mean crack width value [mm]	Standard deviation [mm]
C1	0.09	0.025
C2	0.13	0.029
C3	0.14	0.025
C4	0.24	0.025
CN1	0.32	-
CN2	0.32	-
CN3	0.75	-
UC1	-	-
UC2	-	-

Finally, at the end of the tests, the following deformed configurations of the specimens were obtained:

C1:

- 7 transversal cracks along its length, with a main crack width of 0.16 mm and a second-largest crack near the centre of 0.1 mm.
- Total aperture due to the sum of transversal cracks: approximately 0.42 mm.
- longitudinal cracks away from the central section, with a width between 0.02 and 0.04 mm.

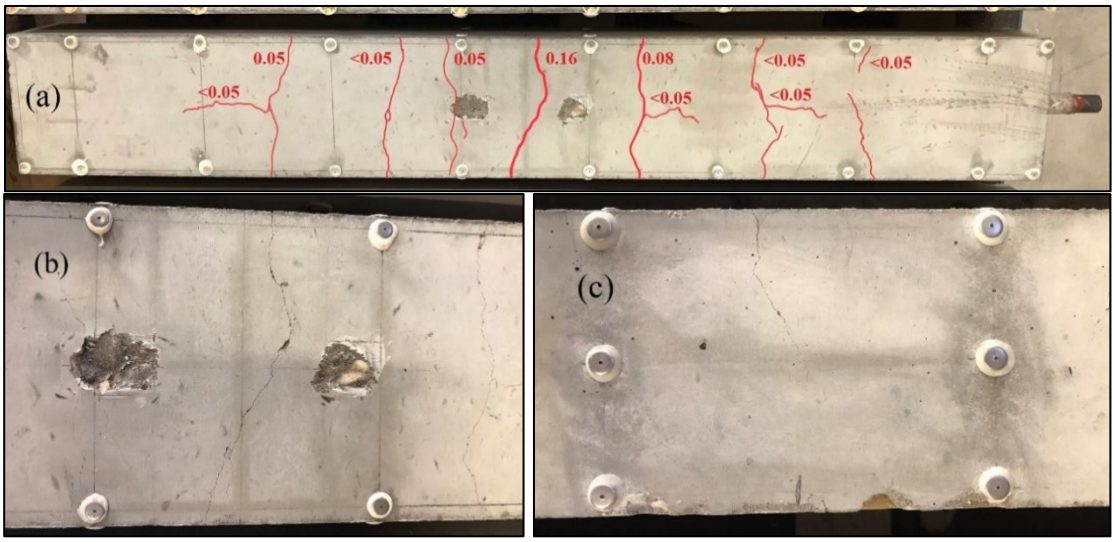

Figure 28: C1 cracks configuration: (a) Mapping, (b) Main crack top view, (c) Main crack lateral view

C2:

- 7 transversal cracks with a main crack width of 0.18 mm and a second-largest crack around the centre of 0.08 mm.
- Total aperture due to the sum of transversal cracks: about 0.45 mm.
- longitudinal cracks (not in the central area) with a width between 0.02 and 0.03 mm.

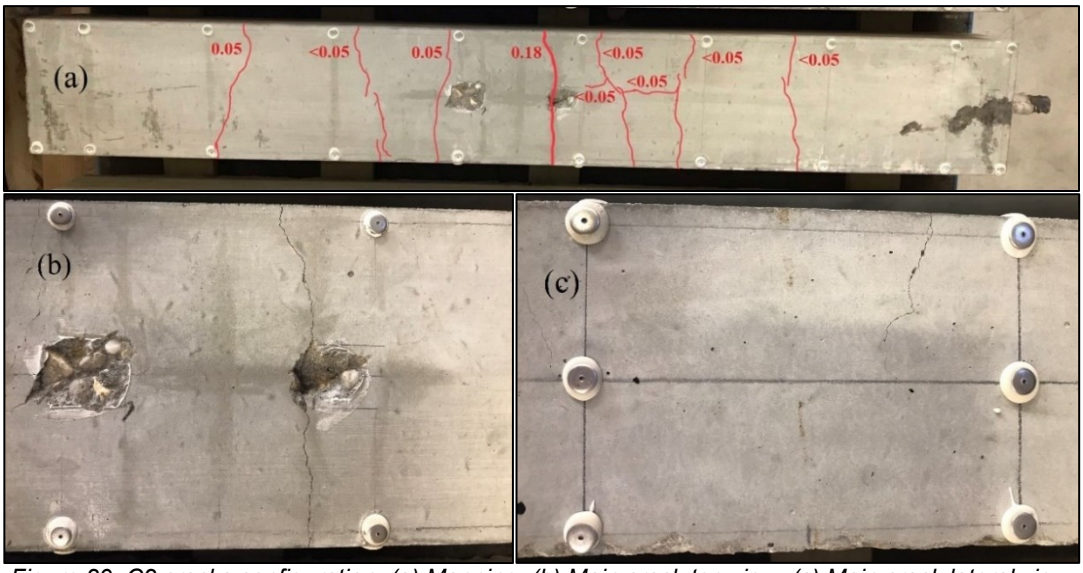

Figure 29: C2 cracks configuration: (a) Mapping, (b) Main crack top view, (c) Main crack lateral view

C3:

- 7 transversal cracks with more bifurcations than previous samples.
- Main crack width in the center: 0.18 mm, second largest (near the center): 0.07 mm.
- Total aperture due to the sum of transversal cracks: around 0.46 mm.
- longitudinal cracks (not in the central area) with a width of 0.05 mm on the left-hand side and 0.02 mm on the right-hand side.

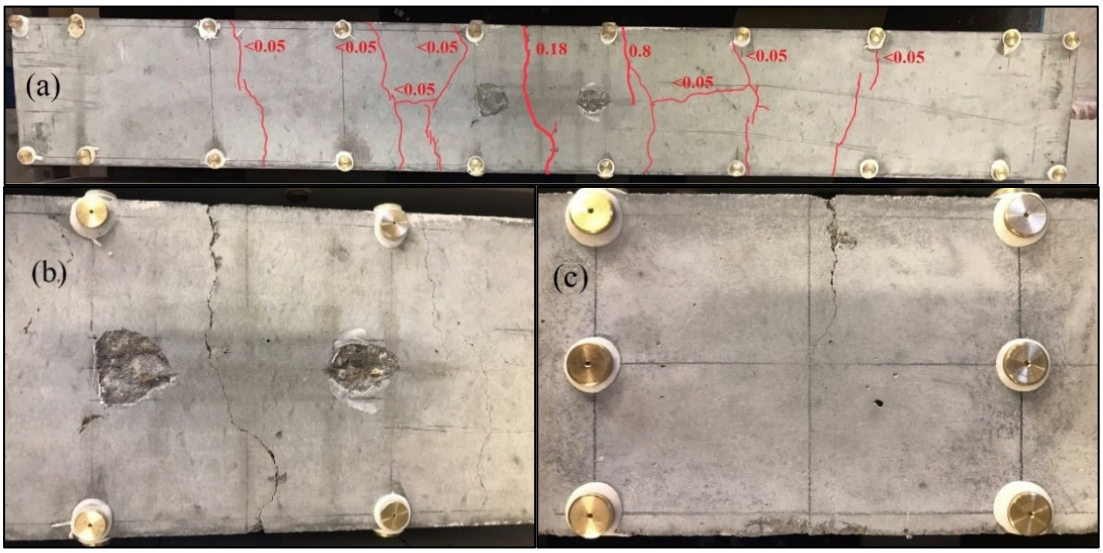

Figure 30: C3 cracks configuration: (a) Mapping, (b) Main crack top view, (c) Main crack lateral view

C4:

- 8 transversal cracks with a main crack width of 0.22 mm and a second largest of approximately 0.10 mm.
- Total aperture due to the sum of transversal cracks: about 0.49 mm.
- short longitudinal cracks, both approximately 0.03 mm wide.

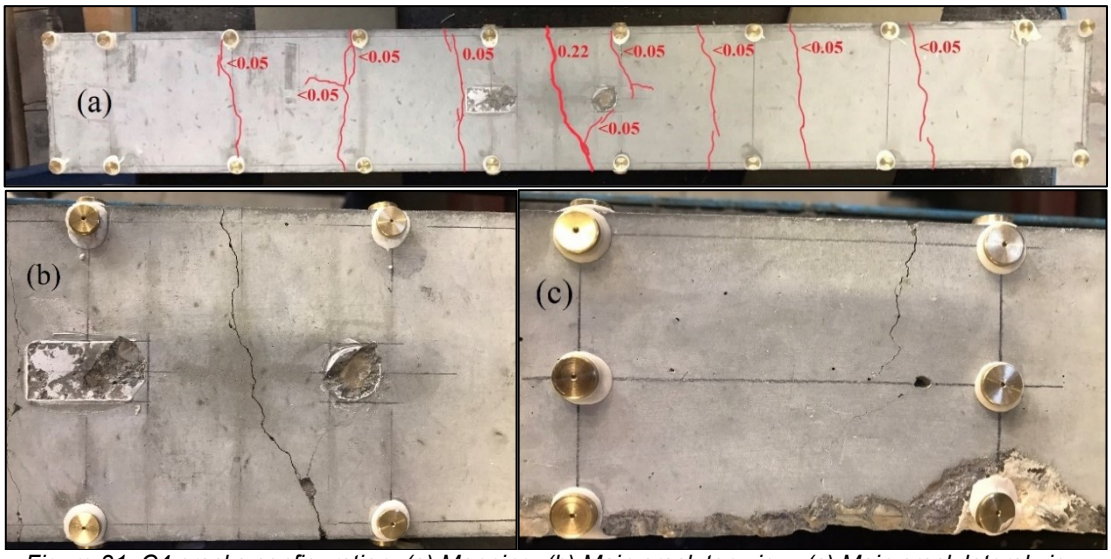

Figure 31: C4 cracks configuration: (a) Mapping, (b) Main crack top view, (c) Main crack lateral view

CN1:

- 5 transversal cracks and 3 longitudinal cracks in the center.
- Main crack width in the center: 0.32 mm, second largest: approximately 0.07 mm.
- Total aperture: around 0.54 mm.
- Longitudinal crack at the LVDT application site (0.15 mm wide) likely resulted from device removal.

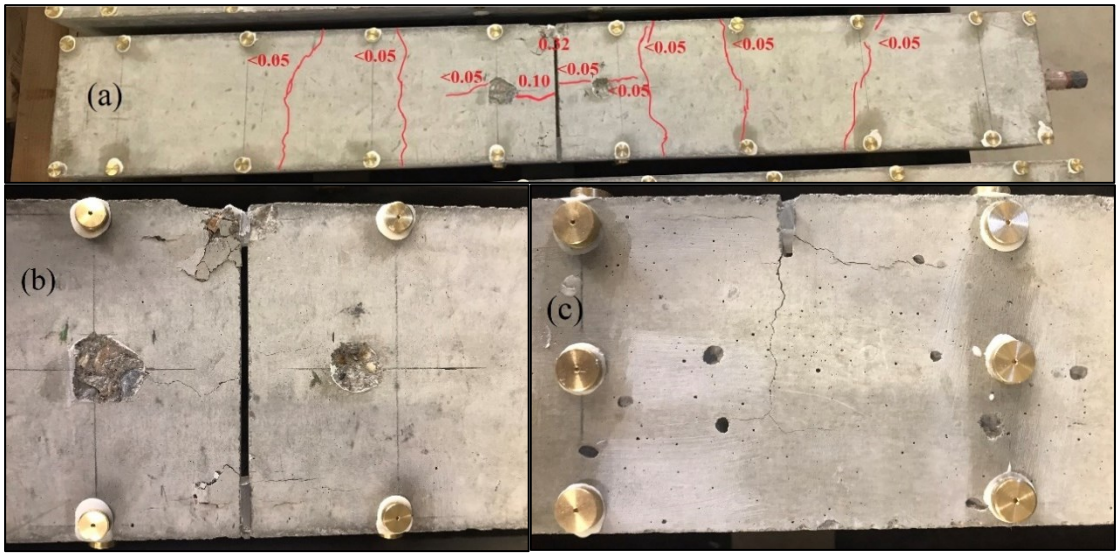

Figure 32: CN1 cracks configuration: (a) Mapping, (b) Main crack top view, (c) Main crack lateral view

CN2:

- 5 transversal cracks and 6 longitudinal cracks (specimen with the most longitudinal cracks).
- Main crack width in the center: 0.32 mm, second largest: approximately 0.05 mm.
- Total aperture due to the sum of transversal cracks: about 0.53 mm.

- Widest longitudinal crack in the central section: 0.25 mm, other longitudinal cracks varied between 0.03 and 0.08 mm.

Figure 33: CN2 cracks configuration: (a) Mapping, (b) Main crack top view, (c) Main crack lateral view

CN3:

- 5 transversal cracks and 5 longitudinal cracks.
- Main crack width in the center: 0.75 mm (largest transversal crack width among all specimens), second largest: approximately 0.45 mm.
- Total aperture: around 1.39 mm.
- No longitudinal cracks in the central area, longitudinal crack widths varied between 0.03 and 0.08 mm.

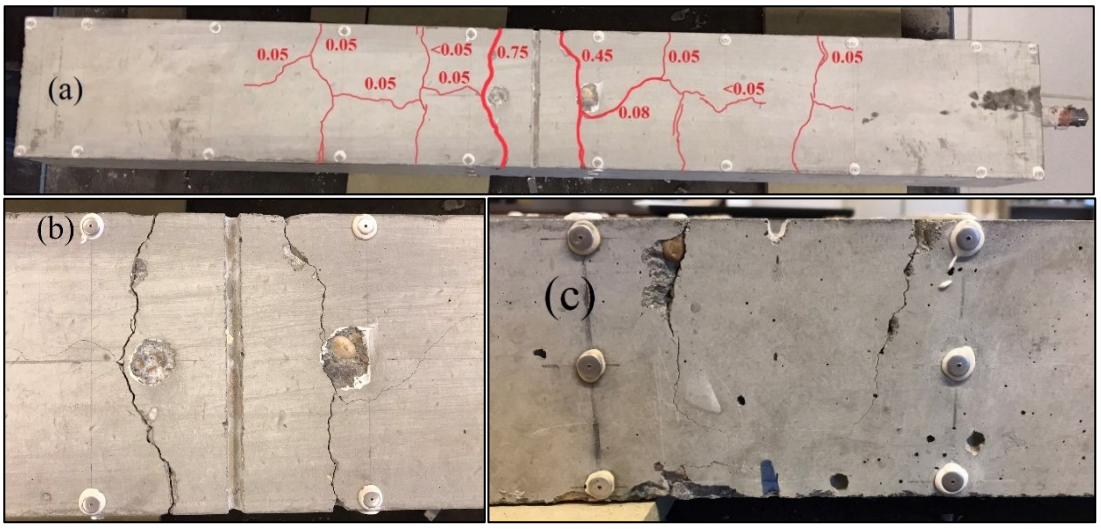

Figure 34: CN3 cracks configuration: (a) Mapping, (b) Main crack top view, (c) Main crack lateral view

3.3 Natural corrosion setup

After the 3-point bending test, the specimens were placed in a corrosion setup structure to investigate chloride-induced corrosion.

The setup consists of three main parts:

- A cubic tank with a volume of 800 L, where a solution of water and 3.5% salt was stored (Figure 35 (b)).
- Tubes through which water containing chlorides flows from the tank to the steel structure (Figure 35 (c)).
- A steel structure measuring 2.25 x 2.25 x 1.20 m with five floors. The tubes are attached to the top of each floor, allowing the water containing chlorides to spread over the samples placed on the floors. At the bottom of the structure, there is a water collector with a capacity of 700 L (Figure 35 (a) and (d)).

The entire corrosion setup was designed by the PhD student and daily supervisor of this thesis research, Constantijn Martens, at the Civil Engineering department of KU Leuven.

Figure 35: Natural corrosion setup: (a) Entire corrosion setup, (b) Tank, (c) Tubes, (d) Metallic structure

The corrosion process began 77 days after casting the samples. It involves spreading water containing chlorides on the surface of each specimen. The solution is distributed daily for 90 seconds, after which the samples remain dry for the rest of the day. The corrosion setup simulates the exposure categories listed by the Eurocode [55]:

- XD3, corrosion induced by chlorides – cyclic wet and dry
- XS3, corrosion induced by chlorides from seawater – tidal, splash and spray zone, see Figure 7.

In both cases, wetting and drying cycles occur, creating a highly aggressive environment for the corrosion of reinforced concrete. Considering that the initial chloride content of 0.4% by weight of cement added during the casting process, the corrosion process is expected to be fast.

It is important to note that corrosion process in this setup is natural, allowing for capillary suction and migration as transport mechanisms of chlorides inside the concrete matrix, leading to a natural depassivation of the steel reinforcement. This process would not be possible with current applied methods (accelerated corrosion setups).

Furthermore, the environment inside the structure is designed to have a large RH, favouring the corrosion process, and it is not saturated thanks to the circulation of air in the open space between the glazed facade of the structure and the container at the bottom.

3.4 Overview of the experimental tests

The experimental test conducted on the reinforced concrete samples can be summarized as follows:

Placement in corrosion setup: After 77 days of casting the samples, they were placed in the corrosion setup structure. The setup involved spreading water containing chlorides on the cracked surface of each specimen in a cyclic wet and dry environment.

Laboratory Monitoring: The laboratory monitoring process was carried out once a week for a total of 18 weeks (124 days). This continuous observation provided data on the progression of the corrosion process and the behavior of the samples.

Galvanostatic Pulse Technique: The corrosion potential, corrosion current density and corrosion rate were monitored using Galvanostatic Pulse technique, providing insights into the corrosion behavior of the steel reinforcement.

Demec points, Microscope and Crack Ruler: The Demec points, microscope, and crack ruler were utilized to monitor and measure the crack width on the samples. This allowed for the observation of crack development and changes over time.

Chloride Content and Mass Loss Measurement: After 75 days of initial exposure, chloride content and mass loss of the reinforcement were measured by taking concrete cores and extracting the reinforcement steel from the corroded samples.

However, due to time constraints and the slow process of natural corrosion, only two samples were chosen for this measurement, while the others were kept under observation for potential future experimental works in the department.

Overall, the experimental tests provided important data on the corrosion behavior of the reinforced concrete samples under different conditions, shedding light on the crack development, chloride ingress, and mass loss of the reinforcement.

Chapter 4: Corrosion parameters

As indicated in Sections 2.2 and 2.3 the Chloride Diffusion Coefficient (CDC), chloride content, and corrosion rate play a crucial role in modelling and predicting the corrosion process. In this chapter, a prediction and analysis of these parameters are conducted.

4.1 Chloride Migration Coefficient

In Section 2.3 it was mentioned that the CDC is assessed using the Nord test, conducted at the chemistry laboratory of the Civil Engineering Department at KU Leuven. This assessment took place 80 days after the casting of the specimens. This test, following the standard "NT build 492" [42], allows for the evaluation of the Chloride Migration Coefficient (CMC or D_{RCM} [m^2/s]). Based on this coefficient, the apparent diffusion coefficient can be determined.

The experimental setup involves three cylindrical drilled cores with a diameter of 100 mm and a thickness of 50 mm. These cores are placed in a basin after which an external electrical potential is applied axially across the specimens, promoting the migration of chloride ions. This setup is shown in Figure 36. After the migration of chloride ions, a splitting test is performed on the cores to provide two surfaces for measuring the penetration depth.

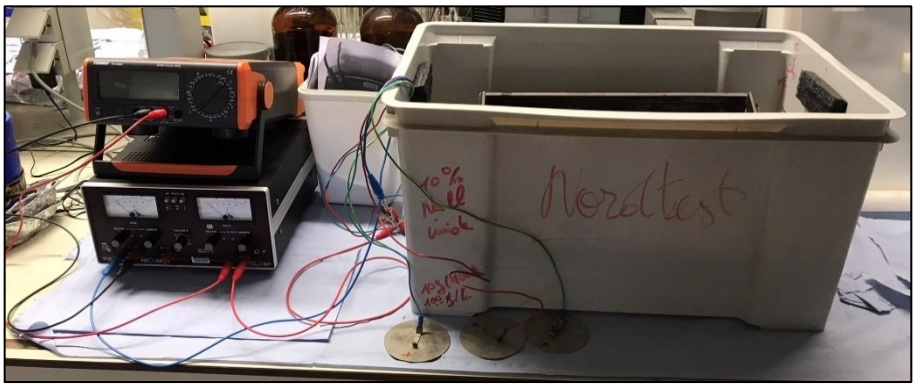

Figure 36: Nord Test setup

The value of the CMC is determined using various parameters, as described by Equation (4.1):

$$D_{RCM} = \frac{RT}{zFE} * \frac{x_d - \alpha\sqrt{x_d}}{t} \quad (4.1)$$

In this equation, D_{RCM} is expressed in units of [m^2/s], the parameter *z* represents the absolute value of the ion valence for chlorides (*z=1*). *F* [-] denotes the Faraday constant, *R* [-] is the gas constant, *T* represents the average temperature in the anolyte solution, expressed in Kelvin [K], *t* corresponds to the test duration in seconds [s] and x_d [m] represents the chloride penetration depth resulting from electrical migration. For a detailed understanding of the other parameters, reference is made to “NT build 492” [42].

To determine the value of x_d, three samples (cores) were examined. After the Brazilian splitting test, six longitudinal surfaces were obtained. The chloride penetration can be clearly observed on the split surfaces, displaying a white/silver colour due to the application $AgNO_3$. These areas are highlighted in red in Figure 37.

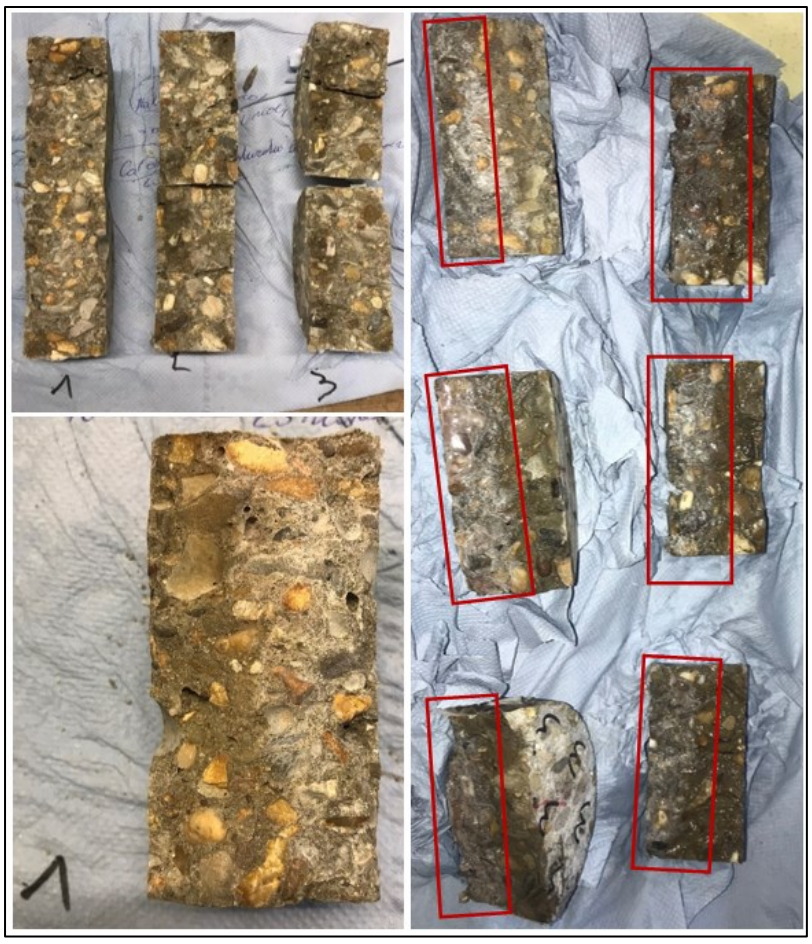

Figure 37: Chloride penetration depth measurement

Finally, the penetration depth is measured using a caliper and the following results are obtained:

Table 10: Nord Test - chloride penetration results

Specimen	Mean value μ [mm]	Standard deviation σ [mm]
1A	27.40	3.37
1B	27.22	3.31
2A	27.27	2.92
2B	29.21	2.40
3A	26.30	1.67

3B	26.71	1.38
Average	**27.35**	2.51

Consequently, the obtained results follow the following normal distributions:

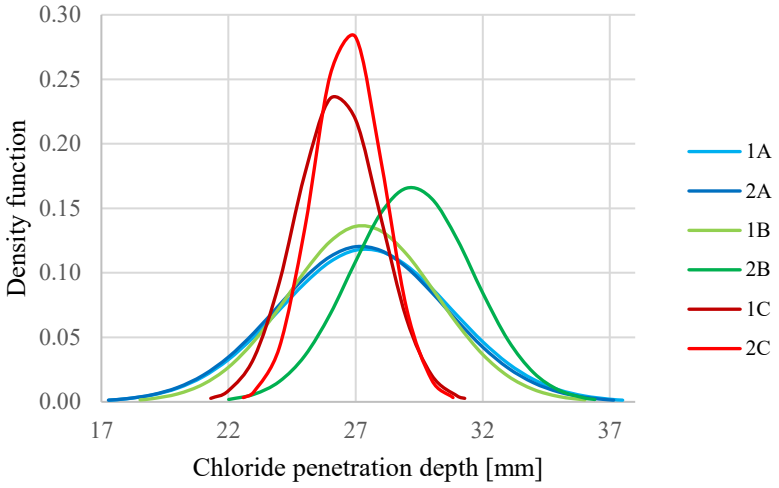

Figure 38: Normal distributions of chloride penetration depth for the split samples faces (A and B)

It is noticeable that determining the penetration depth is not straightforward as each specimen exhibits slight variations in the average value. However, according to Table 10, the overall chloride penetration depth corresponds to *27.35 mm*.

Thus, the value of the experimental chloride migration coefficient ($D_{RCM,e}$) at the Nord-test time-day (80 days), calculated using Equation (4.1), is as follows:

$$D_{RCM,e} = 1.277 * 10^{-11}\ m^2/s \tag{4.2}$$

This will be utilized in Section 4.2 to evaluate the Chloride Diffusion Coefficient.

The “fib-bulletin 76” code [40] provides a pre-established normal distribution for D_{RCM}, specifically based on the cement type (CEM I, CEM II, etc.) and the water-to-cement ratio (w/c). By considering CEM I with a *w/c=0.47*, the theoretical chloride migration coefficient ($D_{RCM,t}$) at the first exposure time t_0 (77 days) value is determined:

$$D_{RCM,t}(t_0) = 1.216 * 10^{-11}\ m^2/s \tag{4.3}$$

It is worth noting that the difference between the theoretical and experimental values is less than 5%, indicating a satisfactory level of agreement.

4.2 Chloride Diffusion Coefficient

As described in the literature Section 2.4, the CMC specifically relates to the migration of chloride ions under the influence of an electrical field. However, to account for the natural diffusion of chloride ions in response to concentration gradients, the Chloride Diffusion Coefficient (CDC) needs to be calculated.

Based on the experimental value of the CMC, Equation (2.10) is utilized to determine the Apparent chloride diffusion coefficient over time ($D_{app}(t)$), as illustrated in Figure 39. The time figure displays two additional vertical functions representing the time

first exposure time (77 days after casting process) and the time when the experimental work for this thesis concluded, namely the inspection time (152 days after casting process). Notably, the coefficient decreases over time due to the ageing coefficient "*a*", see Equation (2.10), as the ongoing hydration process reduces the pore structure, and continued chloride ingress can result in a pore-blocking effect [40].

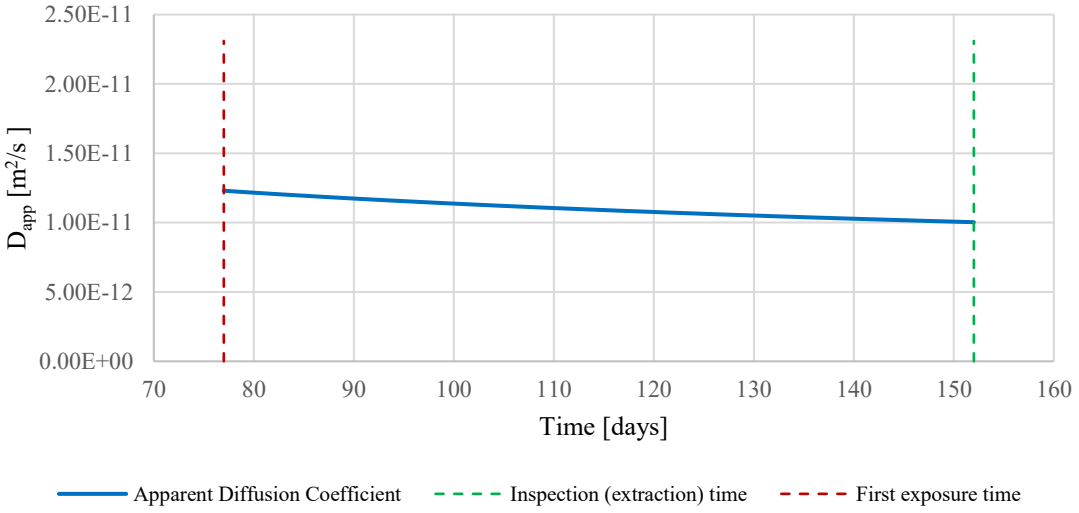

Figure 39: Apparent Diffusion Coefficient over time

The value of the Apparent Diffusion Coefficient, which is also considered as the Chloride Diffusion Coefficient due its time-dependent behaviour, holds significant importance in corrosion process models.

To determine the chloride content and corrosion rate models, it is essential to have a value for D_{app}. This coefficient is evaluated at the inspection time, which corresponds to the time when samples C4 and CN3 were subjected to rebar extraction and core drilling. The inspection time was 75 days after the initial exposure time (152 days after sample curing). Hence, by using Equation (2.10) and the experimental chloride migration coefficient ($D_{RCM,e}$) the following value of D_{app} is obtained:

$$D_{app} = 1.041 * 10^{-11}\ m^2/s \tag{4.4}$$

Appendix A1 provides a more detailed explanation of the parameter values along with their respective distributions.

4.3 Chloride content

After calculating D_{app}, the chloride content model is determined using the ERFC-Solution with Time-Dependent D_{app}, as represented by Equation (2.15). For this thesis's experimental work, a short-term analysis is required. However, it is essential to consider the chloride surface concentration (C_s) when examining chloride-induced corrosion in marine environments. As discussed in Section 2.3, C_s depends on various factors, including wind speed, distance from the coast, exposure time and water-to-cement ratio.

The corrosion setup, explained in Section 3.4, aims to simulate the chloride-induced corrosion in marine environments' tidal zone. In this setup, the samples inside the structure are daily wetted with sprayed water containing salt. Consequently, the mathematical formula that better describes the chloride penetration mechanics of this corrosion setup should be more closely related to the tidal and splash zones in marine environments rather than the submerged and atmospheric zones. Therefore, wind speed and distance from the coast are not considered significant factors. Instead, exposure time and w/c are identified as the main influencing parameters for C_s.

The mathematical formula considered is described by Equation (2.19) as reported in Section 2.3:

$$C_{s,conc} = \left(0.257\frac{w}{c} + 0.254\right) t^{0.383} \rightarrow \quad C_{s,conc} = 0.20\ \% \tag{4.2}$$

In this equation, t is the final inspection time of 75 days from the first exposure, which corresponds to the date when the two samples were subjected to rebar extraction and core drilling, moreover C_s is expressed in mass percentage of chloride to concrete, therefore a transformation to mass percentage of chloride to cement is necessary, considering the cement-to-concrete ratio of 0.146 given by Table 4:

$$C_{s,cem} = 1.40\ \% \tag{4.2}$$

Once C_s is calculated, the chloride content at an inspection time t can be evaluated over the depth.

Based on the result, to gain insight into the corrosion risk levels by the predictive model, the following four models are presented in Table 11.

Table 11: Chloride content by weight of cement - Risk levels (adapted from [56])

Total chloride content [by weight of cement]	Corrosion risk
≤ 0.2 %	Negligible
0.2 - 0.4 %	Low
0.4 - 1 %	Moderate
> 1 %	High

The chloride content-penetration depth curve is visually represented in Figure 40:

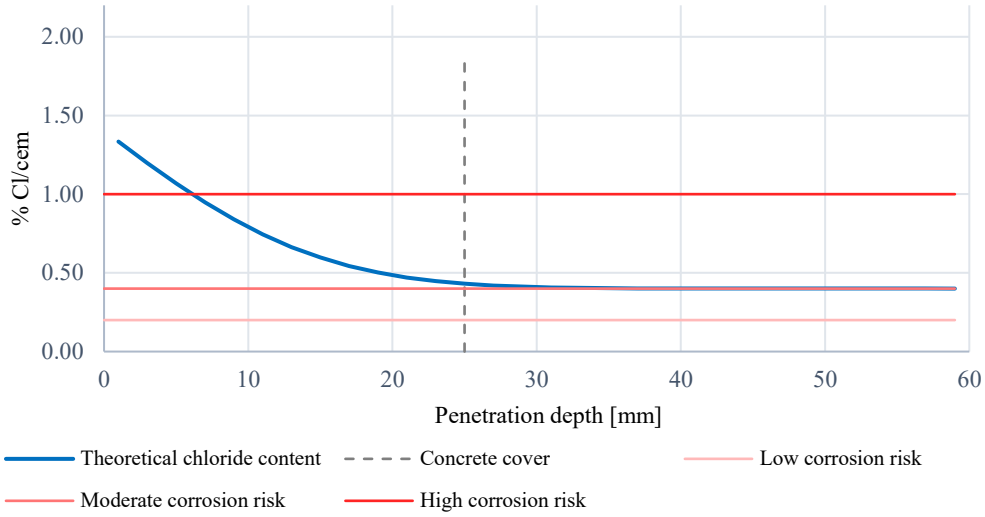

Figure 40: Theoretical chloride penetration curve at time t=77 days

The obtained curve demonstrates that the chloride content decreases with increasing distance from the surface of the RC samples. At the reinforcement depth, a predicted amount of 0.43% is found.

Furthermore, an estimation of moderate corrosion risk can be anticipated, considering the provided chloride content.

Another interesting analysis concerns the chloride content's behavior over time at the concrete cover depth. By considering the initial exposure time (t_0) as 77 days and observing a period of one year (until 442 days), the incremental penetration curve can be observed through the theoretical model, as depicted in Figure 41:

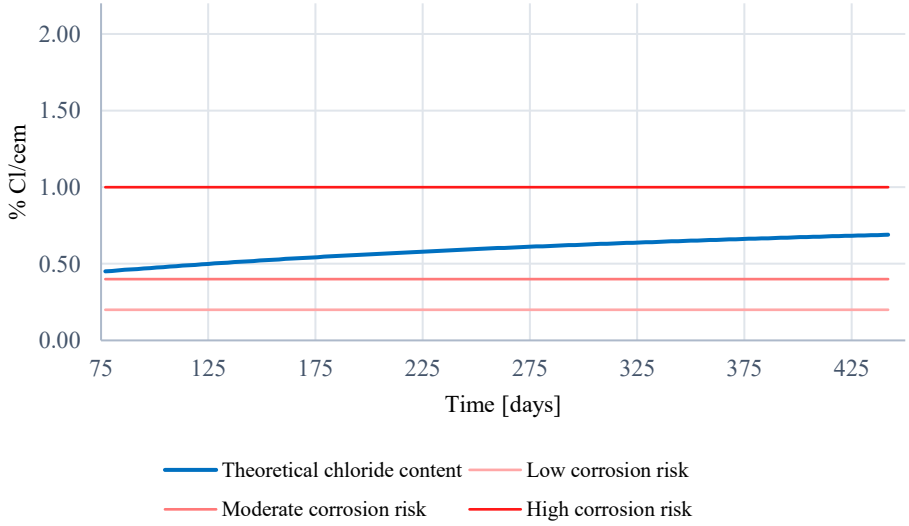

Figure 41: Theoretical chloride penetration curve at depth x=25 mm

The figure illustrates the progressive increase in chloride content at the reinforcement surface. Unlike the previous case where D_{app} remained fixed at the extraction time (152 days), this curve shows D_{app} as variable over time. Remarkably, even after one year, the chloride content at the concrete cover depth is still insufficient to pose a high risk of corrosion.

It is essential to note that the presented curves are specifically applicable to RC concrete surfaces without cracks. The formula is based on analyzing the natural diffusion mechanism that occurs within the concrete matrix. However, for cracked specimens, the presence of cracks significantly facilitates chloride ingress, to the extent that the initiation stage is typically considered negligible.

4.4 Corrosion rate

Another important parameter for describing the corrosion process is the corrosion rate. In Section 2.2, the model from Otieno [35] is presented to predict the corrosion rate for cracked samples. This model is primarily influenced by concrete cover, crack width and chloride diffusion coefficient. By applying this model, it becomes possible to obtain a theoretical value of the corrosion rate in the main crack zone for all the cracked samples.

Due to the very short exposure time for the uncracked samples, the likelihood of corrosion occurrence is significantly reduced. As a result, no corrosion rate models were applied to uncracked samples.

Furthermore, the model is based on two sets of results: one from the natural corrosion setup and the other from the accelerated corrosion setup. By utilizing Equations (2.11) and (2.12), the parameters k_2 [µA/cm^2] and A_2 [-] can be calculated:

$$k_2 = \begin{cases} 5.180 & lab\ (l) \\ 0.640 & field\ (f) \end{cases} \tag{4.5}$$

$$A_2 = \begin{cases} 266.754 & lab\ (l) \\ 0.210 & field\ (f) \end{cases} \tag{4.6}$$

After taking into account the different transversal crack widths in the main zone of the samples, the theoretical corrosion current density can be calculated using Equation (2.13) and subsequently reported in Table 12.

Table 12: Theoretical corrosion rates

Specimens	$i_{corr,field}$ [µA/cm^2]	$i_{corr,lab}$ [µA/cm^2]	$V_{corr,field}$ [mm/year]	$V_{corr,lab}$ [mm/year]
C1	0.205	0.000	0.002	0.000
C2	0.222	0.000	0.003	0.000
C3	0.209	0.000	0.002	0.000
C4	0.235	0.000	0.003	0.000
CN1	0.259	0.000	0.003	0.000
CN2	0.287	0.000	0.003	0.000
CN3	0.305	0.000	0.004	0.000

The last two columns on the left represent the corrosion penetration for both the natural and accelerated corrosion setups. These values are obtained by using the corrosion current density in Equation (2.23).

However, it is evident that the laboratory values are null, indicating a possible error in the formulation of $A_{2,lab}$. In fact, from Equation (4.6), it is apparent that $A_{2,lab}$ is two orders of magnitude larger than $A_{2,field}$. This larger value leads to the resulting i_{corr}

being equal to 0. Additionally, it is observed from Equation (2.12) that the form of the equations is different, where the lab parameter is described by a power function, while the field one is described by an exponential function. Consequently, the lab values cannot be considered reliable. Nonetheless, since the experimental setup of this thesis is based on the natural transport mechanism of chloride, the most important theoretical results are those obtained from the field.

To gain a better understand of the level of corrosion predicted by the Otieno model, Table 13 presents four different corrosion levels based on i_{corr} and V_{corr} values.

Table 13:Corrosion current density (i_{corr}) and corrosion penetration (V_{corr}) levels.

i_{corr} [$\mu A/cm^2$]	V_{corr} [*mm/year*]	**Corrosion risk**
≤ 0.1	≤ 0.001	Negligible
0.1 - 0.5	0.001 - 0.005	Low
0.5 - 1	0.005 - 0.01	Moderate
> 1	> 0.01	High

Therefore, with corrosion current density values ranging from 0.2 and 0.3 for all the samples, it can be concluded that the theoretical corrosion level of all the samples is low.

These theoretical results obtained will be compared with the experimental measurements reported in Chapter 5.

Chapter 5: Corrosion monitoring and assessing

The first day of monitoring marks the beginning of the corrosion process by the corrosion setup described in Section 3.4. On this day, the initial measurements were taken.

The measurements conducted during the monitoring process included various electrochemical parameters such as half-cell potential or corrosion potential, corrosion current density and electrochemical resistance using Galvanostatic Pulse. Additionally, crack monitoring was performed to detect transversal cracks resulting from the three-point bending test and potential new longitudinal cracks that may arise due to corrosion product formation throughout the duration of the research.

The monitoring program involved conducting measurements once per week, preferably on the same day of the week and at same time. This approach aimed to maintain consistency throughout the monitoring period, considering that the electrochemical measurements can be significantly influenced by variations in humidity conditions of the samples.

The first step involved moving the samples from the corrosion setup to a table. The top surface of the samples was cleaned to remove any excessive chloride presence that could potentially impact the accuracy of the electrochemical measurements. Special attention was given to cleaning the cantilever part of the rebar, as it represented an exposed area of the steel reinforcement and was particularly susceptible to corrosion. At the end of each monitoring day, this exposed part was covered with a plastic cup sealed with silicon protection.

After cleaning, the surfaces and the rebar, the GalvaPulse measurements were initiated starting from zone 1, see Figure 42. Following the completion of the first set of measurements for all the samples, a mandatory 30-minute interruption was observed. This interruption allowed sufficient time for the anodic area to depolarize after the Pulse emission. During this time, DEMEC measurements were taken.

Once the GalvaPulse and DEMEC measurements were completed, the half-cell potentials were measures. As this step did not involve Pulse emission, it could be completed more quickly. Finally, a thorough visual inspection of the cracks was performed using both a crack ruler and a microscope. This check was conducted before returning the samples to the corrosion setup.

The routine was followed as part of the weekly monitoring process.

5.1 Galvanostatic Pulse monitoring

In the Galvanostatic Pulse monitoring process described in this chapter, four main parameters are measured:

- *Corrosion potential* (E_{corr}): These potentials, measured in millivolts [mV], are monitored together to ensure consistency in the measurements.
- *Electrochemical Resistance* (R_e): This parameter, measured in ohms [Ω], is necessary to evaluate the corresponding corrosion current density, as explained in Section 2.5.
- *Corrosion current density* (I_{corr}): Measured in microamps per square centimeter [$\mu A/cm^2$], the corrosion current density is used in conjunction with the Faraday's law to calculate the corrosion rate (V_{corr}) in millimeters per year [*mm/year*], as described in Equation (2.23).

The Galvanostatic Pulse technique involves confining the current with guard rings, which have a diameter of approximately 70 mm. As a result, the specimens are measured in seven different zones, as depicted in Figure 42. The first and last zones are located furthest from the main transversal crack, while the fourth zone is the central one containing the main transversal crack. This arrangement allows for the observation of differences in response during the corrosion process, providing insight into the temporal and spatial evolution of the main corrosion parameters.

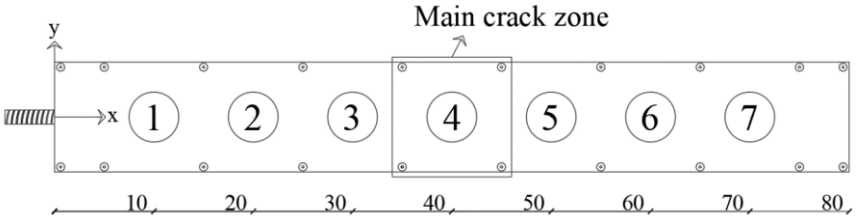

Figure 42: RC-samples subdivision for GalvaPulse measurements

To streamline the report and avoid an overwhelming number of charts, this chapter will be focus on showcasing the results of three selected samples: *UC1*, *C4* and *CN3*. These samples are chosen to highlight the main differences among the three different types of specimens. It is worth noting that only sample C4 and CN3 were subjected to rebar extraction and mass loss measurement, while the remaining samples are being kept under the corrosion process for continued monitoring beyond the scope of this thesis.

To ensure consistency in the results, additional information about the monitoring process for the remaining six samples will be included, along with the corresponding graphs in the Appendix. These samples were monitored for an additional 50 days, offering further data points for analysis into their behavior over an extended time period.

5.1.1 Corrosion potential

To gain an initial understanding of the corrosion level, the corrosion potential (E_{corr}) and half-cell potential charts can be examined.

It is important to note that different reference electrodes (RE) are used in corrosion potential measurements. Common examples include the Copper/Copper sulphate electrode (CSE), Silver/Silver chloride electrode (SSCE), Hydrogen electrode (SHE), and Saturated Calomel Electrode (SCE). Each reference electrode corresponds to specific predetermined potentials [57].

In the Galvanostatic Pulse technique, the reference electrode Ag/AgCl (SSCE) is commonly adopted. A corrosion potential value of *-406* mV, as indicated by the SSCE reference electrode, suggests a significant risk of severe corrosion.

Table 14: Corrosion potential - Risk levels, adapted from [58]

Corrosion risk [mV]	CSE	SSCE	SHE	SCE
Low	> -200	**>-106**	>+116	>-126
Intermediate	-350 to -200	**-106 to -256**	+116 to -34	-126 to -276
High	<-350	**<-256**	<-34	<-276
Severe	<-500	**<-406**	<-184	<-426

Among the three different samples, the expectation is that the corrosion potential values become more negative moving from the uncracked sample to cracked-notched. This is because in the main crack zone, where the transversal crack width increases, chloride ions can more easily penetrate the cement paste and come in contact with the rebar, leading to the higher likelihood of corrosion.

Specifically, in the UC1 sample, there are no cracks, and it is in pristine condition with an initial addition of chloride content of 0.4% by weight of cement. In contrast, the C4 sample represents a specimen that exhibited the largest transversal crack width of *0.2 mm* after undergoing the three-point bending test. Lastly, the CN3 sample is particularly interesting as it has a notch, but the main transversal crack formed on the sides of the notch. In this sample, a significant transversal crack of *0.7 mm* and a secondary crack within the main crack zone of *0.4 mm* have developed.

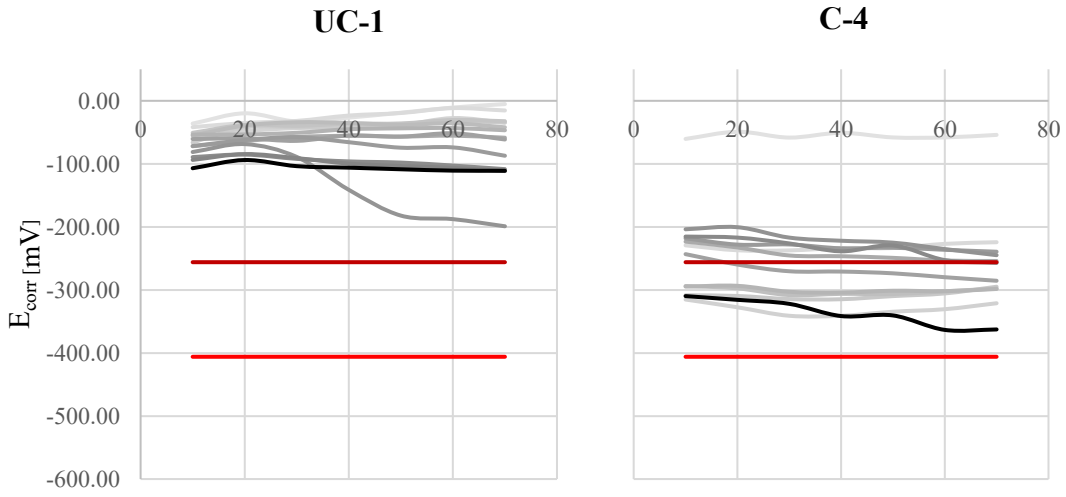

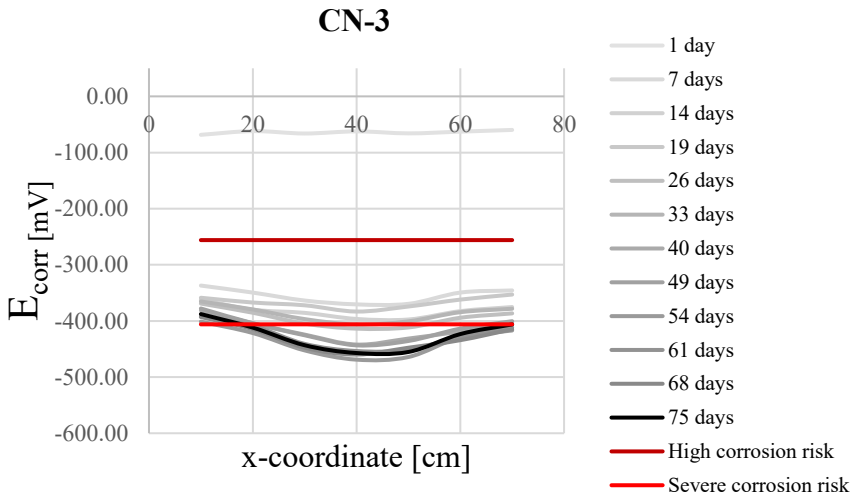

Figure 43: Corrosion potential over space for samples: UC1, C4 and CN3

From Figure 43, the corrosion potential is analysed longitudinally along the samples. The grey functions represent different periods measurements, progressing from the lightest to the darkest. The two red functions indicate corrosion risk, with dark red indicating high corrosion risk and light red indicating severe corrosion risk.

One notable observation is that, as predicted earlier, the corrosion potential significantly decreases from the uncracked specimen to the cracked-notched sample, particularly in the main crack zone. This demonstrates the significant influence of the transversal cracks on the corrosion potential.

The CN3 sample exhibits the lowest corrosion potential values. It is interesting to note that, even after the initial measurement taken before the corrosion process began, the values already decrease significantly, falling below the high corrosion risk limit of -256 mV. In the main crack zone, there is a distinct “sag” in the functions, with higher absolute values. However, in all the other the zones, the corrosion potential remains very low. This can be attributed to the presence of other transversal and longitudinal cracks throughout the sample, which facilitate chloride ingress, even with smaller crack widths, as shown in Figure 34. Over time, it becomes evident that the corrosion risk increases, with the darkest functions falling below the severe corrosion risk limit.

The C4 sample exhibit corrosion potential values between UC1 and CN3. After the first measurement, there is a smaller jump compared to CN3, but the functions remain above the high corrosion risk limit of -256 mV. However, the graph shows a non-monotonic decrease in corrosion potential, with values fluctuating over time. This behaviour is attributed to the non-depassivated state of the rebar in C4. Unlike CN3, depassivation did not occur for C4, which affect the accuracy of the Galvanostatic Pulse results, particularly when external factors such as humidity come into play. Therefore, the accuracy of measurements by Galvanostatic Pulse improves with higher corrosion levels. Another notable detail on C4 chart is the almost straight shape of the functions, indicating that the main crack zone is not the most affected (no sag). Zone 7 exhibits the highest absolute values, which can be attributed to the double exposure of the rebar surface, with the top and lateral surfaces contributing to chloride penetration.

The UC1 sample displays the lowest absolute values of corrosion potential, which is expected for a non-cracked specimen subjected to daily spraying of water containing chlorides over a period of approximately three months. With the exception of a potentially erroneous function, all the functions remain constant with values well below the high corrosion risk limit.

In conclusion, after a 75-day time-period, the results indicate that rebar CN3 is depassivated, with an almost instantaneous initiation stage. On the other hand, C4 is still not fully depassivated. However, since the chloride-induced corrosion involves pit corrosion, it is important to visually inspect the sample. Even if the rebar is not fully depassivated, the presence of localized pits would indicate that chlorides have come into contact with the rebar at specific locations.

In Appendix B.1, the same graphs (Figure 66) are provided for the other six specimens (UC2, C1, C2, C3, CN1 and CN2). These graphs confirm the distinct behavior of the three different types of samples, with a particular emphasis on the significant corrosion potential results observed for the cracked-notched samples. Figure 44 presents a comparison between the corrosion potential and half-cell potential over a period of time, aiming to provide a clearer visualization of the sample respective behaviours and changes over time.

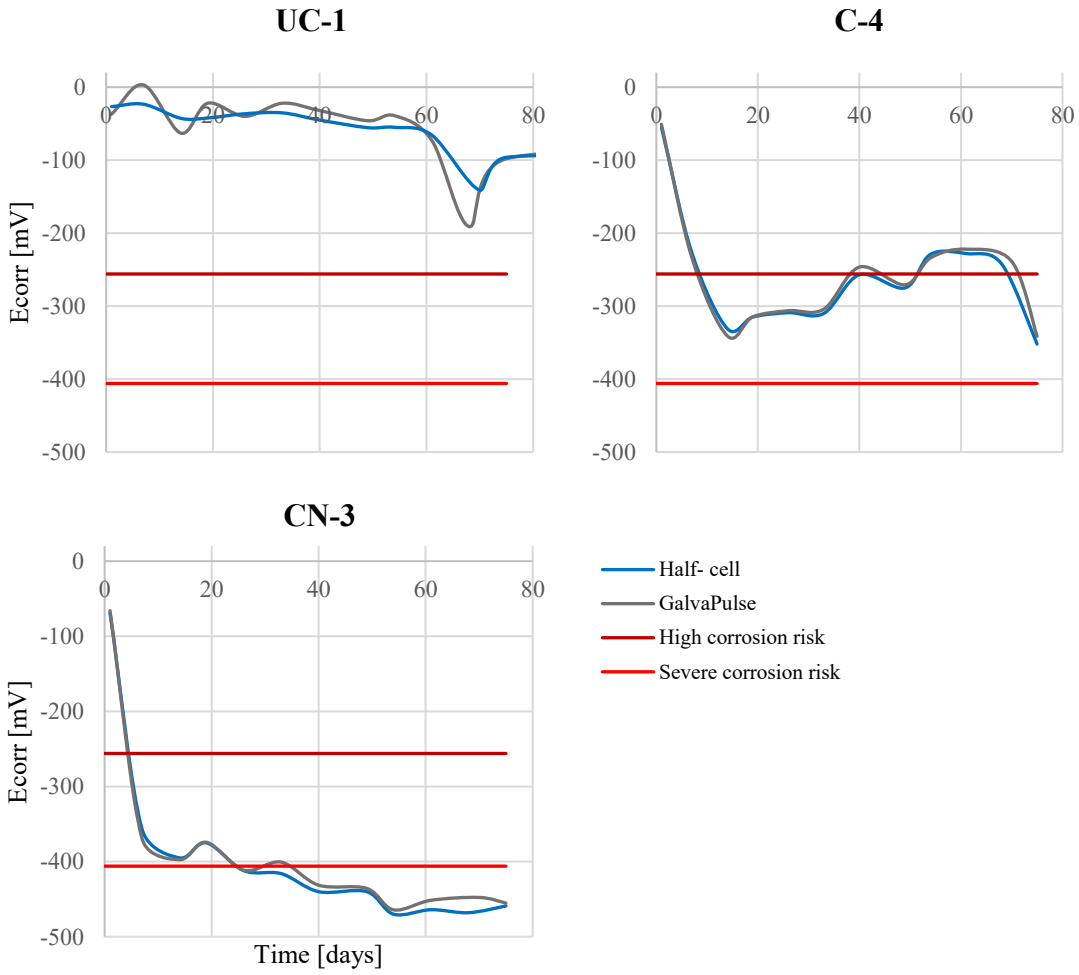

Figure 44: Corrosion potential over time for samples: UC1, C4 and CN3 at zone 4.

From Figure 44, it is evident that the corrosion potential values for sample C4 exhibit fluctuations over time. Initially, there is a drop in the corrosion potential due to the initiation of the corrosion process. Subsequently, the values stabilize around the high corrosion risk level until the last measurements, where a decline in the functions is noticeable. This decline suggests that during the final period of monitoring, the steel reinforcement may have been approaching depassivation. However, it is important to note that fluctuation of the functions throughout the entire monitoring process indicates that the rebar has consistently remained in the initiation phase.

In contrast, the chart for sample CN3 clearly demonstrates a monotonically decreasing trend of the corrosion potential over time. The absolute values of the corrosion potential exceed the severe corrosion risk limit from approximately 30 days onwards.

Finally, the chart for UC1 displays nearly constant functions with very low absolute values. The fluctuations observed in the last few days could be attributed to varying humidity conditions. Nevertheless, it is evident that the uncracked specimen is still entirely in the initiation phase.

The similarity between the two potentials confirms the consistency of the measurements.

5.1.2 Corrosion current density

The Galvanostatic Pulse instrument can assess the corrosion current density (I_{corr}) by evaluating the Polarization resistance (R_p) and utilizing the Stern-Geary relationship, as explained in Section 2.5. Additionally, Equation (2.19), provides further insight into this process. To specify a visual representation of the obtained results, Table 15 in the CONTECVET manual distinguishes different levels of corrosion risk based on the corrosion current density [52].

Table 15: Corrosion current density - Risk levels, adapted from [47]

i_{corr} [$\mu A/cm^2$]	Corrosion risk
≤ 0.1	Negligible
0.1 - 0.5	Low
0.5 - 1	Moderate
> 1	High

However, the corrosion current density is closely associated with the corrosion potential. The larger the potential difference, the greater the generated corrosion current. The corrosion current density provides a more comprehensive understanding of the corrosion state of the samples as it is linked to corrosion rate at the anode. A higher corrosion current density indicates a higher corrosion rate.

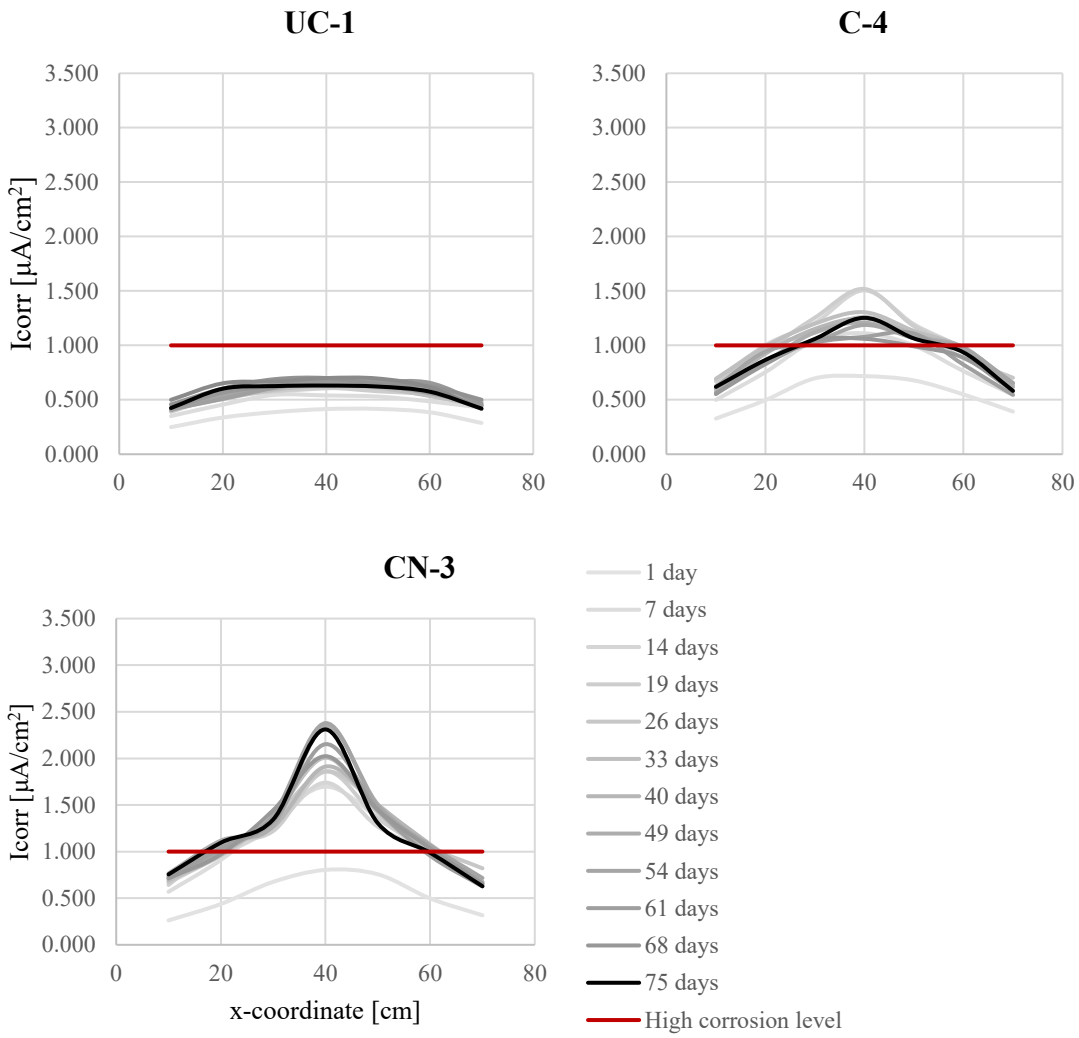

Figure 45: Corrosion current density over space for samples: UC1, C4 and CN3

Based on the results depicted in Figure 45, it is evident that the observed trend for the corrosion potential is confirmed. Notably, an intriguing observation is the tendency of the functions to exhibit a flatter shaped from CN3 to UC1. The influence of substantial transverse crack is clearly discernible in this figure, as the peaks of the corrosion current density increase with larger crack widths. However, it is noteworthy that all three specimens display the lowest values in the lateral zones, indicating a relatively safer region for corrosion propagation. This can be attributed to the reduction in transverse crack width moving away from the central zone coupled with the absence of cracks, since the frequency of transverse cracks tends to increase approaching the central zone of the samples in the three-point bending test.

In Appendix B.2, in Figure 67 presents the results for i_{corr} for the remaining samples, revealing the following findings:

- UC2 exhibits an i_{corr} value lower than the high corrosion risk level, although slightly larger than UC1. This suggest that UC1 appears to have the lowest corrosion rate in terms of corrosion current density among the samples.

- C1, C2 and C3 confirm the trend of C4 by displaying i_{corr} values larger than the high corrosion risk level in the middle of the specimens (zone 4). However, overall, C4 exhibits the highest values.
- UC1 and UC2 demonstrated nearly identical values of i_{corr}. Interestingly, since UC1 and UC2 were monitored for additional 50 days compared to UC3, the corrosion current density for these two samples continued to increase. This observation highlights how these types of specimens are highly influenced by the corrosion process over time.

5.1.3 Corrosion rate

The final corrosion parameter evaluated is the corrosion rate, which indicates the speed at which the corrosion propagates. It is directly related to the corrosion current density through the Faraday's law, see Equation (2.19). Figure 45 illustrates the variation of corrosion rate across the entire samples. However, for a more insightful analysis, it would be valuable to examine the corrosion rate (V_{corr}) [*mm/year*] over a specific duration of time [*days*]. Additionally, Table 16 presents different levels of corrosion risk based on the corrosion rate [52].

Table 16: Corrosion rate - Risk levels, adapted from [47]

V_{corr} [*mm/year*]	Corrosion risk
≤ 0.001	Negligible
0.001 - 0.005	Low
0.005 - 0.01	Moderate
> 0.01	High

Furthermore, Figure 46 displays the corrosion rates for all three specimens in four distinct zones (from zone 1 to zone 4). The remaining zones (5, 6 and 7) exhibit a very similar behaviour of zones 3, 2 and 1, respectively, due to the symmetry of the samples.

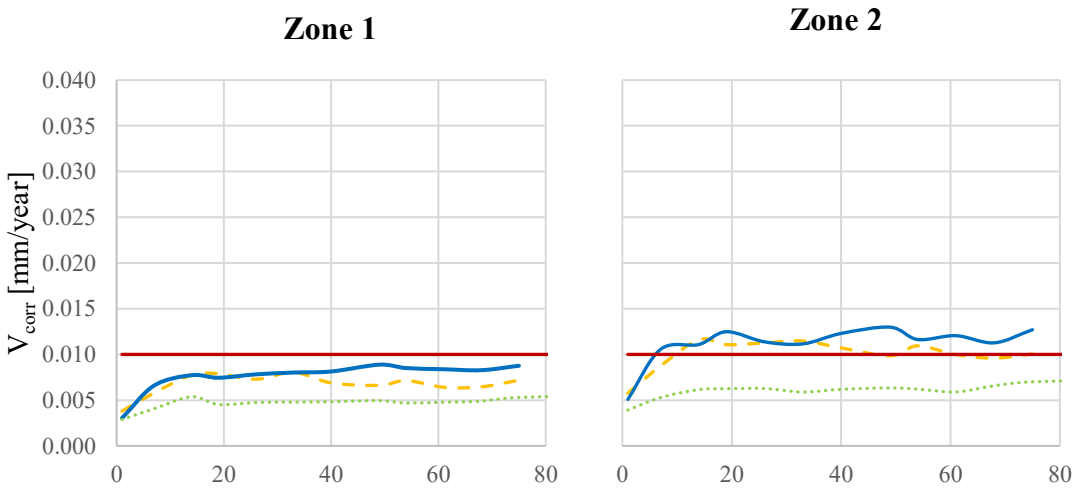

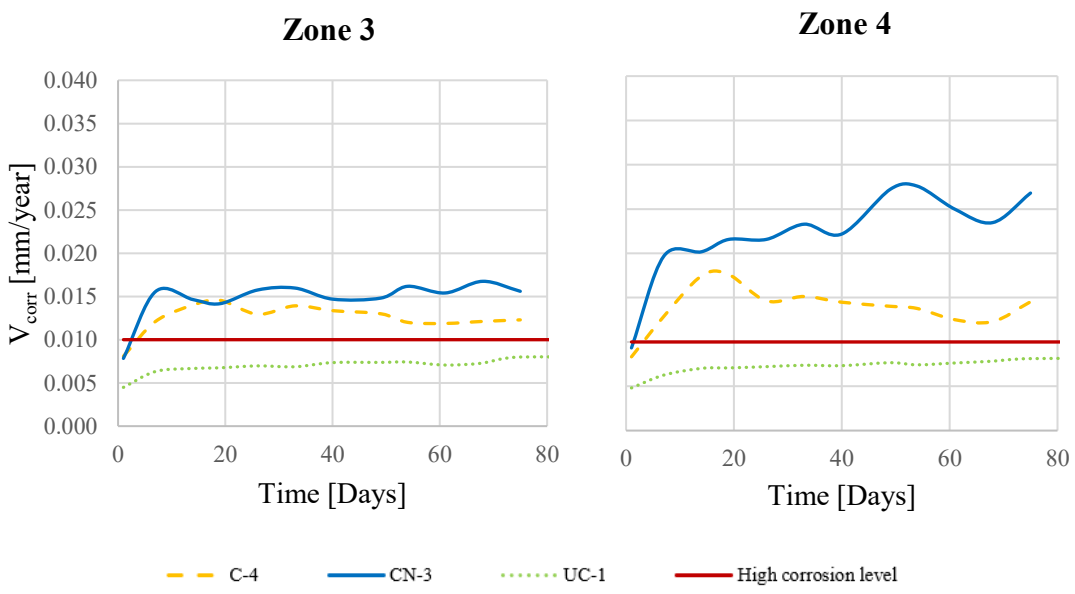

Figure 46: Corrosion rate over time for samples: UC1, C4 and CN3

From Figure 46, the most noteworthy observation is that, in general, the corrosion rate increases moving from zone 1 (farthest) to zone 4 (central) for all three specimens. This increase is particularly pronounced for samples whit larger transverse cracks, such as CN3.

UC1, on the other hand, exhibits a relatively consistent behaviour from zone 1 to zone 4, with corrosion rates remaining below the high corrosion risk level throughout.

Sample C4 shows a similar pattern to UC1 in zone 1, but as it approaches the center, the corrosion rate begins to increase. Starting from zone 2, the values surpass the high corrosion risk threshold and reach their maximum in zone 4.

However, the most significant behaviour is observed in the case of sample CN3. It shows a similar trend to UC1 and C4 in zone 1, but in zone 4, the corrosion rate significantly surpasses that of C4, with CN3 exhibiting much larger values. This highlights the importance of crack width in the main crack zone, as the corrosion rate in CN3 is double that of C4 in zone 4.

In Appendix B.3, more complete graphs are presented in Figure 68, showcasing the corrosion rate over time for all the specimens in each zone, ranging from 1 to 7. The figure demonstrates a clear trend that moving away from zone 4 and towards either zone 1 or 7, the corrosion rate significantly decrease. Furthermore, the graphs highlight the distinct behavior of the cracked-notched specimens (CN1 and CN2) compared to the other samples. In zone 4, the cracked-notched specimens display a much higher increase of corrosion rate compared to the other specimens. On the other hand, the uncracked specimens show minimal increase in the corrosion rate both in time and space along the specimen.

The electrochemical corrosion parameters result clearly demonstrates the significance of the crack width in the main crack zone for the corrosion process. However, as a final step, it is crucial to visually confirm these findings by extracting the rebar from the samples.

The experimental results presented in this section can be compared with the theoretical predictions obtained from the Otieno model [35], as described in Section 4.4. However, it should be noted that only *field* data from Otieno model were used, in this comparison, as the results for accelerated corrosion did not align with the corrosion setup employed in this thesis' experimental work. The comparison is presented in Table 17.

Table 17: Comparison of Theoretical and measured corrosion rates

Specimen	Crack width [mm]	Theoretical V_{corr} [mm/year]	Measured V_{corr} [mm/year]
C4	0.21	0.003	0.015
CN3	0.73	0.004	0.027

It is evident that there is a significant difference between the theoretical and measured results, particularly with a discrepancy of 84.05%. Several factors contribute to this variation, which distinguishes the experimental work in this thesis from that conducted by Otieno [35]:

Initial chloride content:

In this thesis work, the initial chloride content corresponds to 0.4%, whereas no salts were used during the casting process in Otieno's experiment. This discrepancy leads to a shorter corrosion initiation phase and a faster corrosion propagation in the current experimental setup.

Apparent diffusion coefficient:

The values of D_{app} differed between the two experimental works, with a larger value in this thesis work. A larger D_{app} implies faster chloride penetration and, consequently, a more intensive corrosion process. This difference may be attributed to the varying exposure time of the samples, with 122 weeks for Otieno's experiment and 11 weeks for this thesis' experimental work. Additionally, differences in w/c ratio and concrete mixture, could also influence D_{app} values. It is worth mentioning that D_{app} was evaluated using the Rapid Migration test for this thesis work, while Otieno's research relied on the chloride conductivity index (CCI).

Exposure environment:

In this thesis' experimental work, the samples were placed in a closed structure and subjected to daily wetting and drying by water containing salt. In contrast, Otieno's experiment involved specimens exposed to the tidal zone in a marine environment. The varying salinity of water and timing of wetting and drying could be significant factors contributing to the differences observed between the two experimental works.

Therefore, selecting an appropriate predictive model for the evaluation of corrosion rate is not straightforward. Factors such as exposure environment, concrete mixture, water-to-cement ratio and exposure time can lead to significant variations in results.

5.2 Crack width monitoring

Throughout the entire experimental program of this thesis, it has been essential to monitor all the specimens due to one of the most significant consequences associated with the formation of corrosion products (rust): the increase in volume at the rebar surface and the resulting stress and cracking of the adjacent concrete. To achieve this, various methods were employed to monitor crack variation and formation. The primary objectives of crack monitoring were as follows:

- To determine whether the transverse cracks tend to close after the three-point bending test and subsequently widen due to the potential formation of corrosion product.
- To visually observe the formation of new longitudinal cracks resulting from the corrosion process.

The tools utilized for crack monitoring include DEMEC points, a crack ruler and a microscope, as illustrated in Figure 47. DEMEC points are also able to measure strains, even before the cracks are visible. These instruments were chosen to accurately assess and record any changes in crack behaviour and development.

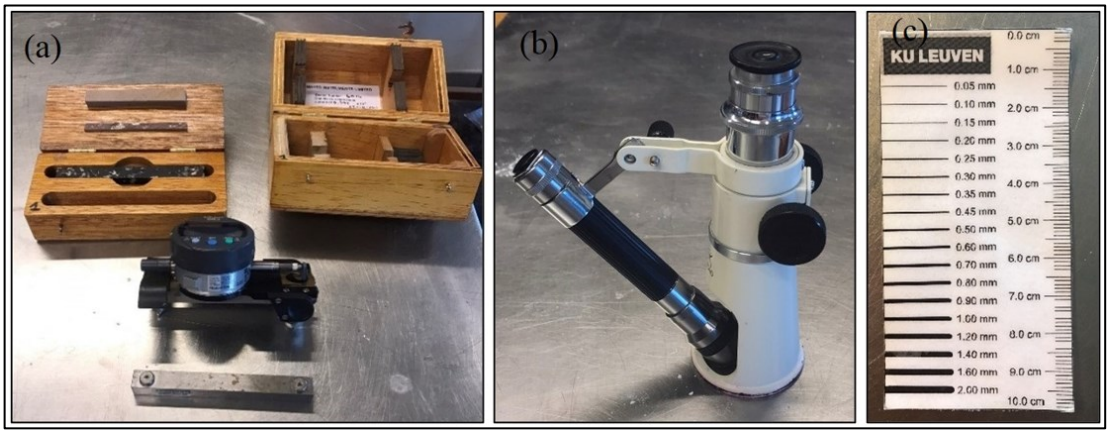

Figure 47: Crack width monitoring tools: (a) DEMEC dial gauge and invar bar, (b) Microscope, (c) Crack ruler

The DEMEC system, as described in Section 3.3, is capable of measuring changes in distances between two fixed points over time and allows for observation of the configuration of those points. In the case of this experimental program, two rows of DEMEC points were distributed longitudinally along the specimens: *HTi* (Horizontal-Top) and *HBi* (Horizontal-Bottom), where *i* ranges from 1 to 7. These rows enable monitoring of the longitudinal behavior of the specimens.

Additionally, there are nine columns of DEMEC points distributed transversally across the specimens, labeled as *Vi* (Vertical). These points are of particular interest when it comes to monitoring the hypothetical formation of longitudinal cracks parallel to the embedded reinforcement caused by corrosion products.

Furthermore, six points, labeled as *HLi* (Horizontal-Lateral), were placed on the lateral side of the specimens. These points were specifically positioned to monitor the variation of the main transverse crack after three-point bending test.

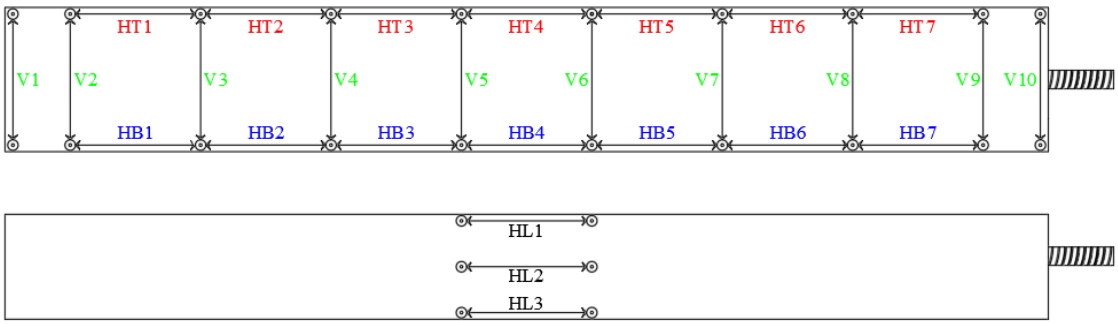

Figure 48: DEMEC points configuration - Top view (above), Lateral view (bottom)

It is important to note that the measurements acquired through the DEMEC points are associated with the crack width corresponding to the line between two DEMEC points. As such, it does not directly measure the opening at the center over the rebar. Specifically, for the main transverse cracks, the opening is related to the lines *HT4* and *HB4*.

As for the microscope, specific points were chosen in advance to monitor the variation of crack width. These points were highlighted with blue dots, as shown in Figure 49. Notably, these points are all located above the rebar, which is the most significant point of the crack. These locations represent critical points where chloride penetration and access to the reinforcement are most likely to occur.

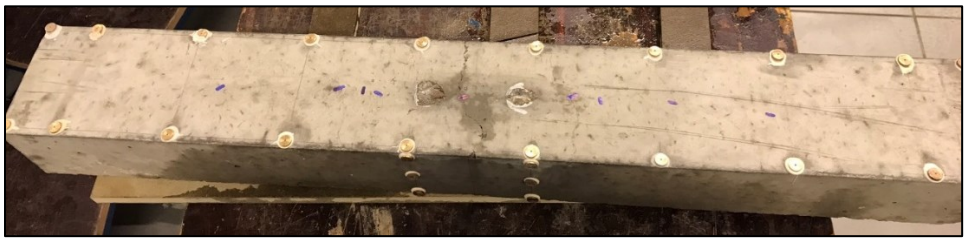

Figure 49: Microscope monitoring points

The crack ruler, being the easiest and quickest instrument to use, was utilized to monitor all cracks in the specimens. Specifically, the transverse cracks were measured at four different points, and subsequent analysis involved calculating the mean value and standard deviation of these measurements.

Table 18 provides the resolutions of each instrument [59] [60].

Table 18: Instruments resolutions

Instrument	**Resolution [mm]**
Demec points	0.001
Microscope	0.020
Crack ruler	0.050

In the thesis report, measurements recorded from the crack monitoring items are included to facilitate a comparison between them and track the development of the cracks. Figure 50 depicts the lines *HL1* and *HL2*, which serve as reference for monitoring crack development. These lines are used in conjunction with a microscope and crack ruler to obtain consistent data for comparison. It is worth noting that the crack widths measured along *HL1* and *HL2* are of particular interest as they

represent the lateral variation of the main transverse crack following three-point bending test.

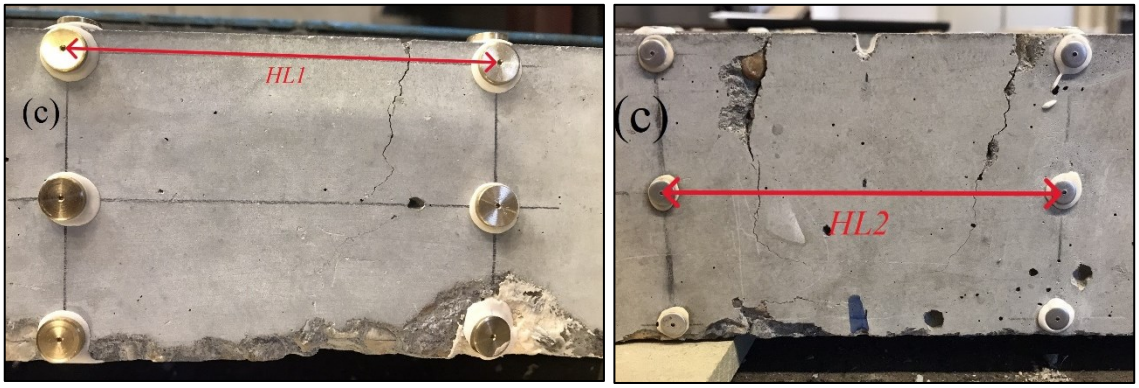

Figure 50: Crack monitoring comparison lines - HL1 and HL2

Although the comparison was performed for all cracked specimens, only the results for samples C4 and CN3 are considered in this report, as the results from the other samples were considered not particularly significant or relevant to the study.

Indeed, for the C4 sample, the crack monitoring was conducted along the line *HL1*, whereas for the CN3 sample, it was performed along the line *HL2.* The reason for this difference is the presence of a notch specifically located in correspondence with the line *HL1* for the CN3.

Furthermore, it is important to note that, unlike the electrochemical parameter figures, the time-domain in the crack monitoring section is larger. This because the first measurements by the DEMEC system were taken both before the 3PBT to establish reference measurements and after the test to monitor the width of the cracks. As a result, the crack monitoring process began 41 days earlier than the monitoring process for the electrochemical parameters.

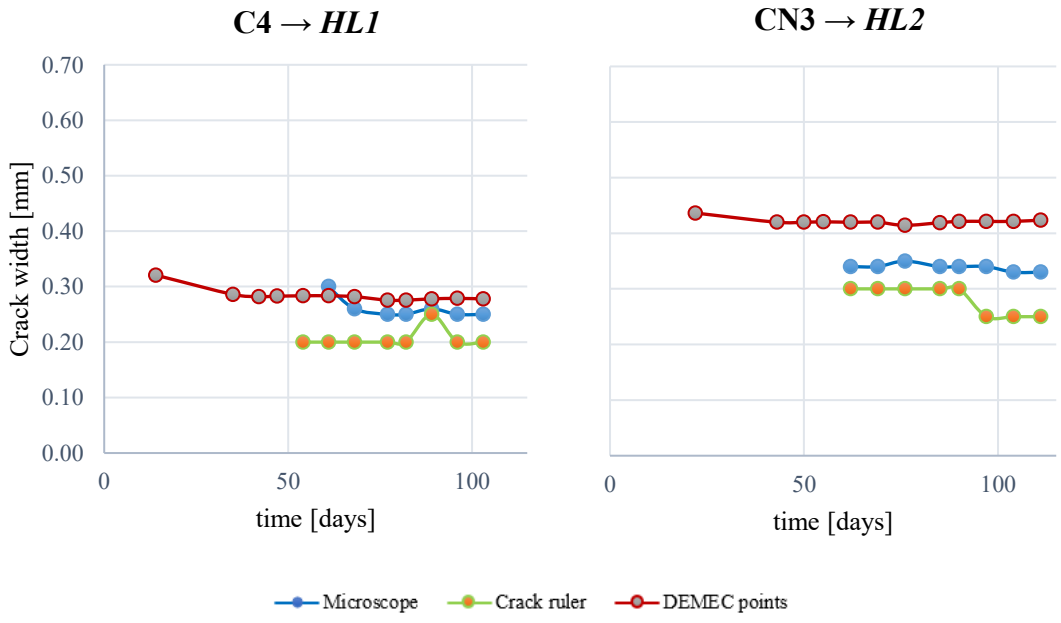

Figure 51: Crack width monitoring for samples C4 and CN3

From Figure 51, it can be observed that the main transverse crack width for both C4 and CN3 samples, as measured along the reading lines (*HL1* and *HL2*), does not change significantly over time. In the initial period, a small decrease in crack width can be noticed based on the DEMEC measurements, which may be attributed to crack closure and relaxation after the three-point bending test. However, after this initial decrease, the crack width remains relatively constant.

In terms of the *HL2* line (corresponding to CN3), a larger crack width is observed compared to *HL1* (corresponding to C4). This difference in crack width also contributes to larger variations among the monitoring items. Specifically, for CN3, the distance between the DEMEC measurements, microscope, and crack ruler is greater compared to C4. This can be explained by the fact that, with the microscope and crack ruler, the measured values correspond to the sum of two cracks, formed in the main crack zone. In contrast, the DEMEC system takes into account the presence of other possible microcracks as well.

It is noticeable that the time-domain of the two samples, CN3 and C4, differs, with CN3 having a larger time-period. This discrepancy is because sample CN3 underwent the 3PBT eight days before sample C4. As a result, the DEMEC measurements for CN3 were taken eight days earlier than those of C4.

It is important to note, however, that the resolution of the microscope and crack ruler is closely tied to the operator's skill and technique, whereas the DEMEC system provides digital and automatic measurements, reducing the operator-related responsibilities.

Based on the information provided, it appears that the monitoring of the transverse crack did not yield significant results in terms of the development of the crack width. This may be attributed to the relatively short timeframe available for the experimental work conducted in this thesis. It is important to note that the formation of corrosion products (rust) and its effects on crack width may require a longer duration to observe substantial changes. However, as indicated by the monitoring of electrochemical parameters, the sample CN3 exhibits signs of corrosion propagation.

Regarding the last set of measurements, interesting results were observed for the longitudinal crack widths of the CN1 and CN2 samples, as depicted in Figure 52.

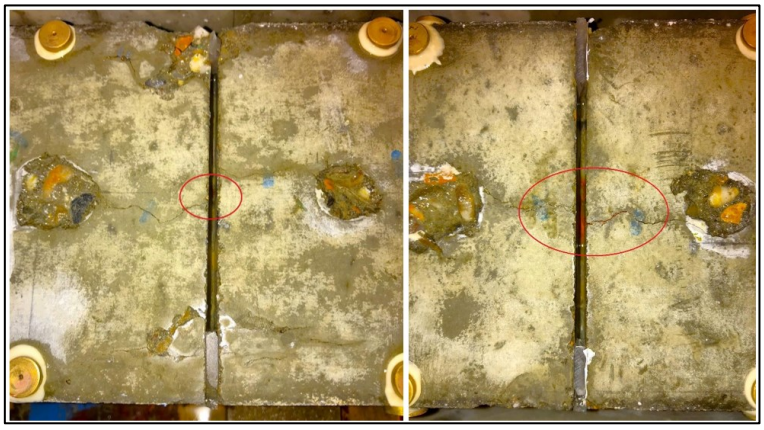

Figure 52: Corrosion products samples CN1 (left), CN2 (right)

The presence of reddish color, indicating the formation of rust, was observed from the notch in the specimens. Of particular interest is the reddish color inside the longitudinal crack to right of the notch in the CN2 sample. This crack holds significant importance for studying the development of crack width, as the corrosion product within the crack may contribute to its enlargement and the formation of other interconnected microcracks. The observation of this reddish color provides valuable insights into the ongoing corrosion processes and their potential impact on crack behavior.

Furthermore, Figure 53 displays the time history of the longitudinal cracks in the CN1 and CN2 samples.

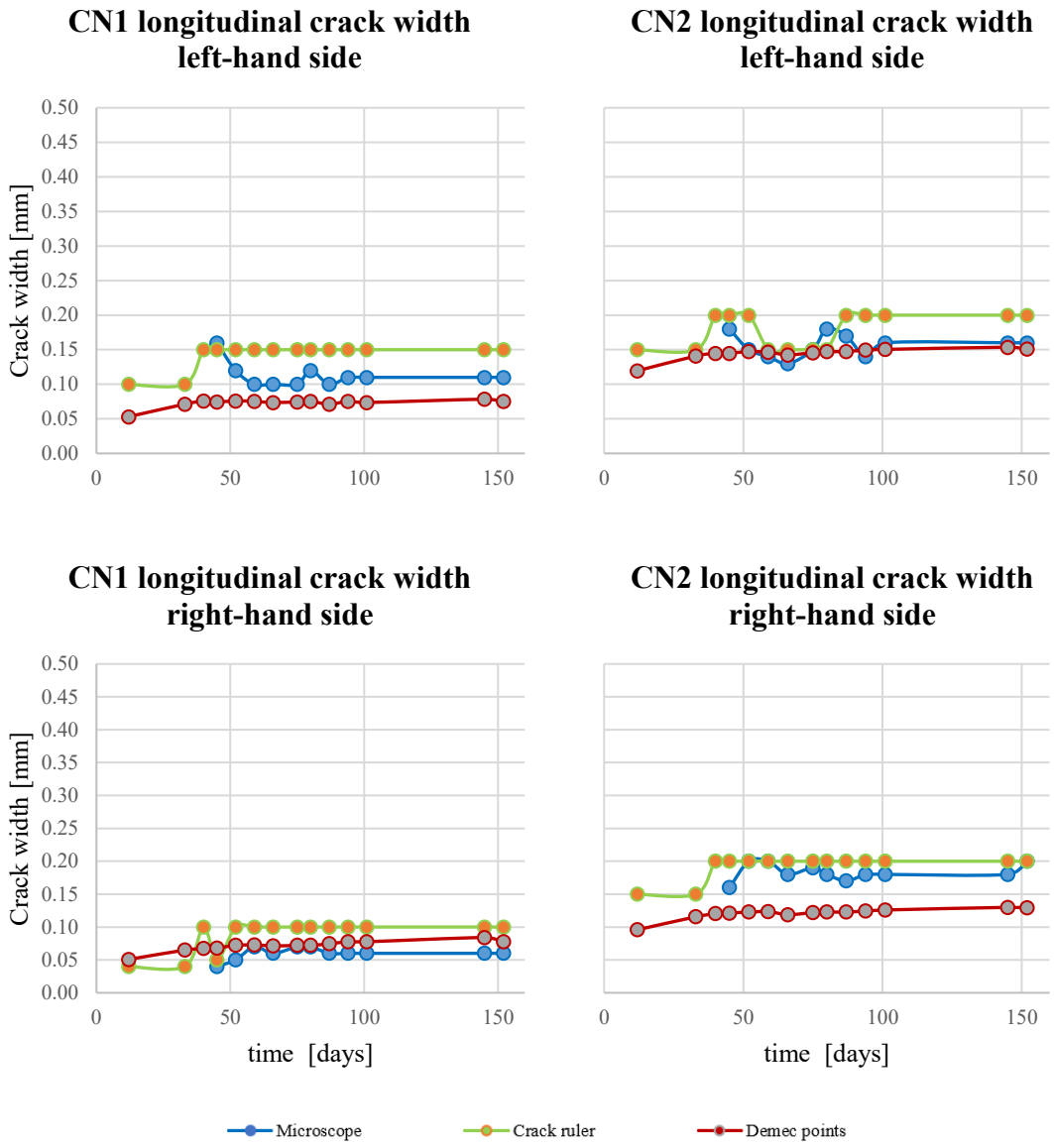

Figure 53: Longitudinal crack monitoring samples CN1 and CN2

The significant detail revealed by the figure is that in the final period, all the longitudinal cracks, particularly as indicated by the DEMEC system results, experienced a slight increase in width. This observation suggests that the longitudinal cracks in the main zone were influences by the corrosion process.

In summary, the monitoring of crack widths did not yield significant results for the consequences of the corrosion process on the main transverse cracks. These cracks exhibited a slight decrease in width after the three-point bending test but were not significantly affected by the corrosion process thereafter. However, notable results were observed for the longitudinal cracks in samples CN1 and CN2. These results can be attributed to three factors:

- The electrochemical parameters indicated a significant corrosion level in the main zone, as shown in Appendix A1.
- The notch in these two specimens was deeper compared to CN3, making the corrosion products more visible and reducing the concrete cover at the notch, thereby accelerating chloride ingress at that specific point.
- The increase in crack width, whether in transverse or predominantly longitudinal cracks, requires more corrosion time.

5.3 Steel reinforcement mass loss

The evaluation on the consequences of the corrosion process on the steel reinforcement represents the final step in the analysis of chloride-induced corrosion. As outlined in Section 2.6, the gravimetric weight loss measurement of the rebars involves extracting the rebar from the concrete sample, cutting it into pieces of the same length and chemically cleaning the pieces to remove any corrosion products. After the cleaning process, the weight of the rebar is measured and compared to its initial weight. The difference in weight before and after the corrosion process provides an indication of the effect of the chloride-induced corrosion on the rebar. Additionally, the gravimetric weight loss can be compared to the predictions obtained through electrochemical techniques, thereby serving as a validation of these techniques.

For this research program, the specimens chosen for rebar extraction and analysis are C4 and CN3, which have been the focus of the monitoring and assessment chapter thus far. Cores were taken from the concrete samples for further analysis of chloride content and carbonation, as described in Section 5.4 of the thesis.

Figure 54: Samples C4 and CN3 rebar extraction

After extraction, the rebars were cut into pieces of the same length, measuring 200 mm, following the specific layout illustrated in Figure 55.

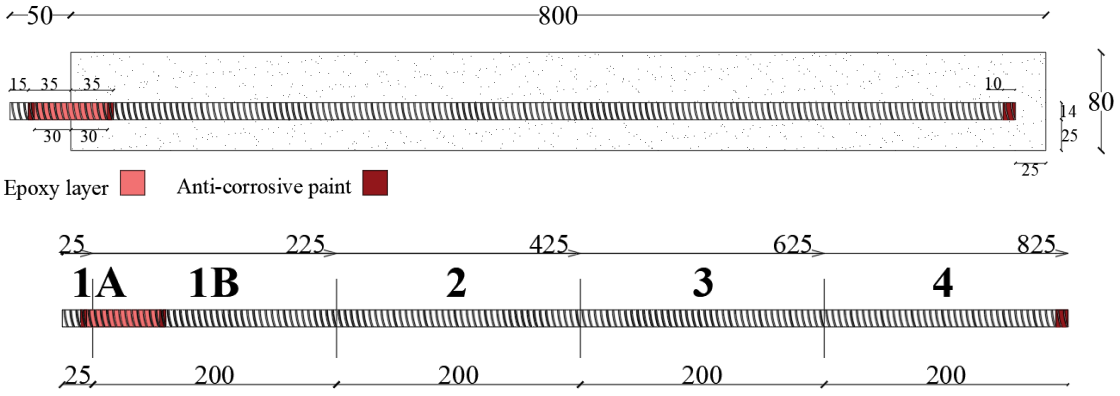

Figure 55: Rebar cut layout

The primary reason of this division was to assess the corrosion level of the rebar across different spatial zones. Keeping the rebar as one piece would provide only an average result, whereas dividing the sample into zones with varying corrosion levels enabled the observation of areas with higher or lower mass loss due to corrosion. Additionally, these cuts are utmost importance for this thesis work, as they facilitate a comparison of the weight with an uncorroded reference piece of rebar (reference weight), the cuts made on the two rebars are shown in Figure 56.

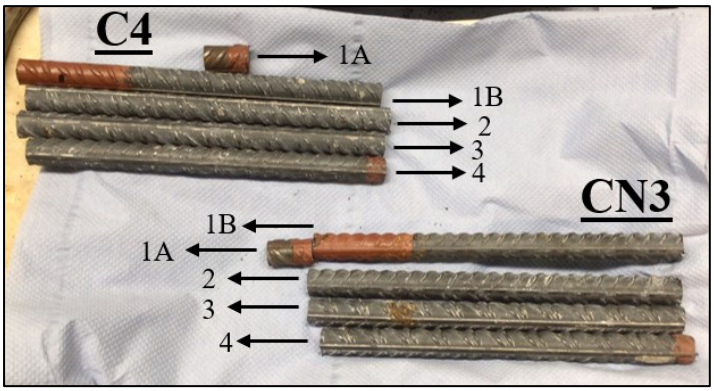

Figure 56: Samples C4 and CN3 rebar cut

The cantilever part of the rebar was selected as the initial point for cutting. The total length of the rebar, which was 825 mm, was divided into five pieces. One of these, measuring 25 mm, is of relatively low importance as it represents the cantilever part of the rebar that was not covered by the concrete paste.

Following the cutting process, chemical cleaning was conducted on the rebars. Figure 57 and Figure 58 illustrate the differences between the rebars before and after cleaning. Notably, the figures highlight the presence of pits on both the C4 and CN3 rebars. This observation is a significant detail that indicates the occurrence of corrosion and its impact on the rebar surfaces.

Figure 57: C4 rebar pit. Pre-cleaning (top), post-cleaning (bottom)

Figure 58: CN3 rebar pits. Pre-cleaning (top), post-cleaning (bottom)

For the rebar of sample C4, the corresponding cut-piece is *cut-piece 2*, which spans from 225 mm to 425 mm, as indicated by the coordinates below the cut-piece in Figure 55. The pit observed on this rebar is located at approximately 400 mm from the beginning of the rebar, indicating its association with the main crack zone. No other pits were observed along the entire length of the rebar.

In the case of the rebar from sample CN3, the corresponding cut-piece is *cut-piece 3*, spanning from 425 mm to 625 mm. In the pre-cleaning picture, a reddish spot covering the surface of the rebar can be observed. After cleaning, the presence of two pits becomes evident, located very close to each other. These pits are situated approximately 480 mm from the beginning of rebar, aligning with the main crack width in the main crack zone, particularly near the largest crack with a width of approximately 0.7 mm. This result is interesting as it confirms the findings from the electrochemical measurements.

Although the dimensions of these pits are relatively small, their presence provides evidence of the corrosion state that has been monitored thus far. It is important to note that these pits may not have a significant influence on the mass loss and diameter reduction of the rebar. However, they serve as indicators of the corrosion process.

Specifically, the mass loss for *cut-piece 2* of sample C4 and *cut-piece 3* of sample CN3 is evaluated by comparing them with a reference cut-piece. The initial value of the analyzed cut-pieces is calculated using the Equation (5.1):

$$\begin{aligned} W_{C4,2,0} &= q_{ref} \cdot L_{C4,2} \\ W_{CN3,3,0} &= q_{ref} \cdot L_{CN3,3} \end{aligned} \tag{5.1}$$

Where $W_{C4,2,0}$ and $W_{CN3,3,0}$ represent the initial weight of *cut-piece 2* for C4 and *cut-piece 3* for CN3, respectively, expressed in grams [g]. q_{ref} is the distributed weight of the reference cut-piece, expressed in grams over millimetres [g/mm], finally, $L_{C4,2}$ and $L_{CN3,3}$ represent the length of the *cut-piece 2* for C4 and *cut-piece 3* for CN3, respectively, measured in millimetres [mm].

Subsequently, the final weight measured after the corrosion process, in the lab, is compared to the initial weight obtained by Equation (5.1), yielding the following results:

$$\begin{aligned} \Delta W_{C4,2} &= W_{C4,2,f} - W_{C4,2,0} = -0.17\ \% \\ \Delta W_{CN3,3} &= W_{CN3,3,f} - W_{CN3,3,0} = -0.53\ \% \end{aligned} \tag{5.2}$$

Where $\Delta W_{C4,2}$ and $\Delta W_{CN3,3}$ represent the variation in weight of *cut-piece 2* for C4 and *cut-piece 3* for CN3, respectively, expressed as a percentage [%]. $W_{C4,2,f}$ and $W_{CN3,3,f}$ are the final weights for *cut-piece 2* of C4 and *cut-piece 3* of CN3, respectively, expressed in grams [g].

The main conclusion drawn from these results is that CN3 displayed visually larger pits, which is further confirmed by a larger reduction in percentage of mass loss compared to C4. This finding aligns with the analysis conducted in the previous section 5.1, where the GalvaPulse monitoring also indicated a higher corrosion level for CN3.

To further analyse the corrosion level, the evaluation of mass loss based on the electrochemical parameter results can be conducted. Following the procedure

outlined in Section 2.5 of the literature, representative corrosion current density or corrosion rate values are required to simulate the behaviour over time. By using the formula for the mean value (Equation (2.25)) the representative corrosion rate can be calculated for each zone (1 to 7) of the specimens, specifically for samples C4 and CN3.

After obtaining the representative values for each zone, the penetration attack (P_x) is evaluated using Equation (2.26). Considering that chloride-induced corrosion involves the formation of pits, a pitting factor (α) equal to 10 (for conservative reasons) is used to determine the pit depth (P_{pit}).

Table 19 lists the pit depths for each zone of the rebar in sample C4 and CN3.

Table 19: Pits depth prediction for rebar C4 and CN3

P_{pit}	C-4	CN-3
	[mm]	[mm]
Zone 1	0.014	0.016
Zone 2	0.021	0.023
Zone 3	0.026	0.030
Zone 4	0.029	0.046
Zone 5	0.025	0.032
Zone 6	0.021	0.023
Zone 7	0.014	0.015

Based on the provided results, it is observed that the maximum pit depths for both samples occur in zone 4, with CN3 exhibiting the largest depth. However, it is important to note that these depths are relatively small, and their impact on the initial rebar diameter can be negligible. For example, the maximum pit depth for CN3 corresponds to a diameter loss of *0.3%* from the initial value of 14 mm, which is considered insignificant. Therefore, GalvaPulse analysis prediction aligns with the conclusion that the experimental timeframe was too short to observe significant corrosion product formation, rebar diameter reduction, and mass loss.

As final step, the weight loss can be compared by approximating the weights of cut-piece *2* for samples C4 and *cut-piece 3* for samples CN3, respectively. Using Equation (2.29), the predicted final weights of the cut-pieces can be determined, while the initial weight is again obtained by Equation (5.1) (see Table 19).

Subsequently, considering the pit depths in in zone 4 for both the cut-pieces *2* and *3*, the previously reported Equation (5.2) is utilized to evaluate the predicted mass loss for these cut-pieces, and then the results are compared with the measured and predicted results.

$$\begin{aligned} \Delta W_{p,C4,2} &= W_{p,C4,2,f} - W_{p,C4,2,0} = -0.33\ \% \\ \Delta W_{p,CN3,3} &= W_{p,CN3,3,f} - W_{p,CN3,3,0} = -0.76\ \% \end{aligned} \tag{5.3}$$

It is evident that the predicted weights are slightly larger than the measured weights. However, the mass loss percentage are relatively similar, indicating a reasonable agreement between the measured and predicted results. The slightly larger values in the predicted mass loss can be attributed to the selection of a pitting factor of 10, which represents a conservative assumption. In reality, the actual corrosion process

observed in this experimental work is minimal, resulting in very small values for mass loss. It is important to note that these comparisons may not hold true for long-term corrosion processes, as different factors come into play over extended periods. Conducting an analysis on the long-term corrosion would be beneficial for further validation and understanding of these results obtained in this study.

5.4 Chloride content measurement

The chloride content in the concrete samples was measured as a part of the further analysis in this thesis work, aiming to gain valuable insights into the impact of chlorides on the corrosion process.

To assess the chloride content, cores were extracted from the concrete samples, as depicted in Figure 59. In the case of sample C4, cores were extracted from two distinct points: one from the non-cracked surface in zone 7, and another from the surface containing the main transversal crack measuring 0.22 mm.

Similarly, for sample CN3, both cores were taken from the main crack zone, with one containing the main transversal crack measuring 0.70 mm, and the other including the notch without cracks, while other cores are used for experiments beyond the scope of this thesis.

After extracting the cores, they were subdivided in different pieces (A to E), as outlined in Table 20 and Figure 59, to allow for a depth-by-depth analysis of the chloride content, providing valuable information on chloride penetration.

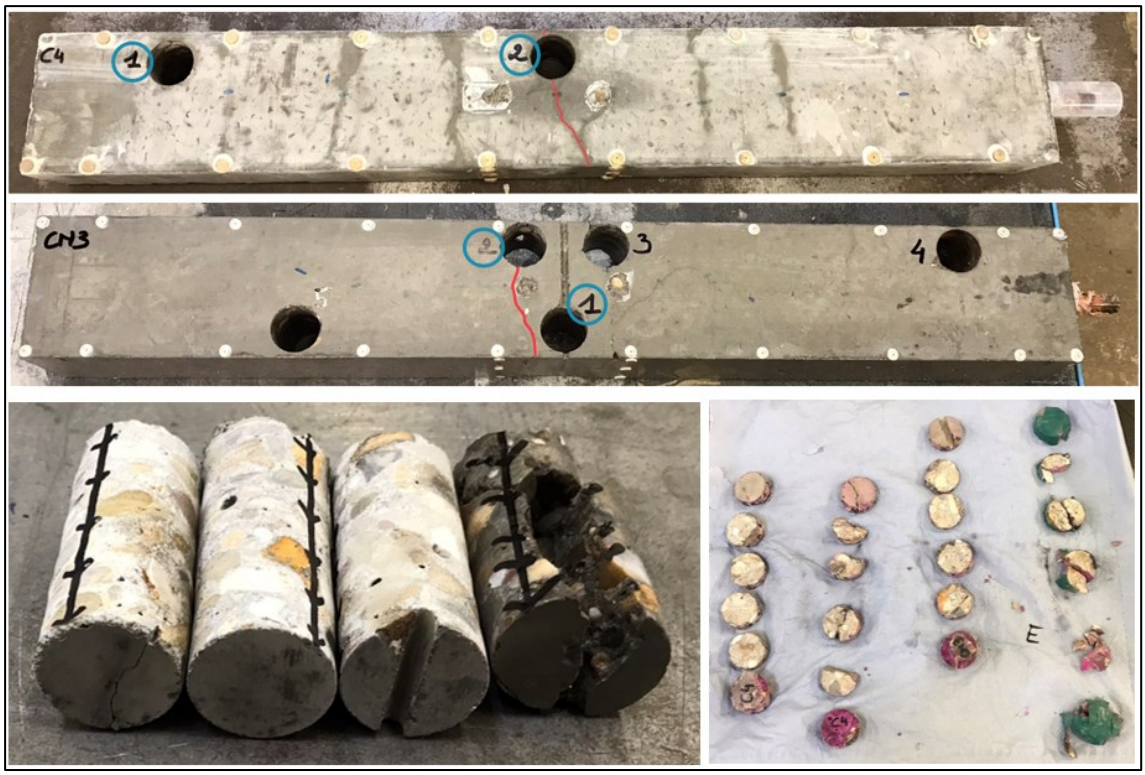

Figure 59: C4 and CN3 cores extraction

Pieces D were not evaluated due to timing constraints, but pieces A, B and C were of particular interest as they represented the depth from the external surface to the rebar with a concrete cover of 25 mm. However, the pieces E were analysed as the chlorides present at that depth could be referred more on the initial chloride content, unlike the chlorides sprayed with water.

Table 20: Cores subdivision

Label	Depth [mm]	
	from	to
A	0	10
B	10	20
C	20	30
D	30	50
E	50	60

Subsequently, the extracted cores were subjected to *tritation*, a chemical procedure used to assess the chloride content inside the cores, as illustrated in Figure 60. Each piece underwent tritation to evaluate the chloride content at various depths within the concrete samples.

Figure 60: Tritation process

After analysing all the pieces, the chloride content was calculated and results are presented in Table 21 and Table 22, showing the chloride content over concrete and cement weight, as well as the chloride mass for each label and different depths.

Table 21: C4 – Chloride content in sample C4 cores 1 and 2

C4 - Core 1 - zone 1 (far from the main crack zone)

Label	Depth [mm]		% by weight of concrete	% by weight of cement
A	0	10	0.27	1.89
B	10	20	0.07	0.46
C	20	30	0.06	0.39
E	50	60	0.04	0.29
Average			0.11	0.76

C4 - Core 2 - zone 4 (main crack zone)

Label	Depth [mm]		% by weight of concrete	% by weight of cement
A	0	10	0.25	1.72
B	10	20	0.17	1.20
C	20	30	0.10	0.70
E	50	60	0.09	0.62
Average			0.15	1.06

For sample C4, at the surface, the chloride content is slightly higher for core 1, whereas moving deeper into the concrete matrix, the chloride content significantly increases for core 2. This indicates that the presence of the crack facilitates the ingress of chlorides to greater depths. On average, the chloride content is indeed higher for core 2 compared to core 1.

Table 22: Chloride content in sample CN3 cores 1 and 2

CN3 - Core 1 - zone 4 (notch)

Label	Depth [mm]		% by weight of concrete	% by weight of cement
A	0	10	0.28	1.90
B	10	20	0.08	0.58
C	20	30	0.04	0.30
E	50	60	0.02	0.17
Average			0.11	0.74

CN3 - Core 2 - zone 4 (main crack)

Label	Depth [mm]		% by weight of concrete	% by weight of cement
A	0	10	0.37	2.51
B	10	20	0.20	1.35
C	20	30	0.19	1.28
E	50	60	0.17	1.17
Average			0.23	1.58

For sample CN3, the chloride content is significantly higher for core 2 at each depth, which highlights the larger width compared to sample C4. Another interesting point is that, despite the reduced concrete cover due to the notch (6 mm reduction), the chloride content in the notch area is very similar to that of C4 at the non-cracked part of sample C4, indicating that the notch does not significantly influence the chloride penetration. Core 2 of CN3 exhibits the highest chloride content values, confirming that a larger crack width leads to higher chloride ingress into the concrete.

The chloride content at the concrete cover depth, 25 mm, is of crucial importance in assessing the corrosion risk for the RC structures. By referring to Table 21 and Table 22, the chloride content at this specific can be determined for each sample.

Once the chloride content values are known, they can be compared to the corrosion risk levels provided by Table 23. These risk levels are indicative of the potential severity of chloride-induced corrosion in the concrete.

Table 23: Chloride content - Risk levels; adapted from [56]

Total chloride content [by weight of cement]	Total chloride content [by weight of concrete]	Corrosion risk
≤ 0.2 %	≤ 0.03 %	Negligible
0.2 - 0.4 %	0.03 - 0.06 %	Low
0.4 - 1 %	0.06 - 0.14 %	Moderate
> 1 %	> 0.14 %	High

The chloride content analysis for both sample C4 and CN3 provides useful insights into corrosion risk levels at different depths within the concrete. For sample C4, the core located far from the main crack zone exhibits a relatively low chloride content of approximately 0.39% by weight of cement, indicating a low corrosion risk. However, the core within the main crack zone shows a higher chloride content of approximately 0.70%, resulting in a moderate corrosion risk.

Similarly, for sample CN3, the core at the notch area displays a chloride content of 0.30% by weight of cement, indicating a low corrosion risk. However, the core within the main crack zone shows a significant higher chloride content of approximately 1.28%, which corresponds to a high corrosion risk level.

These results are in line with the electrochemical measurements and rebar mass loss results, where sample CN3 in the main crack zone exhibited a higher corrosion rate and larger corrosion pits compared to sample C4 in the main crack zone. This suggest that the corrosion process in CN3 initiated at a faster rate and with greater intensity than C4. Furthermore, the corrosion risk levels predicted from the chloride content analysis for the cores without cracks align with the low corrosion rates measured for the uncracked sample, confirming the overall consistency of the results.

The final result is depicted in Figure 61, which shows a diagram of the chloride content for each core in relation to the penetration depth. In the figure, the blue functions represent sample CN3, while the green functions represent sample C4, with the lighter shade representing Core 1 and the darker shade Core 2 for both samples. The red functions represent the corrosion levels, ranging from lighter to the darker shades to indicate increasing corrosion risk levels. Lastly, the grey function represents the concrete cover depth. Generally, the cores containing the crack exhibit the largest chloride content, while the cores without cracks have the lowest values. This demonstrates that chlorides readily penetrate in the presence of cracks, highlighting their significant influence on chloride ingress into the concrete samples.

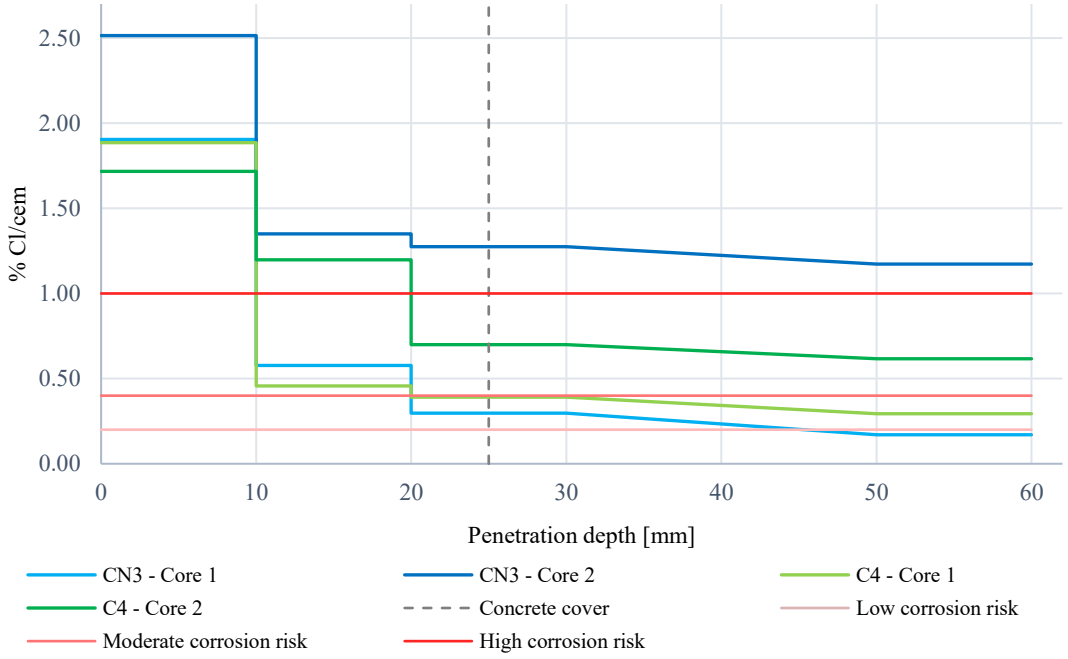

Figure 61: Chloride content over penetration depth

In this context, a comparison between the theoretical and measured results for the chloride content has been conducted, as outlined in Section 4.3, where the theoretical chloride content and the chloride penetration diagram were evaluated. With the actual chloride content measured, a comparison becomes feasible. However, it is important to emphasize that only Core 1 of sample C4 can be used for comparison purposes. This core corresponds to a section of the RC sample that has not been subjected to either notching or cracking. The model utilized to evaluate the chloride content is based on non-cracked RC samples.

The comparison between theoretical and experimental penetration curves is illustrated in Figure 62. The blue and green functions represent the experimental and theoretical results, respectively.

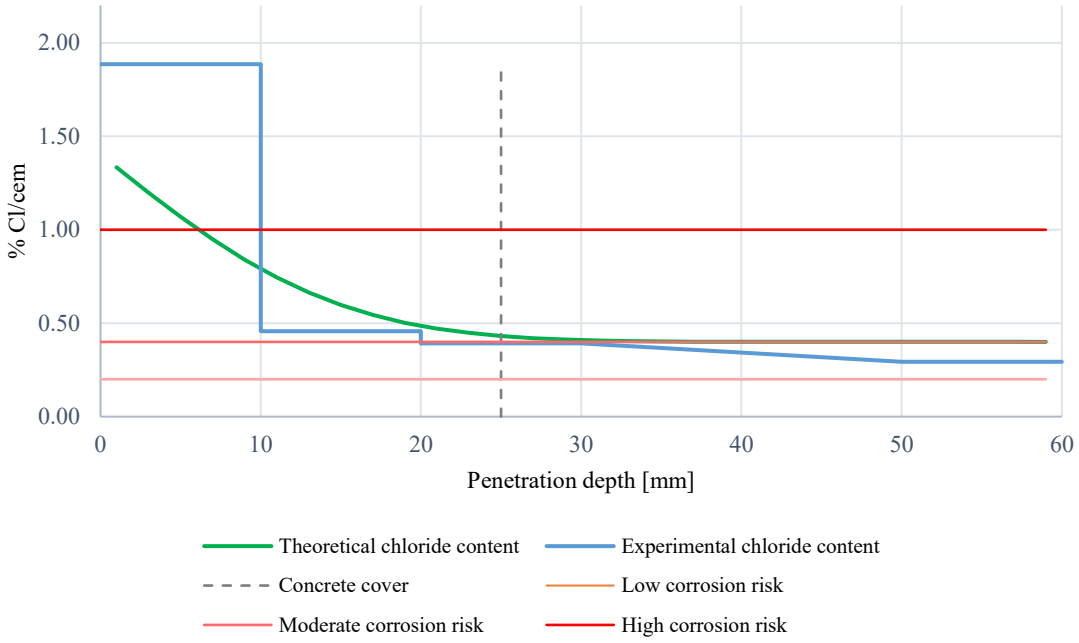

Figure 62: Theoretical and experimental penetration curves

The comparison indicates that there is not substantial difference between the two curves, except at the surface (*x=0*) where the measured chloride content is slightly higher than the predicted value. As the functions extend deeper, they tend to converge and become more similar. At the depth of reinforcement, the measured chloride content is approximately 10% lower than the theoretical value, with the experimental result being 0.39% and the theoretical result being 0.43%.

It is important to consider these differences when interpreting the results and using the theoretical model. Despite the overall similarity, the variations at the surface and the depth of reinforcement can influence the corrosion initiation phase estimation.

5.4.1 Carbonation penetration

The Phenolphthalein test was performed as the last parameter to analyse carbonation in the RC samples. This test serves as a pH indicator for carbonation. When Phenolphthalein ($C_{20}H_{14}O_4$), is sprayed on the concrete surface, a change in color to pink indicates that the concrete is not carbonated, while no change in color suggests carbonation, which results in a lower pH [61]. The change in color is also useful for determining the penetration depth of carbonation. The results of the Phenolphthalein test on the cores are shown in **Errore. L'origine riferimento non è stata trovata.**.

Figure 63: Cores Phenolphthalein test. CN3 cores (on the left), C4 cores (on the right)

The results of the Phenolphthalein test show that all four cores turned pink, indicating that the samples did not undergo carbonation. This outcome can be explained by the corrosion setup described in Section 3.4, where the structure is closed with limited ventilation and high humidity due to water spraying. The lack of ventilation restricts the penetration of CO_2 inside the structure, resulting in a purely chloride-induced corrosion process without the influence of carbonation. Therefore, the corrosion process analyzed in this thesis work is solely chloride-induced corrosion.

5.5 Interpretation of the results

This section aims to provide an interpretation of the results obtained in the previous sections of this chapter, specifically addressing the three main research questions of this thesis:

- How does the presence of mechanical cracks influence the corrosion of steel reinforcement in concrete?
- How does the chloride content influence the corrosion process of steel reinforcement in concrete?
- Do the corrosion parameter models provide a good prediction of the corrosion process in terms of chloride diffusion, chloride content and corrosion rate?

The section is divided into five subsections to address these questions.

5.5.1 Effect of the presence of mechanical cracks

To understand the effect of the mechanical cracks, we consider the corrosion risk levels used in evaluating the corrosion rate for the samples. Table 24 provides a classification of corrosion risk levels and severity of damage [47] [62].

Table 24: Classification of corrosion risk level and severity of damage

i_{corr} [$\mu A/cm^2$]	V_{corr} [*mm/year*]	Corrosion risk	Severity of Damage
≤ 0.1	≤ 0.001	Negligible	No corrosion damage expected
0.1 - 1	0.001 - 0.01	Moderate	Corrosion damage possible in 10 to 15 years
1.0 -10	0.01 - 0.1	High	Corrosion damage expected in 2 to 10 years
> 10	> 0.1	Severe	Corrosion damage expected in 2 or less

Based on this classification, an understanding of the corrosion level is given, particularly in the main transversal crack zone (zone 4) for all the specimens. The observations are as follows:

- *Cracked-notched samples*, especially CN3, with a main crack of 0.70 mm (not corresponding to the notch, a more realistic case), showed very *high* corrosion risk values. Corrosion damage is expected in 2 to 10 years in the zone where the crack (and notch) is located. This level of corrosion is rarely observed in real structures, confirming the high aggressiveness of the adopted corrosion setup.
- *Cracked* samples, representing a more realistic scenario, exhibited slightly *high* corrosion risk values, with expected damage in 2 to 10 years. However, the corrosion rate results for this type of samples were on average *53%* smaller than those obtained for *cracked-notched* samples in zone 4.
- *Uncracked* samples exhibited *moderate* corrosion risk values, with a corresponding possible severity of damage in 10 to 15 years. This is the smallest result among all the types of samples, being on average *37%* smaller than those obtained for the *cracked* ones and *70%* smaller than *cracked-notched* ones. These results align with frequent values measured for actively corroding rebars in real concrete structures (0.1-10 μA/cm^2) [47].

It is important to note that the initial chloride content in the samples is at the maximum allowed by the rules for concrete structure design [54]. Additionally, the concrete cover of 25 mm adopted in this corrosion setup is much smaller than the one allowed by the rules for chloride-induced corrosion in marine environments [55].

5.5.2 Effect of the crack frequency over the samples

The results presented in the Subsection 5.5.1 pertain to the main transversal crack zone (zone 4), making it interesting to analyze the effect of crack frequency on the other zones of the specimen. By revisiting the corrosion risk and severity of damage levels reported in Table 24 and considering the results on the samples reported in Figure 46, it is noticeable that moving from zone 4 to zone 1 the corrosion rate decreases significantly. Specifically, the corrosion risk level in the outer zones is *moderate*, implying possible corrosion damage in 10 to 15 years. This suggests that the zones farther away from the main transverse crack behave similarly to uncracked samples.

The average reduction in corrosion rate when moving from zone 4 to zone 1 and zone 7 is as follows:

- For *cracked-notched* samples, the corrosion rate decreases by an average of *62%.*
- For *cracked* samples, the corrosion rate decreases by an average of *47%.*
- For *uncracked* samples, the corrosion rate decreases by an average of *31%.*

However, it is essential to note that the difference in the discrepancy among the different types of specimens is mainly influenced by the larger corrosion level observed at zone 4 when transitioning from uncracked to cracked-notched

specimens. In fact, in zones 1 and 7, all types of specimens exhibit almost the same corrosion rate values.

5.5.3 Effect of corrosion on concrete cracking

Section 3.3 illustrates the patterns and characteristics of the mechanical cracks in the specimens subjected to the three-point bending test. One of the most interesting aspects was to monitor and visualize possible mechanical crack enlargements or formation of new corrosion cracks, which form parallel to the reinforcement. However, throughout the entire monitoring process of almost five months, no significant results were obtained for any of the samples. The only noteworthy detail to highlight is the visible formation of rust visible in the notch and along the longitudinal mechanical crack, as illustrated in Figure 53.

5.5.4 Effect of chloride content on the corrosion process

Section 5.4 presents an analysis of the chloride content in two different points for samples C4 and CN3. This analysis yielded interesting results, as it allowed a comparison of the chloride content in the zones:

For samples C4:

- Core 1 was taken from zone 7, far from the main crack zone (zone 4).
- Core 2 was taken from zone 4, containing the main transversal crack.

The analysis revealed the following observations:

- Core 2 in sample C4 showed the largest chloride content, with *44%* higher chloride content at the depth of the rebar. Core 2 accounted for 0.*70%* chloride by weight of cement, while core 1 accounted for *0.39%*. The corrosion risk level, given in Table 23, shows that core 2 has a *moderate* risk level, while core 1 has a *low* risk level.

For sample CN3:

- Core 1 was taken at the notch (zone 4) without containing the main transversal crack.
- Core 2 was also taken from zone 4, containing the main transversal crack, which had the largest width among all the specimens, as shown in Figure 59.

The analysis showed the following findings:

- Core 2 in sample CN3 exhibited a larger chloride content than core 1 at the concrete cover depth, with a difference of *77%*. Core 2 had an amount of *1.28%* chloride by weight of cement, while core 1 had *0.30%*. This confirms the significant influence of crack width on chloride ingress in reinforced concrete. According to Table 23, core 2 can be classified in a *moderate* corrosion risk level, very close to the high level, while core 1 falls in the *low* level, very close to the negligible.

It is interesting to note that despite the short-term analysis of the corrosion process, the results are clearly comparable, demonstrating that the cracks serve as a direct connection between the embedded steel reinforcement and the atmosphere.

5.5.5 Comparison between theoretical and measured corrosion parameters

As a final analysis, a comparison was made between the theoretical and measured results for the chloride content and corrosion rate. The theoretical models aim to provide insights into the predicted service life of RC elements; however, achieving accuracy and validity is challenging. In this thesis work, the following observations were made:

Chloride content comparison:

- Figure 62 illustrates a comparison between the theoretical and measured penetration curves for non-cracked RC. The curves differ the most at the surface but tend to get closer as they progress, showing similar values at the concrete cover depth. Specifically, at that depth, the theoretical chloride content is about *9%* larger than the measured one. This is a positive result, indicating that the theoretical model can provide reasonably accurate estimates of chloride content at greater depths in concrete.

  It should be noted, however, that selecting the appropriate parameters for the model is not easy, especially concerning the chloride surface concentration (C_s) and the apparent diffusion coefficient (D_{app}), as both are time-dependent parameters. For short-term analysis, accurately choosing these parameters is challenging because they initially increase rapidly until a point where their increase slows down due to reduced chloride diffusivity within the concrete.

Corrosion rate comparison:

- Comparing the corrosion rate results was even more difficult. The Otieno model [35] was adopted, with the main parameters for prediction being the concrete cover, transversal crack width and apparent diffusion coefficient. The comparison showed very different results. For zone 4, the measured corrosion rate was *84%* larger than the predicted one, as illustrated in Table 17. This indicates the difficulty in matching the theoretical and measured results for corrosion rate prediction.

Chapter 6: Conclusion

This conclusive chapter report the main answers on the research question of this thesis in a more compact and definitive way as done in Section 5.5 of the previous Chapter.

The primary research questions addressed in this thesis were as follows:

- How does the presence of mechanical cracks influence the corrosion of steel reinforcement in concrete?
- How does the chloride content influence the corrosion process of steel reinforcement in concrete?
- Do the corrosion parameter models provide a good prediction of the corrosion process in terms of chloride diffusion, chloride content and corrosion rate?

Moreover, a further section on the suggestions for future works is made.

6.1 General conclusions

Based on the extensive experimental work conducted, the following key conclusions have been drawn:

- The presence of mechanical transversal cracks has a substantial impact on the corrosion rate for chloride-induced corrosion, with potentially dangerous implications for the service life of reinforced concrete elements.
- Mechanical transversal cracks primarily influence the area where the crack is located. However, along the reinforced concrete element, the width of the transversal crack emerges as a critical factor, with larger the crack widths correlating to a more intense corrosion process.
- In short-term analysis utilizing a natural corrosion setup, visualizing the consequences of the corrosion process in terms of corrosion crack formations or spalling remains challenging. Despite efforts to modify concrete cover, apply wetting and drying cycles and utilize the maximum allowed initial chloride content in the concrete mixture, such actions did not provide the expected results.
- The presence of mechanical cracks significantly impacts chloride ingress within concrete, leading to increases chloride content at the depth of reinforcement and consequently reducing initiation time for corrosion. The consistent influence of mechanical transversal cracks on chloride content and

corrosion rate provides helpful insights into the interrelation of these critical parameters for natural chloride-induced corrosion.

- Theoretical models for chloride content display higher reliability in predicting the service life of reinforced concrete elements compared to corrosion rate theoretical models. However, the complexity and unpredictability of parameters influencing chloride-induced corrosion in reinforced concrete elements necessitate a meticulous case-by-case analysis for accurate predictions.

6.2 Suggestions for future works

This thesis represents the first experimental work conducted in this specific type of corrosion setup, as most other experimental tests for natural chloride-induced corrosion are typically conducted in marine environments. While marine environments are not always accessible for experimental testing, this corrosion setup provides a reliable alternative. However, since it was the inaugural experimental test using this approach, several suggestions for future research are presented:

- Long-term analysis: The analysis conducted for this thesis was limited to short-term observations. Therefore, conducting a longer-term analysis would be useful to assess the progression of results and explore the more significant consequences on the rebar mass loss, corrosion cracks formation and consequently concrete spalling, and also to evaluate the initiation time for uncracked samples.
- Realistic concrete cover: The analysis conducted in this experimental work utilized a concrete cover of 25 mm, which is lower than the minimum 40 mm required by regulations in marine environments for chloride-induced corrosion. To achieve more consistent results for real structures, conducting experiments with concrete covers matching the regulations would be valuable, as it covers a paramount importance in the corrosion process.
- Investigation of different crack types: In this experimental work, notches were made to facilitate crack formation at their locations. However, notches are not present in real concrete structures. To align the analysis with real-world scenarios, exploring the influence of different mechanical transveral cracks, without notches, is recommended. To achieve larger transversal crack widths than those in this thesis work, adopting a lower reinforcement-to-concrete ratio while maintaining the recommended concrete cover could be considered.

Appendices

Appendix A: Parameters modelling

In Section 4.2, the evaluation of the apparent diffusion coefficient (D_{app}) is discussed. In Appendix A.1, a more comprehensive analysis of the parameters involved is provided.

A.1 Apparent diffusion coefficient D_{app}

The apparent diffusion coefficient is determined using Equation (2.10), which can be expressed as [40]:

$$D_{app}(t) = \mathrm{k}_e * D_{RCM}(t_0)\left(\frac{t_0}{t}\right)^a \quad \text{(A.1)}$$

In Section 4.2, the experimental value of the chloride migration coefficient, $D_{RCM}(t_0)$, was used. However, according to [41], the mean value can be obtained through interpolation by considering the $D_{RCM,0}$ values at *w/c* ratios of *0.45* and *0.50* for Portland cement type (CEM I). By doing so, a mean value of $1.22*10^{-11}$ m^2/s and a standard deviation of $0.24*10^{-11}$ m^2/s can be determined, see Figure 64.

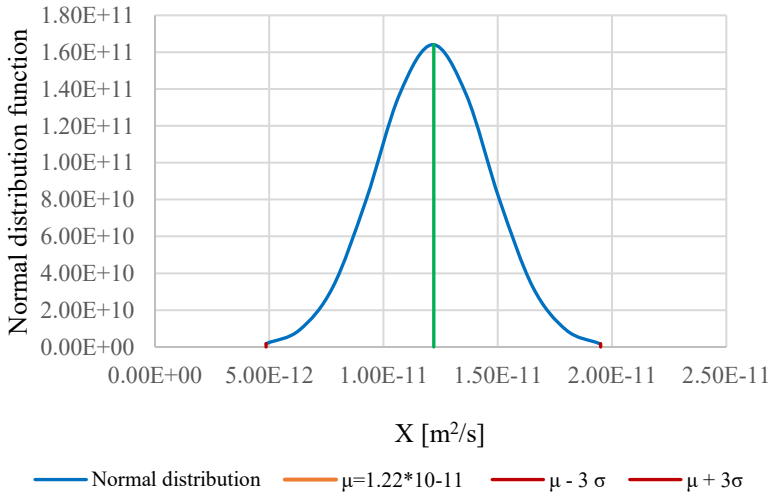

Figure 64: Chloride Migration Coefficient normal distribution curves

Then, the transfer parameter k_t, [-] is commonly assumed to be equal to ***1***, which simplifies the quantification of the ageing coefficient.

The ageing coefficient, *a* [-], is dependent on the type of cement and the water-to-cement ratio (*w/c*). For reinforce concrete (RC) elements with a *w/c* ratio ranging from *0.40* to *0.60*, the ageing coefficient has a mean value of *0.30* and a standard

deviation of *0.12*. It is described by a beta distribution that is defined within the interval, [0,1], and characterized by two positive parameters, *α* and *β*.

Using the mean value (μ) and standard deviation (σ), it is possible to derive the positive parameters required for plotting the function, by deriving *α* and *β* from the following two expressions:

$$\begin{cases} \mu = \frac{\alpha}{\alpha+\beta} \\ \sigma = \sqrt{\frac{\alpha\beta}{(\alpha+\beta)^2(\alpha+\beta+1)}} \end{cases} \tag{A.2}$$

Applying this information, it is obtained the following distribution:

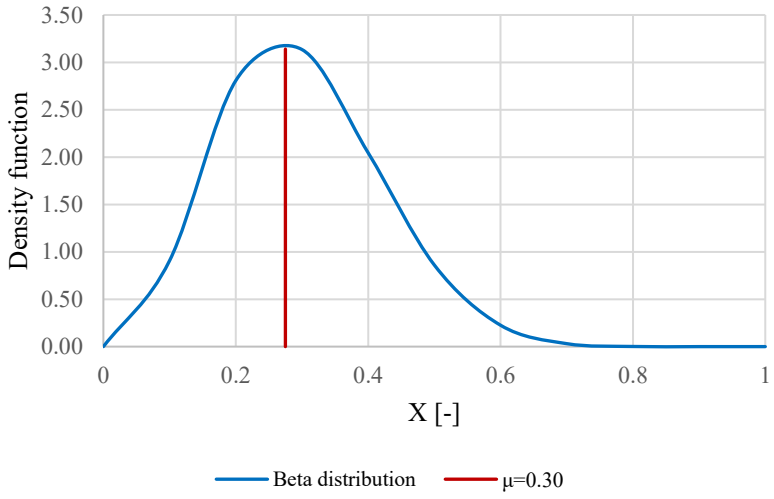

Figure 65: Ageing coefficient Beta distribution

The first exposure time t_0 [years] corresponds to *77* days, namely, *0.2110 years.*

The regression variable, b_e [K], can vary between *3500 K* and *5500 K*. However, it is typically described by a normal distribution with mean value of *4800 K* and a standard deviation of *700 K*.

The ambient temperature surrounding the specimens, T_{real} [K], is controlled in the Laboratory and ranges from *292 K* to *293 K*. It is characterized by a normal distribution with mean value of *293 K* and a standard deviation of *1 K*.

The standard test temperature, T_{ref} [K], remains constant at *293 K*.

The environmental transfer variable, k_e, [-], is calculated using the equation:

$$\mathrm{k}_e = e^{\left(b_e\left(\frac{1}{T_{ref}}-\frac{1}{T_{real}}\right)\right)} \tag{A.3}$$

In this case, the equation results in a value of **1**.

Appendix B: Electrochemical parameters monitoring

In this appendix, the corrosion parameter results for the other six samples are presented, consisting of one uncracked, three cracked and two cracked-notched. These samples were characterized, and their crack mapping was provided in Section 3.3. The graphs for these remaining samples display a larger time-domain as the measurements were conducted until 50 days after the extraction of the rebars from sample C4 and CN3.

B.1 Corrosion potential

The corrosion potential results for the remaining samples are presented in this Appendix Section, as depicted in Figure 66:

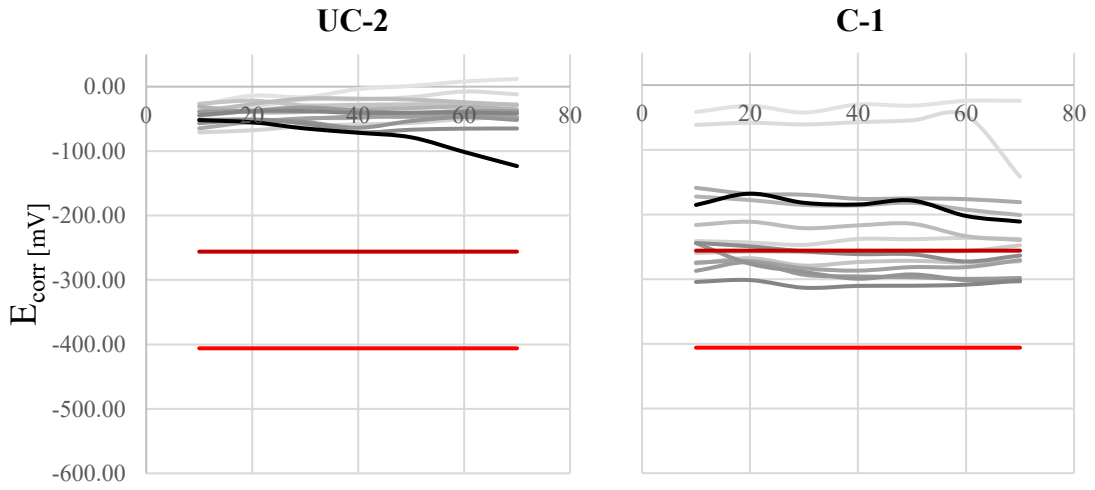

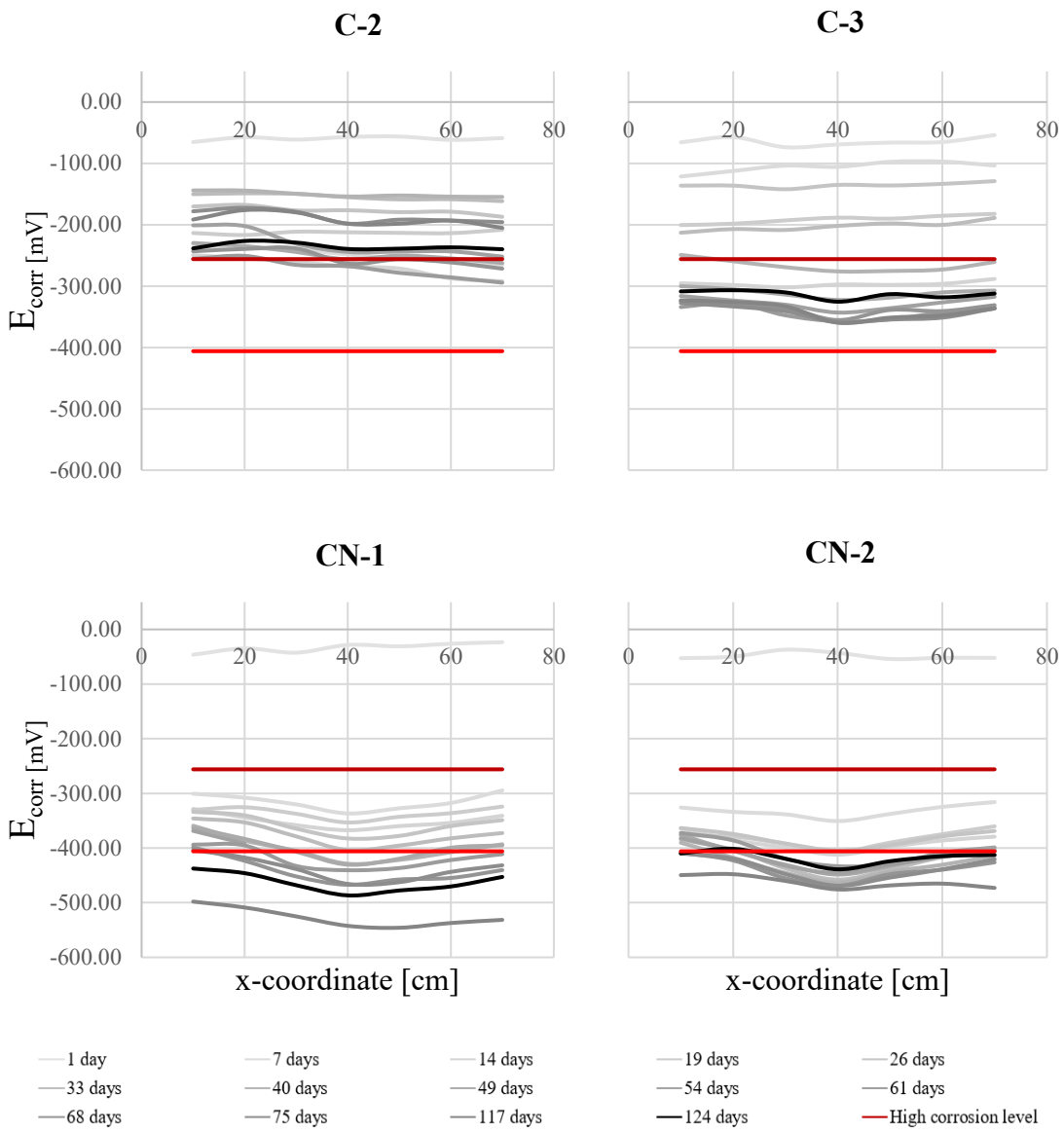

Figure 66: Corrosion potential over space for samples: UC2, C1, C2, C3, CN1 and CN2

These graphs confirm the observations made in Figure 43 from Chapter 5, where the corrosion potential decreases when transitioning from uncracked samples to cracked-notched ones.

It is evident that the three types of samples can be grouped based on they corrosion risk level:

- UC2 exhibits absolute corrosion potential values lower than the high corrosion risk level.
- C1, C2 and C3 display values between the two corrosion risk levels of high and severe.
- CN1 and CN2 show the highest corrosion risk level, surpassing the severe level.

Furthermore, moving from the uncracked sample to the cracked-notched ones, it becomes apparent that the corrosion potential curves tend to shift from a flat profile to a more pronounced curve, with a more distinct sag evident in the cracked-notched samples.

B.2 Corrosion current density

The corrosion current density results for the remaining samples are presented in this Appendix Section, as shown in Figure 67Figure 66:

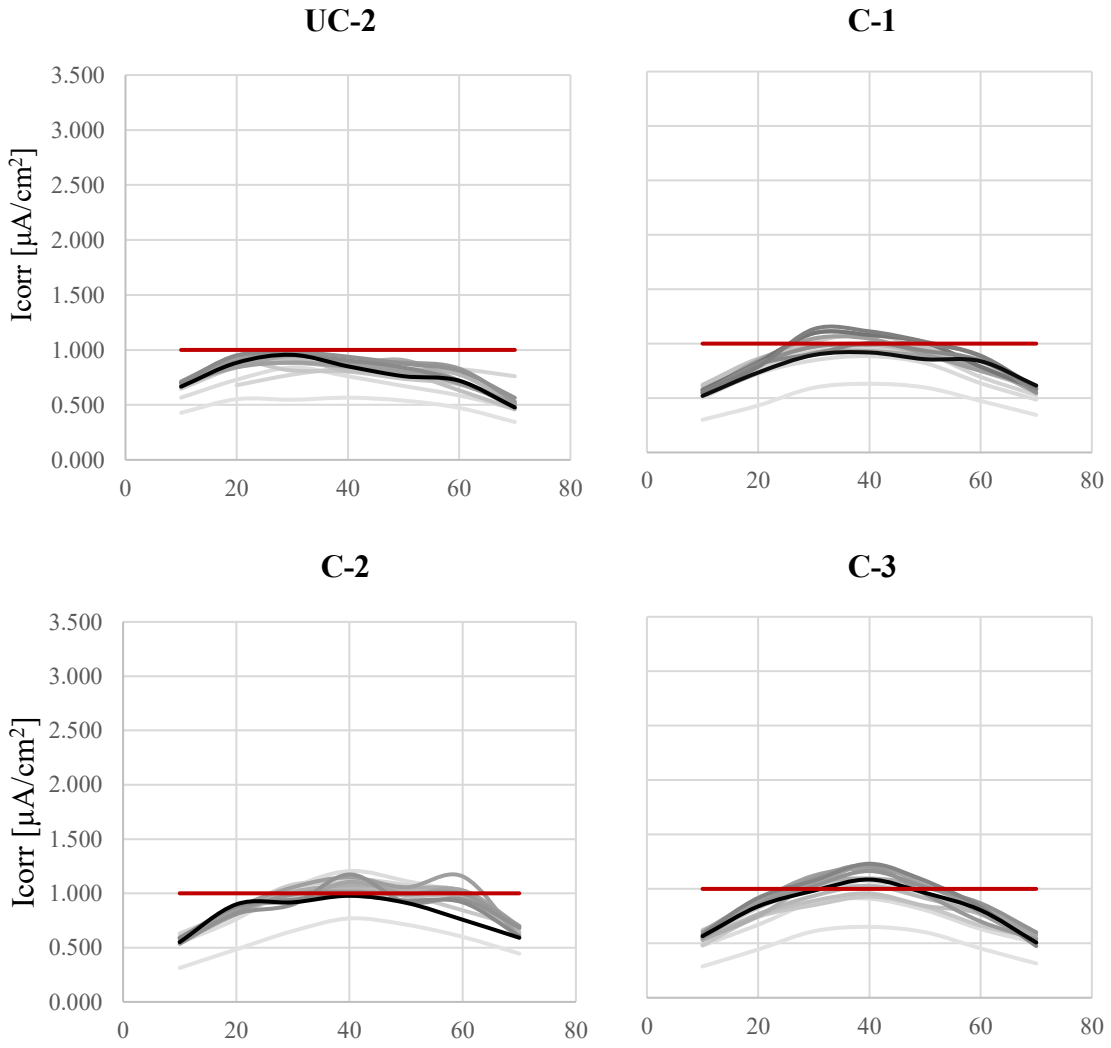

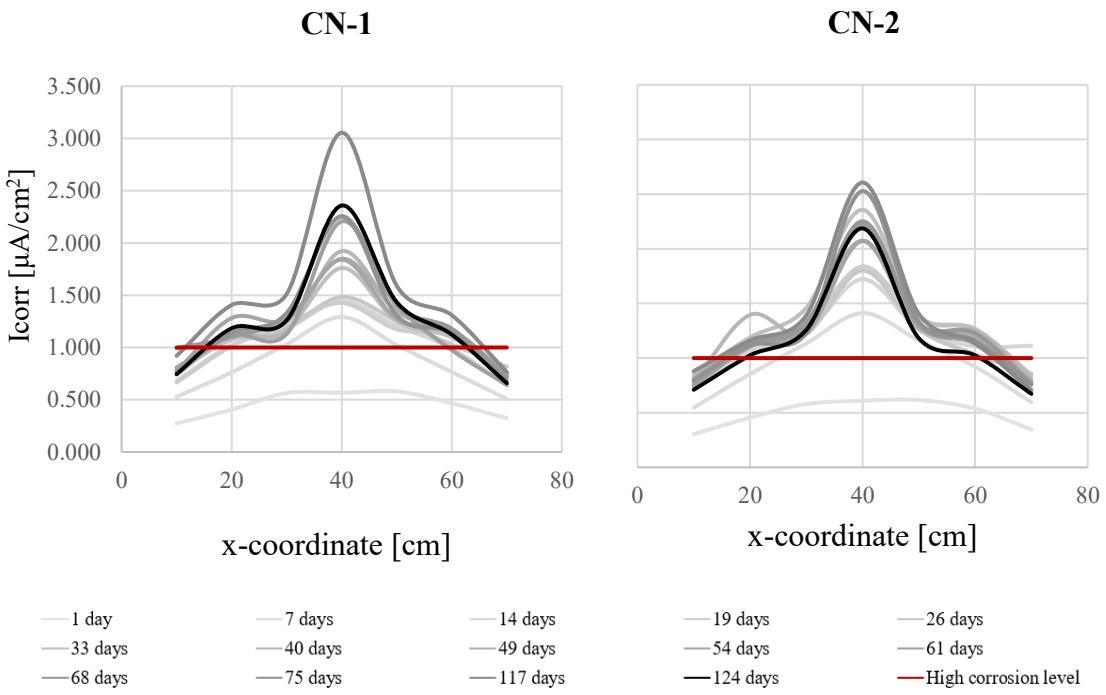

Figure 67: Corrosion current density over space for samples: UC2, C1, C2, C3, CN1 and CN2

Once again, these graphs reaffirm the observations made in Figure 45 from Chapter 5 for the other three samples.

The important feature in Figure 67 is the significant difference in the main crack zone (40 cm) between the cracked-notched specimens and all the others. In the cracked-notched samples, the corrosion current density values are substantially higher than the high corrosion risk level. On the other hand, for the cracked samples (C1, C2 and C3), the maximum values in the middle are slightly higher than the high corrosion risk level. Lastly, for UC2, all the functions at various locations along the specimen show i_{corr} values lower than the high corrosion risk level.

B.3 Corrosion rate

The functions representing the corrosion rate are organized using different types of lines for each type of specimen: straight lines for cracked-notched samples, dashed lines for cracked samples and dotted lines for uncracked samples. Additionally, as the main transverse crack width increases from one sample to another (e.g., from C1 to C4), the contrast of the colors used in the representation also increases.

By analyzing the corrosion parameters for these additional samples, more consistency and insight into the differences in the corrosion behavior of steel reinforcement in concrete among the various types of specimens are gained.

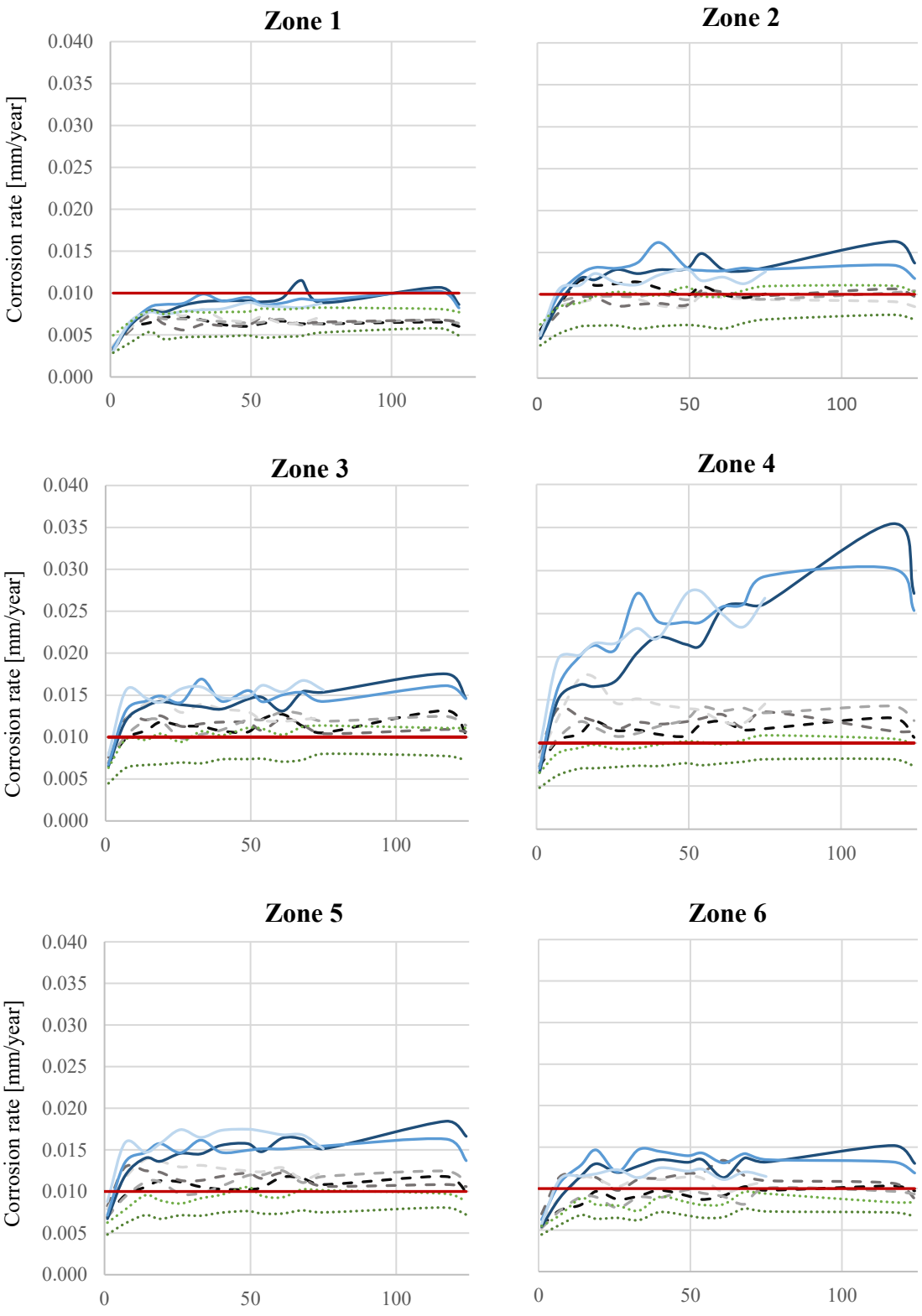
Zone 1
Zone 2
Zone 3
Zone 4
Zone 5
Zone 6
Corrosion rate [mm/year]
0.040
0.035
0.030
0.025
0.020
0.015
0.010
0.005
0.000
0
50
100

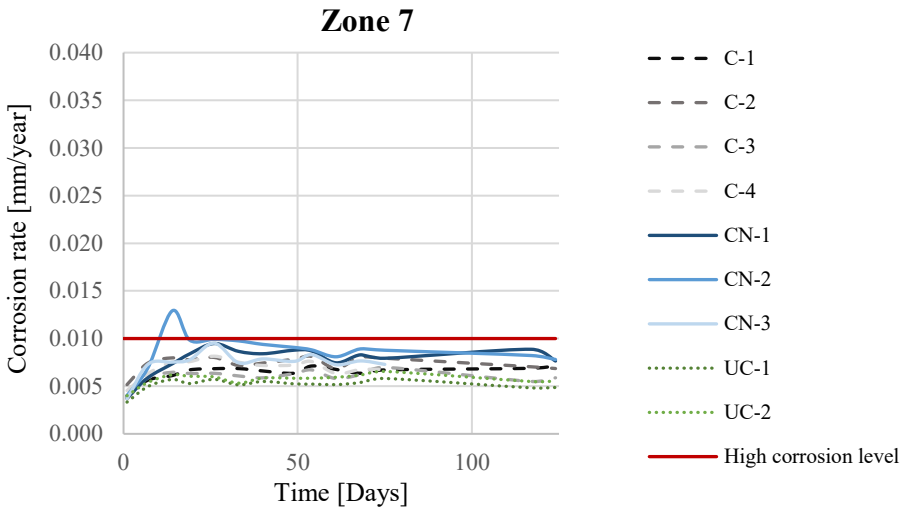

Figure 68: Corrosion rate in different zone for each sample

The corrosion rate figures present a significant outcome, clearly demonstrating the consistency of results among the cracked-notched, cracked and uncracked samples. Notably, the differences in corrosion rate are most prominent in zone 4, where the specimens with cracks and notches exhibit higher corrosion rates compared to the uncracked ones.

Furthermore, an essential finding is that zone 4, which contains the main transversal crack, shows the highest corrosion rates. However, the reduction in corrosion rate moving towards zones 1 and 7, symmetrically, indicates an interesting trend. This reduction is not solely attributed to the width of the transversal cracks, as the crack monitoring revealed minimal differences in crack widths outside the main crack zone, ranging from 0.03 and 0.06 mm.

Instead, this trend could be related to the frequency of cracks in those zones. Moving away from the main zone, the distance between subsequent transversal crack decreases, potentially influencing the corrosion rate. This suggests that the distribution and frequency of cracks play a crucial role in determining the corrosion behavior, in addition to the crack width itself.

Bibliography

[1] J. Yong-Sheng, Z. Wen, M. Hui-Rong y Z. Ping, «Corrosion current distribution of macrocell and microcell of steel bar in concrete exposed to chloride environments,» *Construction and Building Materials,* vol. 47, pp. 104-110, 2013.

[2] G. De Schutter, Damage to Concrete Structures, Boca Raton: Taylor & Francis Group, 2013.

[3] W. w. Buildwise, *Betonschade door wapeningscorrosie Oorzaken –diagnose – herstel-en beschermmethoden,* 2022.

[4] M. Collepardi y L. Coppola, «Cause piu' frequenti di degrado delle strutture in calcestruzzo,» 1993.

[5] A. P. Fantilli y F. Tondolo, «Crack widths in RC and R/FRC elements under repeated actions,» de *fib Bulletin 106*, Torino, 2019, pp. 299-308.

[6] H. Böhni, Corrosion in reinforced concrete structures, Cambridge: CRC Press LLC, 2005.

[7] K. Esfandiari, M. Banihashemi y P. Soleimani, «Influence of impressed current cathodic protection (ICCP) systems on chemical characteristics of underground water,» *Water Environment Research,* vol. 92, pp. 2105-2111, 2020.

[8] M. Pourbaix, E. D. Verink y K. K. Starr, «The Significance of the Protection Potential for Fe-Cr Alloys at Room Temperature.,» *Corrosion,* vol. 32, nº 2, pp. 47-51, 1976.

[9] A. Poursaee, *Corrosion of Steel in Concrete Structures,* Matthew Deans, 2016.

[10] R. T. L. Allen y J. A. Forrester, «The Investigation and Repair of Damaged Reinforced Concrete Structures.,» *Society of Chemical Industry,* p. 29, 1983.

[11] B. Martin-Perez, H. Zibara, R. D. Hooton y M. D. A. Thomas, «A study of the effect of chloride binding on service life predictions,» *Cement and Concrete Research,* vol. 30, pp. 1215-1223, 2000.

[12] European Committee for Standardization, *EN 206: Concrete - Specification,*

performance, production and conformity, 2013.

[13] U. Angst, B. Elsener, C. K. Larsen y Ø. Vennesland, «Critical chloride content in reinforced concrete — A review,» *Cement and Concrete Research,* vol. 39, pp. 1122-1138, 2009.

[14] Q. Yuan, C. Shi, G. De Shutter, K. Audenaert y D. Deng, «Chloride binding of cement-based materials subjected ti external chloride environment - A review,» *Construction and Building Materials,* vol. 23, pp. 1-13, 2009.

[15] P. F. Marques, A. Costa y F. Lanata, «Service life of RC structures: Chloride induced corrosion: Prescriptive versus performance-based methodologies,» *Materials and Structures,* vol. 45, pp. 277-296, 2012.

[16] M. Raupach, «Chloride-induced macrocell corrosion of steel in concrete-theoretical background and practical consequences,» *Construction and Building Materials,* vol. 10, nº 5, pp. 329-338, 1995.

[17] K. Hornbostel, C. K. Larsen y M. R. Geiker, «Relationship between concrete resistivity and corrosion rate - A literature review,» *Cement & Concrete Composites,* vol. 39, pp. 60-72, 2013.

[18] A. Poursaee y B. Ross, «The Role of Cracks in Chloride-Induced Corrosion of Carbon Steel in Concrete — Review,» *Corrosion and materials degragation,* vol. 3, pp. 258-269, 2022.

[19] A. Poursaee y C. M. Hansson, «The influence of longitudinal cracks on the corrosion protection afforded reinforcing steel in high performance concrete.,» *Cement and Concrete Research,* vol. 38, pp. 1098-1105, 2008.

[20] C. Arya y F. K. Ofori-Darko, «Influence of crack frequency on reinforcement corrosion in concrete.,» *Cement Concrete Research,* vol. 26, nº 3, pp. 345-353, 1996.

[21] P. Schiessl y M. Raupach, «Laboratory studies and calculations on the influence of crack width on chloride-induced corrosion of steel in concrete.,» *Materials journal,* p. 94, 1997.

[22] A. Blagojevic, «The Influence of Cracks on the Durability and Service Life of Reinforced Concrete Structures in Relation to Chloride-Induced Corrosion.,» *Ph.D. Thesis, Delft University of Technology,* 2015.

[23] L. Abo ALarab, B. E. Ross y A. Poursaee, «Influence of transverse crack opening size on chloride-induced corrosion of steel bars in concrete.,» *J. Bridge. Engineering,* vol. 25, nº 6, pp. 1-6, 2020.

[24] S. Robuschi, *Natural corrosion in reinforced concrete structures,* Gothenburg, Sweden, 2021.

[25] J. Yong-sheng, J. Yijie, Z. Linglei y B. Zhongzheng, «Laboratory studies on influence of transverse cracking on chloride-induced corrosion rate in concrete,» *Cement and Concrete Composites,* vol. 69, pp. 28-37, 2015.

[26] Y. Ballim y J. C. Reid, «Reinforcement corrosion and the deflection of RC beams - An experimental critique of currrent test methods,» *Cement and Concrete Composites,* vol. 25, pp. 625-632, 2003.

[27] G. Malumbela, *Measurable parameters for performance of corroded and repaired RC beams under load,* PhD thesis, University of Cape Town, 2010.

[28] M. Otieno, «Techniques for accelerating chloride-induced corrosion: of steel in concrete: A review and general guidelines,» *Civil engineering,* vol. 28, nº 6, pp. 1-9, 2020.

[29] F. Hunkeler, «Corrosion in reinforced concrete: Processes and mechanisms,» *Cement and Concrete,* pp. 1-49, 2005.

[30] M. Raupach, «Investigations on the influence of oxygen on corrosion of steel in concrete - Part 1,» *Materials and Structures,* vol. 29, pp. 174-184, 1996.

[31] M. Otieno, H. D. Beushausen y M. G. Alexander, «Concrete under severe conditions : environment and loading : proceedings of the 6th International Conference on Concrete Under Severe Conditions,» de *Concrete Under Severe Conditions*, Merida, Yucatan, Mexico, CRC Press, 2010, pp. pp. 461-469.

[32] M. Otieno, H. Beushausen y M. Alexander, «Prediction of corrosion rate in reinforced concrete structures - a critical review and preliminary results,» *Material and corrosion,* vol. 63, nº 9, pp. 777-790, 2012.

[33] M. Otieno, H. Beushausen y M. Alexander, «Prediction of Corrosion Rate in RC Structures - A Critical Review,» de *RILEM Bookseries*, vol. 63, C. Andrade and G. Mancini, 2011, pp. 15-37.

[34] E. Vereecken, W. Botte, G. Lombaert y R. Caspeele, «Time-dependent degradation due to corrosion,» *Structural concrete,* pp. 1-30, 2021.

[35] M. Otieno, H. Beushausen y M. Alexander, «Chloride-induced corrosion of steel in cracked conrete - Part II: corrosion rate prediction models,» *Cement and Concrete Research,* vol. 79, pp. 386-394, 2016.

[36] M. Otieno, H. Beushausen y M. Alexander, «Chloride-induced corrosion of steel in cracked concrete - Part I: Experimental studies under accelerated and natural marine environments,» *Cement and Concrete Research,* vol. 79, pp. 373-385,

2016.

[37] The European Union– Brite EuRam III, *DuraCrete: Probabilistic Performance based Durability Design of Concrete Structures,* 1998.

[38] E. Koenders, K.-i. Imamoto y A. Soive, «Benchmarking Chloride Ingress Models on Real-life Case Studies - Marine Submerged and Road Sprayed Concrete Structures,» de *RILEM STATE-OF-THE-ART REPORTS*, Eddie Koenders, Kei-ichi Imamoto and Anthony Soive, 2022.

[39] M. Collepardi, *Il nuovo calcestruzzo,* 1970.

[40] Fédération international du béton (fib), *Bulletin 76: Benchmarking of deemed-to satisfy provisions in standards: Durability of reinforced concrete structures exposed to chlorides- 76,* 2015.

[41] Fédération international du béton (fib), *Bulletin 34: Model Code for Service Life Design,* 2006.

[42] NT BUILD, *492: Nordtest method,* 1999.

[43] G. R. Meira, P. R. Ferreira y C. Andrade, «Long-Term Chloride Accumulation on Concrete Surface in Marine Atmosphere Zone—Modelling the Influence of Exposure Time and Chloride Availability in Atmosphere,» *Corrosion and material degradation,* vol. 3, pp. 349-362, 2022.

[44] L. F. Yang, R. Cai y B. Yu, «Investigation of computational model for surface chloride concentration of concrete in marine atmosphere zone,» *Ocean engineering,* vol. 138, pp. 105-111, 2017.

[45] Q.-f. Liu, Z. Hu, X.-y. Lu, J. Yang, I. Azim y W. Sun, «Prediction of Chloride Distribution for Offshore Concrete Based on Statistical Analysis,» *Materials,* vol. 174, p. 16, 2020.

[46] S. F. I. o. T. Zürich, «ETH corrosion,» 8 December 2021. [En línea].

[47] C. Andrade, C. Alonso, J. Gulikers, R. Polder, R. Cigna, O. Vennesland, M. Salta, A. Raharinaivo y B. Elsener, «Test methods for on-site corrosion rate measurement of steel reinforcement in concrete by means of the polarization resistance method,» *Materials and Structures,* vol. 37, pp. 623-643, 2004.

[48] B. Elsener, C. Andrade, J. Gulikers, R. Polder y M. Raupach, «Half-cell potential measurements- Potential mapping on reinforced concrete structures,» *Materials and Structures,* vol. 36, pp. 461-471, 2003.

[49] Germann Instruments, *GalvaPulse,* Copenhagen, Denmark, 2021.

[50] O. Klinghoffer, «In situ monitoring of reinforcement corrosion by means of electrochemical methods,» *Nordic Concrete Research,* vol. 95, nº 1, pp. 1-13.

[51] American Society for Testing and Materials (ASTM), «G1-03: Standard practice for preparing, cleaninng, and evaluating corrosion test specimens,» 2017.

[52] J. Rodriguez y C. Andrade, *CONTECVET - A validated Users Manual for assessing the residual service life of concrete structrures.*

[53] J. Chukwuneke, «Investigation Of The Effect Of Corrosion On Mild Steel In Five Different Environments,» *Scientific & Technology Research,* vol. 3, nº 7, pp. 306-310, 2014.

[54] European Committee for Standardization, *EN 12390-1: Testing hardened concrete. Shape, dimensions and other requirements for specimens and moulds,* 2012.

[55] European Committee for Standardization, *Eurocode 2: Design of concrete structures - Part 1-1 : General rules and rules for buildings,* 2004.

[56] T. Pape y R. Melchers, «Comparison between two corrosion assessment methods and the corrosion of steel in prestressed concrete,» de *Corrosion & Prevention*, Newcastle, Australia, 2009.

[57] M. Daniyal y S. Akhtar, «Corrosion assessment and control techniques for reinforced concrete structures: a review,» *Building Pathology and Rehabilitation,* vol. 5, nº 1, pp. 1-20, 2020.

[58] American Society for Testing and Materials (ASTM), *C876: Standard test method for corrosion potentials of uncoated reinforcing steel in concrete.,* 2015.

[59] «Radical Scientific Equipments Pvt. Ltd.,» [En línea]. Available: https://www.radicalscientific.com/Crackmeasuringdevices.html.

[60] «Mayes Group Windsor England,» [En línea]. Available: http://www.mayes.co.uk/6.html.

[61] Builders booklet, «BUILDERS BOOKLET,» 26 12 2021. [En línea]. Available: https://www.buildersbooklet.com/concrete/carbonation-test-of-concrete/.

[62] G. Crevello, I. Matteini y P. Noyce, «Understanding the Rates of Corrosion in Concrete Structures,» *Structure,* pp. 17-20, 2016.